



## AVERTISSEMENT

Ce document est le fruit d'un long travail approuvé par le jury de soutenance et mis à disposition de l'ensemble de la communauté universitaire élargie.

Il est soumis à la propriété intellectuelle de l'auteur. Ceci implique une obligation de citation et de référencement lors de l'utilisation de ce document.

D'autre part, toute contrefaçon, plagiat, reproduction illicite encourt une poursuite pénale.

Contact : [ddoc-theses-contact@univ-lorraine.fr](mailto:ddoc-theses-contact@univ-lorraine.fr)

## LIENS

Code de la Propriété Intellectuelle. articles L 122. 4

Code de la Propriété Intellectuelle. articles L 335.2- L 335.10

[http://www.cfcopies.com/V2/leg/leg\\_droi.php](http://www.cfcopies.com/V2/leg/leg_droi.php)

<http://www.culture.gouv.fr/culture/infos-pratiques/droits/protection.htm>



UNIVERSITÉ  
DE LORRAINE



## Université de Lorraine

Collegium Sciences et Techniques  
École Doctorale Energie Mécanique  
et Matériaux (EMMA)

Thèse présentée et soutenue publiquement le 5 décembre 2016  
pour l'obtention du titre de  
Docteur de l'Université de Lorraine  
en Physique  
par **Dimitrios Voliotis**

### **Contribution à l'étude des chaînes de spin quantique avec une perturbation aléatoire ou apériodique**

Membres du jury:

<i>Rapporteurs:</i>	Cécile Monthus	Directrice de recherche, CNRS, CEA Saclay
	Janos Polonyi	Professeur, Université de Strasbourg
<i>Examineurs:</i>	Jean-Christian Anglès-Dauriac	Directeur de recherche, CNRS, Université de Grenoble
	Jean-Yves Fortin	Directeur de recherche, CNRS, Université de Lorraine
<i>Directeur:</i>	Christophe Chatelain	Maître de Conférences, Université de Lorraine

**Institut Jean Lamour - Groupe de Physique Statistique**  
**Faculté des Sciences & Technologies - 54500 Vandœuvre-lès-Nancy**

**Contribution to the study of  
quantum spin chains with a  
random or aperiodic perturbation**

Dimitrios Voliotis

January 27, 2017

---

## ABSTRACT

---

In the present thesis, the critical and off-critical behaviors of quantum spin chains in presence of a random or an aperiodic perturbation of the couplings is studied.

The critical behavior of the Ising and Potts random quantum chains is known to be governed by the same Infinite-Disorder Fixed Point. We have implemented a numerical version of the Strong-Disorder Renormalization Group (SDRG) to test this prediction. We then studied the quantum random Ashkin-Teller chain by Density Matrix Renormalization Group. The phase diagram, previously obtained by SDRG, is confirmed by estimating the location of the peaks of the integrated autocorrelation times of both the spin-spin and polarization-polarization autocorrelation functions and of the disorder fluctuations of magnetization and polarization. Finally, the existence of a double-Griffiths phase is shown by a detailed study of the decay of the off-critical autocorrelation functions. As expected, a divergence of the dynamical exponent is observed along the two transition lines.

In the aperiodic case, we studied both the Ising and Potts quantum chains. Using numerical SDRG, we confirmed the known analytical results for the Ising chains and proposed a new estimate of the magnetic scaling dimension. For the quantum  $q$ -state Potts chain, we estimated the magnetic scaling dimension for various aperiodic sequences and showed that it is independent of  $q$  for all sequences with a vanishing wandering exponent. However, we observed that the dynamical exponent is finite and increases with the number of states  $q$ . In contrast, for the Rudin-Shapiro sequence, the results are compatible with an Infinite-Disorder Fixed Point with a diverging dynamical exponent.

---

## RÉSUMÉ

---

Au cours de cette thèse, nous avons étudié le comportement critique de chaînes de spins quantiques en présence de couplages désordonnés ou répartis de manière apériodique.

Il est bien établi que le comportement critique des chaînes de spins quantiques d'Ising et de Potts est gouverné par le même point fixe de désordre infini. Nous avons implémenté une version numérique de la technique de renormalisation de désordre infini (SDRG) afin de tester cette prédiction. Dans un second temps, nous avons étudié la chaîne quantique d'Ashkin-Teller désordonnée par renormalisation de la matrice densité (DMRG). Nous confirmons le diagramme de phase précédemment proposé en déterminant la position des pics du temps d'autocorrélation intégré des corrélations spin-spin et polarisation-polarisation ainsi que ceux des fluctuations de l'aimantation et de la polarisation. Enfin, l'existence d'une double phase de Griffiths est confirmée par une étude détaillée de la décroissance des fonctions d'auto-corrélation en dehors des lignes critiques. Comme attendu, l'exposant dynamique diverge à l'approche de ces lignes.

Dans le cas apériodique, nous avons étudié les chaînes quantiques d'Ising et de Potts. En utilisant la méthode SDRG, nous avons confirmé les résultats connus pour la chaîne d'Ising et proposé des estimations de la dimension d'échelle magnétique. Dans le cas du modèle de Potts à  $q$  états, nous avons estimé l'exposant magnétique et observé qu'il était indépendant du nombre d'états  $q$  pour toutes les séquences dont l'exposant de divagation est nul. Toutefois, nous montrons que l'exposant dynamique est fini et augmente avec le nombre d'états  $q$ . En revanche, pour la séquence de Rudin-Shapiro, les résultats sont compatibles avec un point fixe de désordre infini et donc un exposant dynamique infini.

Dedicated to the memory of Professor Ioannis Bakas (1960-2016).

---

## ACKNOWLEDGEMENTS

---

First of all, I would like to thank my thesis advisor, Christophe Chate-  
lain for his unlimited patience to answer my questions (many times  
the same), to the freedom which he provide me as well as his desire  
to correct my thesis line by line.

I am much obliged to Mme Cécile Monthus and M. Janos Polonyi  
who their acceptance be the *rapporteurs* and M. Jean-Cristian Anglés-  
Dauriac and M. Jean-Yves Fortin who they participate as *examineurs*  
in the jury.

I am grateful to all the members of the *Equipe de Physique Statistique*  
of the Institut Jean Lamour for the scientific environment which they  
provide to all the stages of my studies. I have to thank a bit more,  
for they personal support: Bertrand Berche, Olivier Collet, Jean-Yves  
Fortin and Malte Henkel.

I would like to thank my office colleges: Pierre Wendenbaum, Mar-  
jana Krasnytska, Nicolas Allegra, Emilio Flores, Hugo Tschirhart, Sascha  
Wald, Frank Avezedo and Yannis Brun for the hours and hours that  
we shared together. I would like to thank also, my colleges from other  
groups: Mohammed-Salah Elhadri, Mathilde Blaise, Florent Hild and  
Lucas Eichenberger for our breaks and discussions.

Many thanks to the secretariat Mme Valérie Madeline who always  
kindly answered all my requests and helped me with problems out-  
side her responsibilities.

Words are powerless to express my gratitude to the director of IUT  
of Lunéville, Mme Isabelle Perry, who gave me the opportunity to  
participate in the teaching program DCCE. I am also much obliged,  
to the second year students who kindly accepted to teach me French!

I am grateful to the members of the group of Statistical mechanics  
of the Applied Mathematics Research Centre at Coventry University,  
for the warm hospitality during my visit. I would like, especially to  
thank for their help, Martin Wiegel and Nikos Fytas. I was very lucky  
to meet a personality as Nikos!

I am grateful to the members of Department of Statistical Mechan-  
ics of University of Sao Paulo for the warm hospitality. I have to note:  
Mario J. de Oliveira. Tania Tome, Masayuki Hase, Andre P. Vieira but  
especially Alexander Wada, Pedro. H. Guimarães and Gabriel Landi.

I am grateful to the organizers of *Statistical Field Theory* lectures in  
GGI in Florence for the warm hospitality and especially my friends  
and colleges Davide Nuzzi and Clément Tauber.

Finally, I would like to thank my family in Nancy where each  
of them played a unique role in my life the last three years: Valia  
Tsiontsiou, Dimitris and Bernadette Tsabalas, Alexis Tsabalas, Anto-

nis Antoniadis, Jeremy Leroi, Lelia Thiriet, Apostolis and Anti Katsinoula, Vassilis and Mariana Vassiliadi, Vitalis Ntombrougidis and Ioardanis Iordanov.

---

## CONTENTS

---

List of Figures    iii

List of Tables    viii

1	RÉSUMÉ DÉTAILLÉ EN FRANÇAIS	1
1.1	Introduction	1
1.2	Les transitions de phase quantique de systèmes aléatoires	2
1.2.1	Renormalisation de désordre infini pour les modèles d'Ising	2
1.2.2	Etude de la transition de phase quantique du modèle d'Ashkin-Teller	4
1.3	Les transitions de phase quantiques de systèmes aperiodiques	8
1.3.1	Séquences aperiodiques et matrice de substitution	8
1.3.2	Critère de Luck	8
2	INTRODUCTION AND OUTLINE	14
3	INTRODUCTION TO PHASE TRANSITIONS	17
3.1	Aspects of Classical Phase Transitions	17
3.2	Quantum Phase Transitions	20
3.3	Phase transitions in Disordered Systems	24
3.3.1	Quenched disorder	24
3.3.2	Rare regions and Griffiths phase	25
4	QUANTUM PHASE TRANSITION IN RANDOM SYSTEMS	27
4.1	The Random Quantum Ising Chain	27
4.1.1	The model	27
4.1.2	SDRG approach	29
4.1.3	Numerical test	34
4.2	The Random Quantum Potts model	36
4.2.1	Hamiltonian limit	36
4.2.2	Strong-Disorder RG approach for the random quantum Potts model	39
4.2.3	Numerical test	40
4.3	The random quantum Ashkin-Teller model	43
4.3.1	The model	43
4.3.2	DMRG study of the random Ashkin-Teller model	46
4.3.3	Conclusion	59
5	QUANTUM PHASE TRANSITIONS IN APERIODIC SYSTEMS	60
5.1	Introduction	60
5.2	Aperiodic Sequences	64
5.2.1	Substitution Matrix	64
5.2.2	Irrelevant/Relevant Criterion	66
5.2.3	Aperiodic Sequences	67
5.3	The Aperiodic Quantum Ising Model	70

5.3.1	Application to a family of aperiodic sequences	70
5.3.2	Numerical results at the critical point	77
5.4	The Aperiodic Quantum Potts Model	90
5.4.1	SDRG analysis for the Fibonacci family of aperiodic sequences	90
5.4.2	Magnetic scaling dimension	91
5.4.3	Dynamical exponent	95
5.5	Conclusion	102
6	GENERAL CONCLUSION	106
	Bibliography	108
	Appendices	
.1	Strong-Disorder Renormalization Group details for the RTFIM	114
.1.1	Green functions and Dyson equation	114
.1.2	Renormalization rule for strong bond $J_i$	115
.1.3	Renormalization rule for a strong field $h_i$	116
.2	SDRG for the Potts model	117
.2.1	Properties for the Potts operators	117
.2.2	SDRG rule for strong field	118
.2.3	SDRG rule for strong bond	119
.3	Density-Matrix Renormalization Group	120
.3.1	Introduction	120
.3.2	Density Matrix Renormalization Group algorithms	120
	Appendix Bibliography	124

---

LIST OF FIGURES

---

Figure 1	Règles de renormalisation pour le RTFIM.	3
Figure 2	Chaîne d'Ashkin-Teller avec des couplages entre les spins $\sigma_i$ et $\tau_i$ .	4
Figure 3	Phase diagram of $\text{LiHoF}_4$ as extracted by Bitko <i>et al.</i> [8]. Magnetic field versus the temperature.	21
Figure 4	Schematic phase diagram of a system undergoing a quantum phase transition. The critical lines are presented with the various phases. Figure inspired from [3] and [12].	23
Figure 5	The change from pure to random interaction constant and magnetic field.	24
Figure 6	The paramagnetic Griffiths phase. Locally ferromagnetic rare regions (blue) inside a paramagnetic bulk (green).	25
Figure 7	The ferromagnetic Griffiths phase. Locally ordered rare islands (blue) decoupled from the rest of the system by a paramagnetic shell (green).	26
Figure 8	One-dimensional quantum Ising chain of Hamiltonian (54).	27
Figure 9	SDRG rules for RTFIM.	30
Figure 10	Scaling of the average magnetic moment versus the energy scale $\Omega$ for the RTFIM. The different curves corresponds to different $L$ .	35
Figure 11	Scaling of the number of remaining clusters $L$ with the largest energy $\Omega$ for the RTFIM.	36
Figure 12	Two-dimensional square lattice of the Potts model.	36
Figure 13	Average magnetization $\mu$ versus the lattice length $L$ for $q = 2$ to 8 Potts states. Different curves correspond to different numbers of states $q$ .	41
Figure 14	Renormalization of the average magnetization $\mu$ with the length with $q = 2$ to 8 states.	42
Figure 15	Length scale versus energy for the Potts model with $q = 2$ to 8 states.	42
Figure 16	Ashkin-Teller chain with the couplings between the spins $\sigma_i$ and $\tau_i$ .	43
Figure 17	Ground-state phase diagram of the quantum random Ashkin-Teller model obtained in [41].	45
Figure 18	Schematic of the two dynamical exponents associated to magnetization and polarisation as a function of $\delta$ (from [41]).	45

- Figure 19 Magnetization for the random Ashkin-Teller model chain versus the field  $h$ . The different curves corresponds to different values of  $\epsilon = K_i/J_i$  and for lattice size  $L = 12$ . 48
- Figure 20 Polarization for the random Ashkin-Teller model chain versus the field  $h$ . The different curves corresponds to different values of  $\epsilon = K_i/J_i$  and for lattice size  $L = 12$ . 48
- Figure 21 Autocorrelation time  $\zeta_t$  estimated by the integration of the average spin-spin autocorrelation function  $A_\sigma(t)$ . The different graphs correspond to different values of  $\epsilon$  and the different curves to different lattice sizes  $L$ . 49
- Figure 22 Autocorrelation time  $\zeta_t$  estimated by the integration of the average polarization-polarization autocorrelation function  $A_{\sigma\tau}(t)$ . The different graphs correspond to different values of  $\epsilon$  and the different curves to different lattice sizes  $L$ . 50
- Figure 23 Phase diagram in the parameter in the parameter space  $(\epsilon, h)$  obtained from spin-spin (continuous lines) and polarization-polarization (dashed lines) first moment. 51
- Figure 24 Variance of disorder fluctuations of magnetization. The different graphs corresponds to different values of  $\epsilon$  and the different curves to different lattice sizes  $L$  52
- Figure 25 Variance of disorder fluctuations of polarization. The different graphs corresponds to different values of  $\epsilon$  and the different curves to different lattice sizes  $L$  53
- Figure 26 Spin-spin autocorrelation function of the random Ashkin-Teller chain versus time  $t$ . The different graphs correspond to different values of the transverse field  $h$ . The continuous lines correspond to a fit, either with ansatz (140) or with an exponential (141). 54
- Figure 27 Polarization-polarization autocorrelation function of the random Ashkin-Teller chain versus time  $t$ . The different graphs correspond to different values of the transverse field  $h$ . The continuous lines correspond to a fit, either with ansatz (140) or with an exponential (141). 55

- Figure 28 Inverse of the dynamical exponent  $z$  estimated from the spin-spin autocorrelation function, versus the transverse field  $h$ . The different curves correspond to different lattice sizes and the different graphs to different values of  $\epsilon$ . 57
- Figure 29 Inverse of the dynamical exponent  $z$  estimated from the polarization-polarization autocorrelation function, versus the transverse field  $h$ . The different curves correspond to different lattice sizes and the different graphs to different values of  $\epsilon$ . 58
- Figure 30 Renormalization of a cluster of strong bond  $J_b$ . (a) Lattice before renormalization, where the red cluster will be decimated out. (b) Lattice with the new effective field. 72
- Figure 31 Renormalization of a cluster of strong fields  $h$ . (a) Lattice before the renormalization, with a cluster of spins coupled to the same transverse field  $h$  and interacting via a next-neighbor interaction  $J_a$ . (b) The lattice after renormalization with the new effective interaction coupling at the location of the cluster. 73
- Figure 32 Maximum energy  $\Omega$  versus the lattice length  $L$  during the renormalization for the Paper-Folding sequence. The ratio of the couplings is  $\rho = J_b/J_a = 10$ . 78
- Figure 33 Average magnetization  $\mu$  versus the lattice size during the renormalization of the Ising chain with the Thue-Morse sequence. 80
- Figure 34 Average magnetic moment versus the lattice size during the renormalization of the Ising chain with the Paper-Folding sequence. 80
- Figure 35 Average magnetization  $\mu$  versus the lattice size  $L$  during the renormalization of the Ising chain with the Period-Doubling sequence. 82
- Figure 36 Average magnetization versus the lattice size during the renormalization of the Ising chain with the Three-Folding sequence. 82
- Figure 37 Average magnetization versus the lattice size during the renormalization of the Ising chain with the Rubin-Shapiro sequence. 83
- Figure 38 Sketch of the fit of the largest energy with the lattice length for an aperiodic sequence. The red points corresponds to the points that are considered in the fit. The line is the log-log fit. 84

- Figure 39 Largest energy  $\Omega$  versus the lattice length for three different values of the ratio  $\rho = 3, 6, 10$  in the case of the Fibonacci family of sequences (§ 5.3.1) when  $k = 2$ . Our estimates of the dynamical exponent  $z$  are shown in the legend. 85
- Figure 40 Energy scale versus the lattice length for three different values of the ratio  $\rho = 3, 6, 10$  with the corresponding non universal dynamical exponent  $z$  for the Paper-Folding sequence. 86
- Figure 41 Energy scale versus the lattice length for three different values of the ratio  $\rho = 3, 6, 10$  for the Period-Doubling sequence. 87
- Figure 42 Energy scale versus the lattice length for three different values of the ratio  $\rho = 3, 6, 10$  for the Three-Folding sequence. 88
- Figure 43 Energy scale versus the lattice length for three different values of the ratio  $\rho = 3, 6, 10$  for the Rudin-Shapiro sequence. 88
- Figure 44 Scaling of lattice length with energy for the Rubin-Shapiro sequence for coupling ratio  $\rho = 8$ . 89
- Figure 45 Renormalization of the average magnetization for the Potts model with  $q = 2, 3, 6, 8$  and 10 for the Paper-Folding sequence. 91
- Figure 46 Renormalization of the average magnetization for the  $q = 2, 3, 6$  and 9-state Potts models with the Period-Doubling sequence. The different curves correspond to different numbers of state  $q$ . The curves for  $q = 3, 6$  (red, green) are under the data of  $q = 9$  (blue). 92
- Figure 47 Renormalization of the average magnetic moment for the  $q = 2, 3, 5, 7$  and 9-state Potts model with a Three-Folding sequence. The different curves correspond to different states  $q$ . The curves of  $q = 5, 6$  (green, blue) are under the curve of  $q = 9$  (yellow). 94
- Figure 48 Renormalization of average magnetization for the Potts model of several numbers of state  $q$  with the Rubin-Shapiro sequence. 95
- Figure 49 Largest energy scale versus the lattice length for three different values of the ratio  $\rho = 3, 6, 10$  for the  $q = 2$  quantum Potts model with the marginal Paper-Folding sequence. 96

- Figure 50 Largest energy scale  $\Omega$  with the lattice size  $L$  for various numbers of states  $q$  for the Paper-Folding sequence with two different coupling ratios  $\rho$ . The different curves correspond to different  $q$ . 97
- Figure 51 Energy scaling with the lattice size for five values of the coupling ratio  $\rho$  of the Paper-Folding sequences of  $q = 3$  and  $q = 5$ . The different curves correspond to different ratios  $\rho$ . 98
- Figure 52 Dynamical exponent  $z$  with the coupling ratio  $\rho$  for several numbers of state  $q$  for Potts chains with the Paper-Folding sequence. The different curves correspond to different numbers of states  $q$ . 99
- Figure 53 Energy scaling with the lattice size for various states  $q$  of the Period-Doubling sequence for two different coupling ratios  $\rho$ . The different curves correspond to different  $q$ . 100
- Figure 54 Energy scaling with the lattice size for five values of the coupling ratio  $\rho$  for the Period-Doubling sequences and  $q = 4$  and  $q = 6$  Potts states. The different curves correspond to different ratios  $\rho$ . 101
- Figure 55 Dynamical exponent  $z$  with the inverse of coupling ratio  $\rho$  for several Potts  $q$ -aperiodic Period-Doubling sequences. The different curves correspond to different numbers of states  $q$ . 102
- Figure 56 Largest energy scale  $\Omega$  with the lattice size  $L$  for various numbers of states  $q$  for the Rubin-Shapiro sequence with two different coupling ratios  $\rho$ . The different curves correspond to different  $q$ . 103
- Figure 57 Largest energy scale  $\Omega$  with the lattice size  $L$  for five values of the coupling ratio  $\rho$  for the Rubin-Shapiro sequence with  $q = 5$  and  $q = 16$ . The different curves correspond to different ratios  $\rho$ . 104
- Figure 58 Dynamical exponent  $z$  versus the inverse of the coupling ratio  $\rho$  for several numbers of Potts  $q$  for the Rubin-Shapiro sequences. The different curves correspond to different numbers of states  $q$ . 105
- Figure 59 Infinite-system DMRG steps algorithm. The letters  $\alpha, \delta$  corresponds to blocks and  $\beta, \gamma$  to single sites. 122
- Figure 60 DMRG finite-size algorithm. 123

---

LIST OF TABLES

---

Table 1	Definitions of the critical exponents of a magnetic system. 20
Table 2	Critical exponents of the random transverse field Ising model. 29
Table 3	Exponent $\phi$ for the RTFIM model for five different lattice sizes. 34
Table 4	Exponent $\phi$ for the random quantum Ising model for lattice length $L_e$ . 35
Table 5	Exponent $\phi/2$ for the random quantum Potts model for a chain of length $L$ . The different ranges $L_a, L_b, L_c$ and $L_d$ are the windows where the fit has been performed. 41
Table 6	Wandering exponent $\omega$ of each sequence and cross-over exponent $\phi$ at the Ising and Potts critical points. The last two columns correspond to the Harris-Luck criterion prediction for the Ising and Potts model. Irr. means irrelevant, Marg. marginal and Rel. relevant. 70
Table 7	Critical exponent $\beta/\nu$ computed by SDRG method for the Ising chain with three marginal aperiodic sequences, and values of the pure and random quantum Ising chain. 83
Table 8	Dynamical exponents $z$ for three different ratios obtained by analytical and numerical SDRG approach for the marginal $k = 2$ Fibonacci sequence. 85
Table 9	Dynamical exponents $z$ for three different coupling ratios $\rho$ in the case of the marginal Period-Doubling sequence. 'exact' denotes the exact value obtained analytically in [77]. 'asympt.' is the value given by Eq. 205 and 'SDRG' our numerical estimate. 87
Table 10	Dynamical exponents $z$ for three different coupling ratios $\rho$ in the case of the marginal Three-Folding sequence. 'exact' denotes the exact value obtained analytically in [77]. 'asympt.' is the value given by Eq. 205 and 'SDRG' our numerical estimate. 87

Table 11	Critical exponent $\beta/\nu$ for the quantum $q$ -state Potts chain with a Period-Doubling sequence. $L$ denotes a fit over all data points while $L_a$ , $L_b$ and $L_c$ are limited fitting windows. 93
Table 12	Critical exponent $\beta/\nu$ for the Rubin-Shapiro sequence for the quantum $q$ -state Potts chain. $L$ denotes a fit over all data points while $L_a$ , $L_b$ are limited fitting windows. 94
Table 13	Dynamical exponents $z$ for three different ratios obtained by numerical SDRG approach for the marginal $q = 2$ quantum Potts states for the Paper-Folding sequence. 96

---

## RÉSUMÉ DÉTAILLÉ EN FRANÇAIS

---

### 1.1 INTRODUCTION

Les transitions de phase sont des phénomènes présentant un intérêt pour différents domaines de la physique et pour l'étude de la nature en général. En mécanique statistique, et plus particulièrement dans le domaine des phénomènes critiques, la recherche moderne sur les transitions de phase distingue les transitions de phase classiques et quantiques. L'exemple le plus familier d'une transition de phase classique est l'évaporation de l'eau provoquée par l'élévation de sa température mais on pourrait également citer les transitions qui résultent d'un changement de pression, d'une contrainte mécanique, d'une variation de potentiel chimique, etc. Les transitions de phase quantiques se produisent quant à elles à la température du zéro absolu. On trouve des transitions entre des phases ferromagnétique et paramagnétique mais il existe une pléthore d'autres transitions de phase quantiques, comme les transitions de phase chirale en chromodynamique quantique, les transitions de phase cosmologiques au début de l'Univers, etc. L'étude des transitions de phase intéresse également d'autres sciences, comme la chimie et la biologie.

Un grand progrès dans la compréhension du comportement critique a été le Groupe de Renormalisation de Wilson [7], qui a été appliqué avec succès aux problèmes de mécanique statistique (à l'échelle macroscopique) ainsi qu'aux interactions fondamentales (à l'échelle microscopique). D'autre part, la disponibilité d'ordinateurs toujours plus rapides a permis le développement de techniques de calcul qui ont conduit à beaucoup de nouveaux résultats importants en mécanique statistique. Les techniques numériques jouent aujourd'hui le rôle principal dans la recherche moderne sur les phénomènes critiques.

Une catégorie importante de systèmes statistiques, avec des applications en physique expérimentale, sont les systèmes inhomogènes, en particulier les matériaux désordonnés, ou aperiodiques comme les quasi-cristaux. Les circonstances dans lesquelles le désordre ou la modulation aperiodique sont capables de modifier le comportement critique d'un système pur et de conduire à une nouvelle classe d'universalité ont été étudiées en détail. Beaucoup d'attention a été donné aux transitions de phase quantiques [3], en particulier à la transition à température du zéro absolu entre les phases ferromagnétique

et paramagnétique de la chaîne quantique d'Ising dans un champ transverse avec une perturbation aléatoire ou apériodique des couplages.

Le comportement critique de la chaîne d'Ising quantique dans un champ transverse en présence de désordre est contrôlé par un point fixe de désordre infini, qu'on retrouve également dans d'autres chaînes de spins quantiques désordonnées. Très récemment, ce point fixe de désordre infini a été invoqué pour expliquer le comportement critique du même modèle mais avec une modulation apériodique des couplages. La motivation de cette thèse de doctorat est de mieux comprendre et d'explorer certains aspects des transitions de phase quantiques avec des perturbations aléatoires ou apériodiques dans d'autres chaînes de spin que le modèle d'Ising. Deux modèles de spins quantique nous ont particulièrement intéressés : la chaîne d'Ashkin-Teller, correspondant à deux chaînes d'Ising couplées par une interaction à quatre spins, et la chaîne de Potts à  $q$ -états pour laquelle les spins peuvent prendre  $q$  états différents. Pour la chaîne d'Ashkin-Teller, la région non-critique et, plus particulièrement la phase de Griffiths, n'avait pas été complètement étudiée. Pour la chaîne quantique de Potts, l'influence d'une perturbation apériodique n'avait pas été étudiée auparavant.

Dans ce mémoire, nous discutons nos principaux résultats, présentés dans les chapitres 5 et 6. Nous excluons le chapitre 3, qui est une introduction général aux phénomènes critiques et aux transitions de phase classiques et quantiques.

## 1.2 LES TRANSITIONS DE PHASE QUANTIQUE DE SYSTÈMES ALÉATOIRES

### 1.2.1 Renormalisation de désordre infini pour les modèles d'Ising

La chaîne d'Ising quantique avec un champ magnétique transverse est le modèle paradigmatique pour l'étude des transitions de phase quantiques [3]. Il est défini par le hamiltonien

$$H = - \sum_i J_i \sigma_i^z \sigma_{i+1}^z - \sum_i h_i \sigma_i^x, \quad (1)$$

où  $\sigma_i^x, \sigma_i^z$  sont les matrices de Pauli, agissant sur le  $i$ -ième spin de la chaîne. Le couplage  $J_i$  correspond à l'interaction d'échange avec les spins voisins  $i$  et  $i + 1$ . Par  $h_i$ , nous désignons le champ magnétique transverse qui agit sur tous les spins. Les deux couplages  $J_i$  et  $h_i$  sont des variables aléatoires indépendantes et distribuées suivant les lois  $P(J)$  et  $R(h)$ .

La méthode du groupe de renormalisation de désordre infini (SDRG) est la méthode la plus puissante pour étudier les systèmes quantiques désordonnés dont le comportement critique est contrôlé par un point de fixe de désordre infini (IDFP). La méthode a été introduite par Ma,

Hu et Dasgupta [25, 26] pour la chaîne de spins d'Heisenberg. Vingt années après, D. Fisher a étendu la méthode au modèle d'Ising avec un champ transverse et introduit l'idée de point de fixe de désordre infini [19].

La méthode consiste à éliminer de manière itérative les couplages les plus forts du système. On note  $\Omega \in \{J_i, h_i\}$  l'énergie du couplage le plus fort restant dans le système. Lorsque ce couplage est le couplage d'échange  $J_i$  entre les spins sur les sites  $i$  et  $i + 1$ , l'hamiltonien  $-J_i \sigma_i^z \sigma_{i+1}^z$  est tout d'abord diagonalisé. Les états fondamentaux sont les états ferromagnétiques  $|\psi\rangle_0 = a |\uparrow_i \uparrow_{i+1}\rangle + b |\downarrow_i \downarrow_{i+1}\rangle$ . Pour ces états, les deux spins  $\sigma_i$  and  $\sigma_{i+1}$  sont entièrement corrélés et se comportent comme un seul macro-spin de spin 1/2. En traitant avec la théorie des perturbations de second ordre, l'action des deux champs transverses  $h_i$  et  $h_{i+1}$  sur ces états fondamentaux, on obtient un champ transverse effectif agissant sur le macro-spin et donné par Fig. 9a et § .1.2 :

$$h_{\text{eff}} = \frac{h_i h_{i+1}}{J_i}. \quad (2)$$

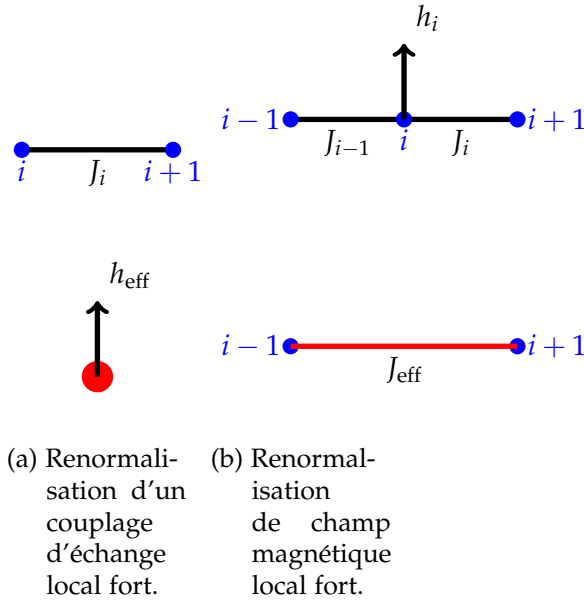


Figure 1: Règles de renormalisation pour le RTFIM.

Le second cas correspond à la situation où le plus grand couplage est un champ transverse  $h_i$  agissant sur le spin au site  $i$ . Contrairement au premier cas, l'état fondamental  $|\psi\rangle_0 = |\uparrow_x\rangle_i$  n'est pas dégénéré. Le spin  $\sigma_i$  est gelé et peut être décimé. Puisque ce spin interagit avec les spins  $\sigma_{i-1}$  et  $\sigma_{i+1}$  via les couplages d'échange  $J_{i-1}$  et  $J_i$ , un couplage effectif est généré par la théorie des perturbations (Fig. 9b et § .1.3) :

$$J_{\text{eff}} = \frac{J_{i-1} J_i}{h_i}. \quad (3)$$



et l'invariance sous le retournement simultané des deux spins  $\sigma_i$  et  $\tau_i$ . La brisure de ces symétries est contrôlée à l'aide des deux paramètres d'ordre

$$M = \sum_i \langle \sigma_i^z \rangle, \quad P = \sum_i \langle \sigma_i^z \tau_i^z \rangle \quad (5)$$

appelés aimantation et polarisation.

Les propriétés critiques du modèle quantique pur unidimensionnel, i.e.  $J_i = J$ ,  $K_i = K$ ,  $h_i = h$  et  $g_i = g$  [38], [42], [43] sont identiques à celles du modèle classique bidimensionnel [39] [44]. Le diagramme de phase du modèle AT aléatoire a été étudié par Carlon *et al.* [40] dans le régime  $\epsilon < 1$  en utilisant l'approche DMRG. Ils ont analysé l'effet de cross-over entre le régime de couplage fort et celui de couplage faible. Le comportement critique de la région de couplage fort,  $\epsilon > 1$  est contrôlé par le IRFP, comme le montre la méthode SDRG. La région de couplage faible,  $\epsilon < 1$  est contrôlée par le point de fixe du modèle pur. En utilisant l'approche SDRG, Hrahsheh *et al.* [45] ont prouvé que, pour une valeur fixée de  $\epsilon < 1$ , les couplages entre chaînes  $K_i$  et  $g_i$  sont non pertinents sur la ligne critique  $\delta = 0$  de sorte que le modèle se comporte comme deux chaînes d'Ising aléatoires non couplées. En approchant le point multicritique  $\delta = 0$  et  $\epsilon = 1$  (Fig. 17) le long des droites  $\epsilon = 1$  et  $\delta = 0$ , le comportement critique est régi par des exposants différents. Deux lignes de transition d'Ising émergent du point multicritique dans le régime  $\epsilon > 1$ . La technique SDRG indique l'existence d'une double phase de Griffiths, correspondant à une phase de Griffiths désordonnée pour le secteur magnétique et ordonnée pour le secteur électrique. Les deux paramètres d'ordre, l'aimantation et la polarisation,  $y$  présentent des singularités algébriques avec des exposants dynamiques  $z_m$  et  $z_p$  différents. Ces deux exposants dynamiques présentent une divergence pour une valeur différente de  $\delta$ , comme représenté sur la figure 18.

### 1.2.2.2 Diagramme de phase

#### *Temps d'auto-corrélation intégré*

Nous avons effectué des calculs numériques par renormalisation de la matrice densité (DMRG) et avons notamment étudié le diagramme de phase de la chaîne quantique aléatoire d'Ashkin-Teller dans le régime de couplage fort dans le but de mettre en évidence la double phase de Griffiths. Nous avons considéré les fonctions d'auto-corrélation spin-spin et polarisation-polarisation, définies comme

$$\overline{A_\sigma(t)} = \overline{\langle 0 | \sigma_{L/2}^z(t) \sigma_{L/2}^z(0) | 0 \rangle} - \overline{\langle m \rangle^2}, \quad (6)$$

$$\overline{A_{\sigma\tau}(t)} = \overline{\langle 0 | \sigma_{L/2}^z(t) \tau_{L/2}^z(t) \sigma_{L/2}^z(0) \tau_{L/2}^z(0) | 0 \rangle} - \overline{\langle p \rangle^2}. \quad (7)$$

Aux temps longs, les fonctions d'auto-corrélation  $\overline{A(t)}$  sont dominées par une décroissance exponentielle avec la variable  $t/\zeta_t$  où  $\zeta_t$  est le temps d'auto-corrélation. En effectuant une intégration de la fonction d'auto-corrélation, on a

$$\tau = \int_0^{+\infty} \overline{A(t/\zeta_t)} dt = \zeta_t \int_0^{+\infty} \overline{A(u)} du, \quad (8)$$

où  $\tau$  est le *temps d'auto-corrélation intégré*. Pour le système aléatoire, une divergence de  $\zeta$  et  $\zeta_t$  est attendue dans toute la phase de Griffiths. Cependant, dans un système fini, ces divergences sont lissées et remplacées par un pic fini. Le même comportement est attendu pour  $\tau$ . Nous avons calculé le temps d'auto-corrélation intégré  $\tau$  pour les corrélations spin-spin,  $A_\sigma(t)$  représentées à la Fig. 21, et pour les corrélations polarisation-polarisation,  $A_{\sigma\tau}(t)$ , Fig. 22. Les deux temps d'auto-corrélation présentent deux pics. Le premier pic reste fini et n'est associé à aucune transition de phase. Pour  $\epsilon \leq 1$ , l'emplacement du second pic est à peu près le même pour les deux temps d'auto-corrélation. Pour  $\epsilon > 1$ , le second pic apparaît pour un paramètre de contrôle  $\delta$  positif, ce qui correspond à un champ transverse  $h < 1$ , pour la fonction d'auto-corrélation spin-spin alors qu'on l'observe pour un paramètre négatif dans le cas des corrélations polarisation-polarisation. Ceci indique que le système subit deux transitions de phase, magnétique puis électrique.

Le diagramme de phase du modèle a également été obtenu par le premier moment des fonctions d'autocorrélation spin-spin et polarisation-polarisation. Il est présenté Fig. 23 et est qualitativement semblable à celui présenté en 17.

#### *Les fluctuations du désordre*

Un autre objet intéressant à étudier dans le cas des transitions de phase dans les systèmes désordonnés est la variance d'une quantité physique  $X$  donnée. Toute moyenne thermodynamique  $\overline{\langle X \rangle}$  est le résultat d'une moyenne quantique

$$\langle X \rangle = \langle \psi_0[J_i, K_i] X[\psi_0[J_i, K_i]] \rangle \quad (9)$$

suivie d'une moyenne sur les configurations de couplage

$$\overline{\langle X \rangle} = \int \langle \psi_0[J_i, K_i] X[\psi_0[J_i, K_i]] \rangle \wp(\{J_i, K_i\}) \prod_i dJ_i dK_i \quad (10)$$

où  $|\psi_0[J_i, K_i]\rangle$  est l'état fondamental de la chaîne d'AT pour une configuration de couplage donnée  $\{J_i, K_i\}$ , et  $\wp(\{J_i, K_i\})$  la probabilité de cette configuration. Les fluctuations du désordre sont mesurées par la variance

$$V_X = \overline{\langle X \rangle^2} - \overline{\langle X \rangle}^2. \quad (11)$$

Dans les systèmes qui sont contrôlés par un IDFP, comme le modèle d'AT aléatoire, les fluctuations du désordre dominent sur les fluctuations quantiques. Nous présentons la variance du désordre pour l'aimantation,  $V_\sigma$  en Fig. 24 et la polarisation,  $V_{\sigma\tau}$  en Fig. 25. Les deux variances sont numériquement très stables et présentent un pic, situé à la même valeur du paramètre  $\delta$  que le deuxième pic du temps d'auto-corrélation.

### 1.2.2.3 Exposants dynamiques

Les fonctions d'auto-corrélation spin-spin et polarisation-polarisation  $\overline{A(t)}$  de la chaîne d'AT quantique aléatoire sont présentés Fig. 26 et Fig. 27 respectivement. Les deux quantités présentent un comportement différent dans les différentes régions du diagramme de phase. Dans notre cas, nous nous sommes intéressés aux phases de Griffiths, où la dynamique est affectées par les régions rares de fortes concentration de couplages forts (ou faibles). Les fonctions d'autocorrélation  $y$  présentent une décroissance algébrique [47]:

$$\overline{A(t)} \sim t^{-1/z}, \quad (12)$$

avec un exposant dynamique  $z$ .

En raison des petites tailles de réseau que nous avons été en mesure d'atteindre numériquement par DMRG, la décroissance algébrique n'est pas observable pour les fonctions d'auto-corrélation spin-spin et polarisation-polarisation de la chaîne d'AT quantique aléatoire. Une décroissance algébrique est supposée se produire dans ce type de systèmes seulement pour des temps longs  $t \gg 1$  et dans la limite thermodynamique  $L \gg 1$ . Les données numériques de la fonction d'auto-corrélation dans la phase de Griffiths sont ajustées par une expression (ansatz) généralisant celle proposée par Rieger *et al.* à des systèmes de taille finie [47]. Pour rendre compte des points hors de la phase de Griffiths, une interpolation des données avec une décroissance purement exponentielle a également été opérée sur les figures 26 et 27.

Les données sont compatibles avec une décroissance exponentielle pour des grands champs transverses pour la fonction d'auto-corrélation spin-spin mais pour un petit champ transverse dans le cas d'une corrélation polarisation-polarisation, confirmant les diagrammes de phase des Fig. 17 et 23. D'autre part, pour des champs transverses intermédiaires, les données sont compatibles avec notre ansatz, ce qui confirme que nos données sont situées dans la phase de Griffiths.

L'inverse de l'exposant dynamique  $z$  est extrait et tracé avec le champ transverse  $h$  pour les corrélations spin-spin (Fig. 28) et polarisation-polarisation (Fig. 29). L'exposant dynamique de la fonction d'auto-corrélation spin-spin présente un pic qui est associé à la transition magnétique et, de manière correspondante, l'auto-corrélation polarisation-polarisation conduit à un pic associé à une transition électrique.

## 1.3 LES TRANSITIONS DE PHASE QUANTIQUES DE SYSTÈMES APÉRIODIQUE

## 1.3.1 Séquences apériodiques et matrice de substitution

Les séquences apériodiques sont générées par l'itération de règles de substitution sur des lettres  $A, B, \dots$ , telles que  $A \rightarrow S(A)$  et  $B \rightarrow S(B)$ .... Les propriétés des séquences apériodiques ainsi générées sont contrôlées par la matrice de substitution, qui est définie comme

$$\mathbb{M} = \begin{pmatrix} n_A^{S(A)} & n_A^{S(B)} & \dots \\ n_B^{S(A)} & n_B^{S(B)} & \dots \\ \vdots & \vdots & \ddots \end{pmatrix}, \quad (13)$$

où par exemple l'élément matriciel  $n_A^{S(A)}$  est le nombre de lettres  $A$  dans le motif  $S(A)$ .

Un exemple simple de système apériodique est la séquence *Thue-Morse* qui est donnée par les règles de substitution (pour simplifier, nous désignons ici les lettres  $A$  comme 0 et  $B$  comme 1)

$$S(0) \rightarrow 01 \quad S(1) \rightarrow 10.$$

Après les  $n$  premières itérations des règles de substitution, la séquence est

$$\begin{aligned} n = 0 & \quad 0, \\ n = 1 & \quad 01, \\ n = 2 & \quad 0110, \\ n = 3 & \quad 01101001, \\ n = 4 & \quad 0110100110010110, \\ & \quad \dots \end{aligned}$$

La matrice de substitution de la séquence Thue-Morse est

$$\mathbb{M}_{\text{thue-morse}} = \begin{pmatrix} 1 & 1 \\ 1 & 1 \end{pmatrix}.$$

Les fluctuations de la séquence apériodique sont contrôlées par l'*exposant de divagation* donné par

$$\omega \equiv \frac{\ln |\zeta_2|}{\ln \zeta_1}, \quad (14)$$

en fonction des deux valeurs propres de la matrice de substitution ( $\zeta_1 > \zeta_2$ ).

## 1.3.2 Critère de Luck

Pour les systèmes désordonnés, le critère de Harris [13] permet de déterminer si une perturbation aléatoire est pertinente ou non au point critique. Ce critère a été étendu aux systèmes apériodiques par

Luck [65,95]. Dans certaines circonstances, la modulation a périodique peut être une perturbation non pertinente, marginale ou pertinente au point fixe pur. Le critère de *Luck* (ou Harris-Luck) repose sur la comparaison de l'écart  $t$  au point critique avec les fluctuations de nature géométrique à une échelle de longueur  $\xi$ . Puisque la longueur de corrélation croît comme  $\xi \sim t^{-\nu}$  [64] au voisinage du point critique, on a le rapport

$$\frac{\overline{\delta t}}{t} \sim t^{-\phi}, \quad \phi = 1 + \nu(\omega - 1). \quad (15)$$

Lorsque l'exposant  $\phi$  est négatif, le rapport s'annule au point critique. L'apériodicité est alors une perturbation non pertinente. En revanche, quand  $\phi$  est positif, le rapport diverge et la modulation a périodique est une perturbation pertinente. Finalement, quand  $\phi = 0$ , la modulation a périodique est marginale et peut conduire le système à un comportement critique non universel. A partir du critère de Luck, nous voyons facilement que l'exposant de divagation  $\omega$  contrôle la pertinence des fluctuations géométriques.

Dans cette section, nous nous sommes intéressés à la modulation a périodique de chaînes de spin quantique d'Ising et de Potts. Dans le tableau 6, nous présentons la prédiction du critère Luck pour ces chaînes.

### 1.3.2.1 La chaîne quantique de Potts et l'approche SDRG

#### La chaîne quantique de Potts

Le modèle classique de Potts [29] est défini par l'hamiltonien

$$H = - \sum_{\langle i,j \rangle} J_{i,j} \delta_{\sigma_i, \sigma_j}. \quad (16)$$

Sur chaque site du réseau se trouve un *spin de Potts* prenant  $q$  états possibles, par exemple  $\sigma_i = \{0, 1, \dots, q-1\}$ . Lorsque  $q = 2$ , les deux états de Potts sont équivalents à des états d'Ising  $\pm 1$  par l'identité  $\delta(\sigma_i, \sigma_j) = \frac{1}{2}(1 + \sigma_i \sigma_j)$ . On retrouve alors le hamiltonien d'Ising en effectuant le changement  $J \rightarrow 2J$ .

En considérant le modèle classique 2D sur réseau carré et en prenant la limite anisotrope extrême, pour laquelle les interactions horizontales tendent vers zéro et les interactions verticale vers l'infini, la matrice de transfert conduit à l'hamiltonien quantique

$$H = - \sum_i \sum_{\sigma=0}^{q-1} J (\hat{\Omega}_i)^\sigma (\hat{\Omega}_{i+1})^{-\sigma} - \sum_i \sum_{\sigma=0}^{q-1} h N_i^\sigma. \quad (17)$$

où les opérateurs de Potts sont définis comme

$$\hat{\Omega}_i = \mathbb{1} \otimes \dots \otimes \mathbb{1} \otimes \begin{pmatrix} 1 & 0 & 0 & 0 \\ 0 & \omega & 0 & 0 \\ 0 & 0 & \omega^2 & 0 \\ 0 & 0 & 0 & \omega^3 \end{pmatrix} \otimes \mathbb{1} \otimes \dots \otimes \mathbb{1}$$

pour  $q = 4$  par exemple, avec  $\omega = e^{\frac{2i\pi}{q}}$ . Nous désignons les opérateurs échelle  $N_i |\sigma_i\rangle = |\sigma_i + 1\rangle$  comme

$$N_i = \mathbb{1} \otimes \dots \otimes \mathbb{1} \otimes \begin{pmatrix} 0 & 0 & 0 & 1 \\ 1 & 0 & 0 & 0 \\ 0 & 1 & 0 & 0 \\ 0 & 0 & 1 & 0 \end{pmatrix} \otimes \mathbb{1} \otimes \dots \otimes \mathbb{1}.$$

#### Règles SDRG pour la chaîne aléatoire

Dans le cas aléatoire où les couplages d'interaction entre spins proches voisins  $J_i$  et champs transverses  $h_i$  sont des variables indépendantes aléatoires, Senthil et Majumdar [37], ont montré par l'approche SDRG que le comportement critique du modèle de Potts quantique désordonné est contrôlé par le même IDFP que le modèle quantique d'Ising désordonné. Le nombre d'état  $q$  n'est donc pas pertinent. Par conséquent, les deux modèles appartiennent à la même classe d'universalité.

Comme dans le cas de la chaîne quantique désordonnée d'Ising, l'approche SDRG consiste en l'élimination itérative du plus grand couplage  $\Omega = \{h_i, J_i\}$ . Si ce dernier est le champ transverse  $h_i$  sur un site  $i$ , la partie dominante de l'hamiltonien est  $-h_i \sum_{\sigma=1}^{q-1} N_i^\sigma$ . Le spin de Potts  $|\sigma_i\rangle$  est gelé dans l'état fondamental  $|\sigma_i\rangle = \frac{1}{\sqrt{N}}(|0_i\rangle + |1_i\rangle + \dots + |(N-1)_i\rangle)$ . Le spin peut donc être décimé et, en utilisant la théorie des perturbations, un couplage effectif est introduit entre ses voisins (détails dans l'annexe .2.2)

$$\tilde{J} = \frac{J_{i-1}J_i}{\kappa h_i}, \quad (18)$$

où  $\kappa = q/2$ .

Par ailleurs, si le plus grand couplage correspond à une interaction  $J_i$  alors la partie dominante de l'hamiltonien est  $-J_i \hat{\Omega}_i^\sigma \hat{\Omega}_{i+1}^{-\sigma}$ . Dans l'état fondamental, les deux spins de Potts se trouvent toujours dans le même état. Ils se comportent comme un unique macro-spin de Potts. Par la théorie des perturbations, les deux champs  $h_i$  et  $h_{i-1}$  se combinent pour donner un champ effectif donné par (annexe .2.3)

$$\tilde{h} = \frac{h_i h_{i+1}}{\kappa J_i}. \quad (19)$$

### 1.3.2.2 Application à une famille aperiodique de séquences

Nous étendons les résultats de F.J. Oliveira Filho *et al* [91] pour la chaîne d'Ising quantique perturbée par une famille de séquences aperiodiques définie par les règles de substitution:

$$a \rightarrow ab^k, \quad b \rightarrow a \quad \text{for} \quad b^k \equiv \underbrace{bb \dots b}_{k \times \text{letters}} \quad (20)$$

ou  $k$  est un entier positif. Pour  $k = 1$ , on retrouve la séquence de *Fibonacci*.

Nous considérons le modèle de Potts quantique défini par l'hamiltonien (17) avec une modulation des couplages entre spins proches voisins suivant la famille de séquences aperiodiques ci-dessus. Les couplages prennent les deux valeurs  $J_a$  et  $J_b$ . Le champ magnétique transverse  $h$  est considéré comme uniforme sur tout le réseau. Les couplages sont supposés suivre l'inégalité  $J_a < h < J_b$ . En appliquant l'approche SDRG, les couplages effectifs obtenus après  $j + 1$  itérations du groupe de renormalisation peuvent s'exprimer sous forme matricielle

$$\begin{pmatrix} \ln r^{(j+1)} \\ \ln s^{(j+1)} \end{pmatrix} = \begin{pmatrix} k & -1 \\ -k & k+1 \end{pmatrix} \begin{pmatrix} \ln r^{(j)} \\ \ln s^{(j)} \end{pmatrix} + \begin{pmatrix} C_k \\ 0 \end{pmatrix}, \quad (21)$$

avec  $C_k = k \ln\left(\frac{2}{q}\right)$ .

La seule différence avec l'analyse effectuée pour la chaîne quantique d'Ising aperiodique est la présence de la constante  $C_k$ . Si le point fixe de ces équations de flot correspond à un point fixe de désordre infini alors nous nous attendons à ce que  $\ln r$  et  $\ln s$  divergent. En conséquence, la constante  $C_k$  qui, reste finie, devient infiniment plus petite que le reste de l'équation. Le nombre d'états  $q$  devrait alors être non pertinent au point fixe.

En calculer les exposants de divagation pour chaque valeur entière de  $k$ , on observe, suivant le critère de Luck pour le modèle de Potts, que l'aperiodicité est une perturbation non pertinente pour  $k = 1$ . Pour  $k = 2$ , la modulation aperiodique est marginale pour  $q = 2$  et pertinent pour  $q > 2$ . Enfin, pour  $k \geq 3$ , l'aperiodicité est pertinente pour tout  $q$ .

Pour tester cette prédiction, nous présentons dans la suite des calculs SDRG numériques pour les séquences aperiodiques de Thue-Morse, Paper-Folding, Period-Doubling, Three-Folding et Rudin-Shapiro.

### 1.3.2.3 Dimension d'échelle de l'aimantation

Dans le cas de la chaîne quantique aléatoire d'Ising avec un champ magnétique transverse, le comportement critique est régi par un point

fixe de désordre infini, caractérisé par un exposant dynamique infini  $z$ . Par conséquent, l'énergie maximale  $\Omega$  se comporte

$$\Omega_j \sim e^{-L^{-\psi}} \Leftrightarrow L \sim \left( \ln \frac{\Omega_I}{\Omega_j} \right)^{-1/\psi} \quad (22)$$

et l'aimantation comme

$$\mu^{(j)} \sim \left[ \ln \frac{\Omega_I}{\Omega_j} \right]^\phi, \quad (23)$$

avec l'exposant  $\phi = (\sqrt{5} + 1)/2$ . Dans les deux cas, l'énergie  $\Omega_I$  est une constante non universelle.

En combinant les équations (193) et (23), la dimension d'échelle magnétique  $x_m = \beta/\nu$  est obtenue à partir du comportement de l'aimantation avec la taille du réseau

$$\mu^{(j)} \sim L^{1-\beta/\nu}. \quad (24)$$

avec  $\beta = \nu(1 - \phi\psi)$ . En utilisant Eq. (195), nous avons calculé numériquement l'exposant critique  $\beta/\nu$ .

Pour le modèle d'Ising avec la séquence de Thue-Morse, nous savons déjà que l'apériodicité est une perturbation non pertinente, ce qui signifie que  $\beta/\nu$  doit prendre la valeur  $1/8$  du modèle pur, comme nous le voyons sur la fig. 33. Pour les autres séquences, le comportement d'échelle de l'aimantation avec la longueur de la chaîne est présenté sur les figures suivantes : Paper-Folding (fig. 34), Period-Doubling (fig. 35), Three-Folding (fig. 36) and Rudin-Shapiro (fig. 37). L'exposant critique  $\beta/\nu$ , a été extrait et est présenté dans le tableau 7.

Pour la chaîne de Potts, l'exposant pour les séquences de Paper-Folding (fig. 45), Three-Folding (fig. 47) et Period-Doubling (fig.46), est compatible avec l'exposant de la chaîne d'Ising et donc indépendant du nombre d'états  $q$ . Pour la séquence de Rudin-Shapiro (fig. 48), l'exposant présente une faible dépendance avec  $q$ .

#### 1.3.2.4 Estimation de l'exposant dynamique

Dans le cas de la chaîne aléatoire quantique d'Ising, la plus grande énergie  $\Omega$  se comporte avec la longueur du réseau comme

$$\Omega \sim L^z, \quad (25)$$

lorsque l'exposant dynamique  $z$  est fini.

Le comportement de  $\Omega$  en fonction de  $L$  est représenté schématiquement sur la Fig. 32. La courbe  $\Omega(L)$  n'est pas monotone, mais présente des marches. Chacune de ces marches correspond à la renormalisation de tous les couplages de même valeur. Pour extraire l'exposant  $z$ , nous avons considéré chaque marche et extrait la valeur de  $L$  au bord

de la marche. Une interpolation log-log est alors effectuée uniquement avec les points correspondant à ces bords de marche. Ils sont représentés par des points rouges sur Fig. 38.

Dans le cas de la chaîne d'Ising, nous présentons le comportement d'échelle et l'exposant dynamique obtenu à la section 5.3.2.2. Nos résultats sont comparés à l'expression exacte des séquences de F. Iglói *et al* [77], en fonction du rapport des couplage  $\rho = J_b/J_a$ . Avec l'approche SDRG, nous nous sommes seulement intéressés au cas de  $\rho$  grand. L'expression de [77] se réduit alors à sa forme asymptotique. On peut constater sur les figures que, à mesure que  $\rho$  devient grand, notre prédiction par SDRG numérique de l'exposant dynamique  $z$  se rapproche des résultats exacts de [77]. Pour la séquence de Rudin-Shapiro, nous avons conclu à l'existence d'un IDFP à partir de l'exposant critique  $\psi$ , comme cela avait déjà été fait par F. Filho Oliveira *et al.* [91].

Enfin, le comportement d'échelle de l'énergie  $\Omega$  avec la longueur de chaîne est étendu à la chaîne de Potts en 5.4.3. L'exposant dynamique obtenu augmente avec le nombre d'états  $q$  mais reste fini.

---

## INTRODUCTION AND OUTLINE

---

Phase transitions are one of the most common and probably most studied phenomena in nature with extensions in many areas of physics. In statistical mechanics, more specifically in the field of critical phenomena, the modern research is divided in classical and quantum phase transitions. The most familiar example of a classical phase transition, found even in school physics textbooks, is the temperature-driven transition of water boiling when heated. Other examples of classical phase transitions follow from changes in pressure, uniaxial stress, chemical potential, etc. Another kind of phase transition, occurring at absolute zero-temperature, is the quantum phase transition, whose most common example is the ferromagnetic to paramagnetic transition. Besides these examples, there are a plethora of such transitions in different fields of physics, such as the chiral and dilaton phase transitions of string theory in quantum chromodynamics, the cosmological phase transitions related to the strong and electroweak interactions in the early Universe, etc. Phase transitions are also found in many applications in chemistry and biology as well. Nowadays, many aspects of phase transitions can also be found in modern domains of complex systems theory like economical and social networks.

A big progress in the understanding of critical behavior was the Renormalization Group by Wilson [7], which was applied successfully to statistical mechanics problems (macroscopic scale) as well as to the fundamental interactions (microscopic scale). The exact solution of the 2D classical Ising model, or equivalently the mapping of the quantum Ising chain in a transverse field onto a free fermion gas [2], was also a major breakthrough. On the other hand, the availability of better and faster computers allowed for the development of computational methods which provided a lot of important results for statistical mechanics problems. Numerical techniques, nowadays, have a primary role in the modern research of critical phenomena.

An important category of systems with applications in experimental physics are inhomogeneous systems, for instance disordered metals, conductors, etc or aperiodic as quasicrystals. The circumstances under which disorder or aperiodic modulation is able to change the critical behavior of a clean system and lead to a new universality class were studied in detail. A lot of attention was given to quantum

phase transitions [3], in particular to the transition at absolute-zero temperature between the ferromagnetic and paramagnetic phases of the quantum Ising chain in a transverse field with random or aperiodic perturbations. The technological interest of these phenomena in condensed matter acted as an incentive of the study at the theoretical and experimental levels for other lattice spin chains and statistical models in general.

The critical behavior of the quantum Ising chain in a transverse field in presence of disorder is controlled by an infinite-disorder fixed-point, also present in other disordered quantum spins chains. Very recently, this infinite-disorder fixed-point was found to control the same model but with some aperiodic modulations. The motivation of this PhD thesis, is to better understand and to explore aspects of quantum phase transitions with random or aperiodic perturbations beyond the prototypical standard quantum Ising chain. Two very interesting quantum spin models are the Ashkin-Teller chain, a version of two coupled Ising chains and the  $q$ -state Potts chain, where the spins can take  $q$  states. For the Ashkin-Teller chain, the off-critical region and specially the Griffiths phase was not fully studied. For the quantum  $q$ -state Potts chain, the influence of an aperiodic perturbation has not been studied before.

Recently, a new kind of quantum disordered phase transition in condensed matter physics, the Many-Body Localization phase transition, attracted a lot of interest due to its possible experimental applications, like quantum memory and quantum information . This phase transition may also be present, not only in random systems, but also in aperiodic ones. Still, the number of spins chains where the many-body localization were confirmed is limited. We hope that our results for the random quantum Ashkin-Teller chain as well as in the aperiodic quantum Potts chain will be useful for a detailed exploration of this new phase of matter.

The thesis is divided into the following parts : in Chapter 3, we discuss the general aspects of phase transitions, in particular order-parameter, critical points and critical exponents and how they appear in physical quantities. Next, we introduce an experimental example of a quantum phase transition, the different phases and their location in the phase diagram. Some basic aspects of disordered systems are presented, as well as the important criteria stating under which circumstances disorder leads to a different universality class. Finally, we give a brief picture of the effects of rare regions in Griffiths phases.

In Chapter 4, we study the critical and off-critical properties of quantum random spin chains. We begin with the description of basic features and the critical behavior of the quantum random Ising chain in a transverse field. We introduce the Strong-Disorder Renormalization Group approach and we apply it to the quantum Ising chain, discussing the Infinite-Disorder Fixed Point uncovered by Fisher. Us-

ing a numerical implementation of SDRG, we extract the critical exponents and test the numerical approach. Subsequently, we apply the SDRG approach to the quantum random  $q$ -state Potts model confirming again by numerical calculations that the fixed point is the same IDFP as the Ising chain. Finally, we present a detailed study of the quantum random Ashkin-Teller chain using Density-Matrix Renormalization Group, focusing on the double Griffiths phase in the off-critical region.

In Chapter 5, we study the critical properties of aperiodic quantum spin chains. We give first a short overview of the achievements in the study of the critical behavior of classical and quantum systems with aperiodic perturbations. We present the basic mathematical description and properties of the aperiodic sequences that will be considered. We discuss the known results, based on an analytical SDRG approach, for the quantum Ising chain in the cases of irrelevant, marginal and relevant aperiodic perturbations. By numerical SDRG calculations, we extract the magnetic scaling dimension as well as the dynamical exponent for different sequences. Finally, we extend these analytical and numerical studies to the quantum Potts model.

A general conclusion of this thesis is given in Chapter 6.

In the appendices, we present the derivation of the SDRG rules of the quantum Ising and Potts chains. In a second part, we discuss the Infinite and Finite-Size DMRG algorithms.

---

INTRODUCTION TO PHASE TRANSITIONS

---

## 3.1 ASPECTS OF CLASSICAL PHASE TRANSITIONS

Consider a system of  $N$  atoms forming a crystal. Each atom carries a magnetic moment, denoted  $\vec{S}_i$  for the  $i$ -th atom, and referred to as a spin in the following for simplicity. The magnetic moments are supposed to be in thermal equilibrium. The probability that the system is in the configuration  $\mathcal{C}$  is given by the Boltzmann law

$$P[\mathcal{C}] = \frac{e^{-\beta E(\mathcal{C})}}{\mathcal{Z}} \quad (26)$$

where  $\beta = 1/kT$ .  $k$  is the Boltzmann constant,  $T$  is the absolute temperature and  $E(\mathcal{C})$  is the energy of the configuration  $\mathcal{C}$ . The quantity  $\mathcal{Z}$ , called *partition function* of the system and defined as

$$\mathcal{Z}(N, \beta) = \sum_{\mathcal{C}} e^{-\beta E(\mathcal{C})}, \quad (27)$$

has a crucial meaning in statistical mechanics: it is the generating function of the thermodynamic averages of the system in the equilibrium state. The expectation value of any physical observable  $\mathcal{O}$  is expressed as the statistical average over all configurations  $\mathcal{C}$ , with the weight given by the Boltzmann law

$$\langle \mathcal{O} \rangle = \mathcal{Z}^{-1} \sum_{\mathcal{C}} \mathcal{O}(\mathcal{C}) e^{-\beta E(\mathcal{C})}. \quad (28)$$

The *free-energy* of the system is related to the partition function by

$$\mathcal{Z}(N, \beta) = e^{-\beta F(N, \beta)}. \quad (29)$$

*Phase transition* (PT) is the phenomena by which some macroscopic observables of a physical system undergo an abrupt, sometimes discontinuous, change, signalling that the system goes from one phase to another one. The most common example of PT in nature is the transition between the solid, liquid and gaseous phases of matter [4] [5]. There are many other examples of PT in physical systems, as structural transitions between different cristallographic orderings [6], the

transition between superconducting and normal phases, or the transitions undergone in the early universe [7].

PT are classified in two categories, the *first-order* and *continuous* phase transitions. The first-order phase transitions are characterized by a jump of a first order derivative of the free energy, often the energy. In the example of the liquid-gas transition, the system absorbs or releases energy, the latent heat, when undergoing the transition. In contrast, second-order or *continuous phase transitions* are characterized by a vanishing latent heat. Many ferromagnetic-paramagnetic transitions are in this category, as well as transitions in superconductors and superfluids.

In most of the examples given above, the phase transition occurs when the temperature changes and crosses a *critical temperature*  $T_c$ . These are classical phase transitions driven by *thermal fluctuations*. Phase transitions are characterized by an *order-parameter*, a physical quantity which vanishes in one phase and is non-zero in the other. In a magnetic transition, the physical quantity which plays the role of the order-parameter is usually the *total magnetization*

$$\vec{M} = \sum_i \vec{S}_i. \quad (30)$$

In the paramagnetic phase, i.e. when  $T > T_c$ , the total magnetization has a zero mean value. Spins have no privileged direction, in agreement with the rotational symmetry of the Hamiltonian. In the ferromagnetic phase, i.e. when  $T < T_c$ , the total magnetization takes a finite value. A majority of spins are aligned in a spontaneously preferred spatial direction. The Hamiltonian symmetry is broken (*spontaneous symmetry breaking*). When  $T = T_c$ , the order parameter displays a singular behavior, expressed as a power law dependence with temperature or magnetic field. From these power laws, one can define *critical exponents*. When the system is coupled to an external magnetic field  $\vec{H}$  in the direction of the z-axis, the net magnetization in the same axis has a mean value

$$M(H, T) = \langle S_i^z \rangle \equiv \frac{1}{Z_i} \sum_i S_i^z e^{-\beta \mathcal{H}} = -\frac{\partial F}{\partial H}, \quad (31)$$

where  $\mathcal{H}$  is the Hamiltonian of the system. In the ferromagnetic phase, the *spontaneous magnetization* is a function of  $T$ :

$$M(T) = \lim_{H \rightarrow 0} M(H, T). \quad (32)$$

Near the critical temperature  $T_c$ , the spontaneous magnetization has an anomalous behavior, parametrized by the critical exponent  $\beta$

$$M = M_0(-t)^\beta, \quad t = (T - T_c)/T_c. \quad (33)$$

where  $t$  denotes the distance from the critical point. At the critical temperature  $T = T_c$  but under a non-vanishing magnetic field  $H \neq 0$ , the magnetization behaves as a power-law with an exponent  $\delta$ :

$$M(H, T_c) = M_0 H^{1/\delta}. \quad (34)$$

The *magnetic susceptibility* is defined as

$$\chi(H, T) = \frac{\partial M(H, T)}{\partial H}. \quad (35)$$

Close to the critical point, it presents a singularity which is expressed with a critical exponent  $\gamma$  as:

$$\chi(0, T) = \begin{cases} \chi_+ t^\gamma, & T > T_c \\ \chi_- (-t)^\gamma, & T < T_c \end{cases}. \quad (36)$$

Similarly, the specific heat is defined by

$$C(T) = \frac{\partial U}{\partial T}, \quad (37)$$

where  $U$  is the internal energy of the system. This quantity has a singularity near the critical temperature with a critical exponent  $\alpha$ :

$$C(T) = \begin{cases} C_+ t^{-\alpha}, & T > T_c \\ C_- (-t)^{-\alpha}, & T < T_c \end{cases}. \quad (38)$$

Experimentally, magnetic systems or liquids are studied using scattering processes which give access to *two-point correlation functions*. In the case of our magnetic system, the spin-spin correlation reads

$$G^{(2)}(i, j) = \langle \vec{S}_i \cdot \vec{S}_j \rangle. \quad (39)$$

When the system is invariant under translation and rotation, the correlation function can be expressed as a function of the distance between the two spins  $r_{ij} = |\vec{i} - \vec{j}|$ , i.e.  $G^{(2)}(i, j) = G^{(2)}(r_{ij})$ . In a region close to the critical point, for  $T < T_c$ , the spins are predominantly aligned along the same direction, so it is more convenient to study the correlation between their fluctuations around the mean value. The *connected correlation function* reads

$$G_c^{(2)}(r) = \langle (\vec{S}_i - \vec{S}_0)(\vec{S}_j - \vec{S}_0) \rangle = \langle \vec{S}_i \vec{S}_j \rangle - |\vec{S}_0|^2. \quad (40)$$

if  $\langle \vec{S}_i \rangle = \langle \vec{S}_j \rangle = \vec{S}_0$ . In the paramagnetic phase, for  $T > T_c$ , because there is no privileged direction, this mean value is zero. At

the critical point, the correlation function shows a power law behavior

$$G_c^{(2)}(r) \simeq \frac{1}{r^{d-2+\eta}}, \quad r \gg a \quad (41)$$

where  $\eta$  is called the *anomalous dimension* of the order parameter and  $a$  is the lattice spacing. Away from the critical point, i.e.  $T \neq T_c$ , correlations extend over a certain distance  $\xi$ , called the *correlation length*. This is the typical size of the region in which the spins take the same value, up to thermal fluctuations. The correlation function displays the asymptotic behavior

$$G_c^{(2)}(r) \simeq e^{-r/\xi}, \quad r \gg a. \quad (42)$$

The correlation length remains finite at the transition temperature of a first-order phase transition. In contrast, the correlation length diverges when approaching the critical point of a continuous phase transition with a critical exponent  $\nu$ :

$$\xi(T) = \begin{cases} \xi_+ t^{-\nu}, & T > T_c \\ \xi_- (-t)^{-\nu}, & T < T_c \end{cases}. \quad (43)$$

The critical exponents of a magnetic system are summarized in table 1.

Exponent	Definition	Condition
$\alpha$	$C \sim  T - T_c ^{-\alpha}$	$H = 0$
$\beta$	$M \sim (T_c - T)^\beta$	$T < T_c, H = 0$
$\gamma$	$\chi \sim  T - T_c ^{-\gamma}$	$H = 0$
$\delta$	$H \sim  M ^\delta$	$T = T_c$
$\nu$	$\xi \sim  T - T_c ^{-\nu}$	$H = 0$
$\eta$	$G_c^{(2)} \sim r^{-(d-2+\eta)}$	$T = T_c$

Table 1: Definitions of the critical exponents of a magnetic system.

### 3.2 QUANTUM PHASE TRANSITIONS

In contrast with the classical case, *quantum phase transitions* (QPT's) occur at absolute zero-temperature,  $T = 0$ . The system is therefore always in its quantum ground state. The latter depends on the parameters of the quantum Hamiltonian. By varying some of these parameters, one can jump from one ground state to another one with a different symmetry.

A common example of experimentally observed QPT is the magnetic phase diagram of  $\text{LiHoF}_4$  [8] as presented in Fig. 3. Due to its uniaxial anisotropy, the system behaves as an Ising ferromagnet.

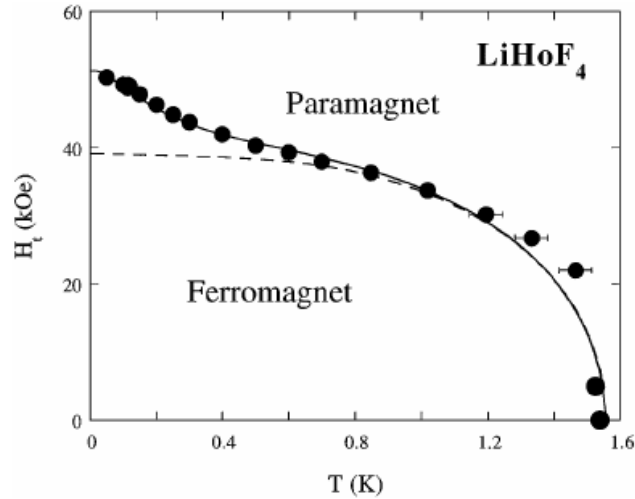


Figure 3: Phase diagram of LiHoF<sub>4</sub> as extracted by Bitko *et al.* [8]. Magnetic field versus the temperature. .

It undergoes a classical phase transition: when the temperature is increased above the critical temperature  $T_c \simeq 1.5^\circ\text{K}$  thermal fluctuations destroy the long-range ferromagnetic order and drive the system to the paramagnetic phase. At zero temperature, the system undergoes a QPT: by applying a transverse magnetic field, denoted as  $H_t$  in the phase diagram of Fig. 3, another phase transition is observed for a finite value of  $H_t$ . For a small magnetic field and keeping the temperature at a zero value, the system is in the ferromagnetic phase. By increasing the transverse magnetic field to a value called *critical field*, the system goes into the paramagnetic phase. The system has undergone a zero-temperature quantum phase transition driven by quantum fluctuations.

Other experimental examples of quantum transitions are : a) the magnetic phase transition of the alloy  $\text{SR}_{1-x}\text{Ca}_x\text{CuO}_3$  which undergoes a quantum phase transition from a ferromagnetic metal to a paramagnetic metal [9], b) Mott superfluid-insulator transition of an ultracold gas of bosons in an optical lattice produced by standing laser waves [10].

In analogy with the classical case, the point of the phase diagram where the different phases meet is called a *quantum critical point*. At this point, the ground state energy of the system is a non-analytic function of the parameters of the Hamiltonian (pressure, transverse magnetic field or interaction strength). At the transition, the ground state and the first-excited state are exchanged. Denoting  $\Delta$  the energy difference between the ground state and the first excited-state, the

quantum critical point can be characterized by  $\Delta = 0$ . If the transition is driven by a parameter  $g$  of the quantum Hamiltonian,  $\Delta$  scales as

$$\Delta \propto |g - g_c|^{\nu z}, \quad (44)$$

close to the critical coupling  $g_c$ .  $\nu$  and  $z$  are critical exponents. The equal-time correlation function  $G(r)$  of the order-parameter at two points separated by a distance  $r$ , decay exponentially in the vicinity of the critical point with a correlation length  $\xi$

$$G(r) = \langle O(0, t) O(r, t) \rangle - \langle O(0, t) \rangle \langle O(r, t) \rangle \propto \frac{e^{-r/\xi}}{r^{d-2+\eta}}. \quad (45)$$

As the critical point is approached,  $\xi$  diverges with the critical exponent  $\nu$  as

$$\xi \sim |g - g_c|^{-\nu}. \quad (46)$$

While the correlation length  $\xi$  defines a natural length scale of the system, a time scale is given by correlation time  $\xi_t$  associated to the equal-space autocorrelation function of the order-parameter. It scales with the energy difference  $\Delta$  as

$$\xi_t \sim \Delta^{-1}. \quad (47)$$

From equations (46), (47), and (44), one can write

$$\xi_t \sim \xi^z \propto |g - g_c|^{-\nu z} \quad (48)$$

which means that in QPT, space and time are connected, something which is in contrast with classical phase transitions. Because, at the critical point the correlation length and correlation time are both infinite, quantum fluctuations occur at any length and time scales. As a result, the system is scale-invariant. All observables (magnetization, susceptibility, e.t.c.) display a power-law behavior near the critical point

$$\mathcal{M} \propto \begin{cases} (g - g_c)^\beta, & g < g_c \\ 0, & g > g_c \end{cases}. \quad (49)$$

Quantum effects are important for the system as long as the energy of quantum fluctuations, of the order of  $\Delta$ , is larger than the energy of thermal fluctuations  $k_B T$ . In the region where  $k_B T$  dominates, the classical description applies and the phase transitions is driven by thermal fluctuations.

The phase diagram of a system undergoing a quantum phase transition at finite temperature is shown on Fig. 4. Long-range order can be destroyed by either thermal or quantum fluctuations. Depending on which one dominate, the system will be found in a thermally dis-

ordered or quantum disordered phase. In between, there exists a quantum critical region.

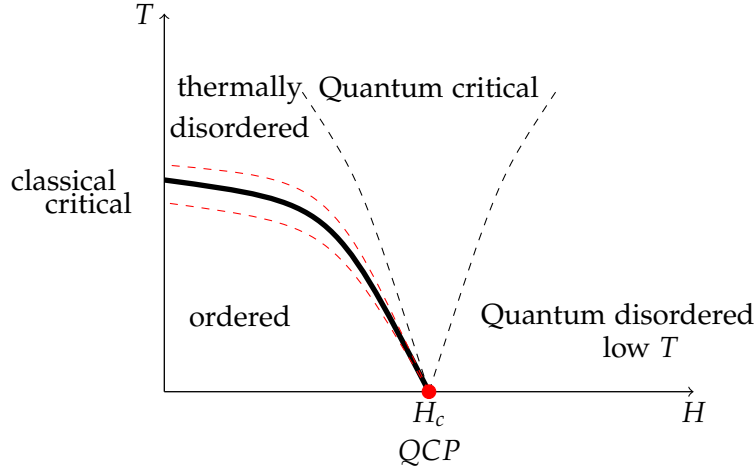


Figure 4: Schematic phase diagram of a system undergoing a quantum phase transition. The critical lines are presented with the various phases. Figure inspired from [3] and [12].

In classical statistical physics, the partition function of a gas of particles can usually be factorized into a kinetic part and a potential or configurational one. This is not possible in quantum statistical physics because kinetic  $T$  (related to momentum) and potential  $V$  (related to position), do not commute so that  $e^{T+V} \neq e^T e^V$ . The problem is solved by the Trotter identity [11]

$$e^{A+B} = \lim_{N \rightarrow \infty} \left[ e^{A/N} e^{B/N} \right]^N, \quad (50)$$

which can be applied to the partition function as follows:

$$Z = \text{Tr} e^{-\beta H} = \text{Tr} e^{-\beta(T+V)} = \lim_{N \rightarrow \infty} \prod_{n=1}^N (e^{-\beta T/N} e^{-\beta V/N}). \quad (51)$$

The Trotter formula *cuts* the inverse temperature  $\beta$  into many pieces. Moreover, the Boltzmann weights  $e^{-\beta A/N}$  are formally equivalent to evolution operators in imaginary time. Therefore, the partition function is equivalent to a quantum amplitude for a quantum system with an additional compactified imaginary time dimension  $\tau$ . The inverse temperature  $\beta$  plays the role of the size of this imaginary time dimension. *A classical phase transition in  $d + 1$  space dimensions is equivalent to a quantum phase transition in  $d$  dimensions.*

## 3.3 PHASE TRANSITIONS IN DISORDERED SYSTEMS

## 3.3.1 Quenched disorder

A huge research effort in statistical physics has been devoted to the study of the critical behavior of *disordered systems*. Examples of experimental disordered systems include vacancies, impurities or extended defects in crystals etc. *Disorder* or *randomness* can appear in two different types: *quenched* or *annealed*. In the former, defects or impurities are frozen while in the latter, they have their own dynamics and can redistribute themselves. In the following, we are interested only in *quenched disorder*.

An important issue that makes the analysis of disordered systems complex is that, for all thermodynamic quantities such as free-energy or magnetization, two averages need to be taken: over thermal or quantum fluctuations and over disorder. For the lattice spin models we are interested in, randomness can be introduced in the interaction coupling between neighbor spins,  $J$  or in the transverse field  $h$  (see Fig. 5).

$$J \longrightarrow J_{ij} \qquad h \longrightarrow h_i$$

Figure 5: The change from pure to random interaction constant and magnetic field.

The two quantum Hamiltonian parameters  $J$  and  $h$  become non-uniform and varies randomly from one lattice site to the other. When the disorder is introduced only in interaction coupling, it is called *random-mass disorder* because in quantum field theory (QFT), the randomness appears in the mass term. In contrast, when randomness is introduced in the transverse field, the resulting *random-field disorder* breaks locally the up-down ferromagnetic symmetry.

A very big issue in statistical mechanics is whether or not, and under which circumstances, the presence of disorder in statistical models is able to change the critical behavior and if yes in what sense. An argument for systems with mass-disorder was pointed out by Harris [13]. The powerful *Harris criterion* can be summarized into the inequality

$$d\nu > 2, \tag{52}$$

where  $d$  is the lattice spatial dimension and  $\nu$  is the correlation length exponent. If the inequality is fulfilled, the disorder does not affect the critical behavior of the system, which remains identical to the clean system. In contrast, when the inequality has the opposite sign, the critical behavior of the clean system is unstable and the disorder leads the system into a new universality class. Finally, for the marginal case  $d\nu = 2$ , the criterion is unproductive.

The Harris criterion should be modified for correlated random couplings. Weinrib and Halperin [14] showed that for algebraically decaying correlations of the form  $|x - x'|^{-a}$ , the Harris criterion (52) does not hold if  $a < d$  and should be modified instead as

$$\min(d, a)\nu > 2. \quad (53)$$

For random-field disorder, Imry and Ma [15] formulated a simple argument which predicts whether the random-field will destroy the ferromagnetic order or not. For dimensions  $d > 2$ , the ferromagnetic order is stable in presence of disorder while for  $d < 2$  the random-field destroys the order. Aizenman and Wehr [16] showed that the random field breaks the long-range order for  $d \leq 2$  in the case of discrete symmetry and for  $d \geq 4$  break the continuous symmetry.

### 3.3.2 Rare regions and Griffiths phase

As we discussed in 3.1, the order parameter as well as other thermodynamic quantities present a singular behavior at the critical point. The presence of disorder affects the system which presents a singular behavior not only at the critical point but also away. In the paramagnetic and ferromagnetic phases, these regions of singular behavior are called *Griffiths phases* or *Griffiths regions*, named by R. Griffiths [17].

In the paramagnetic phase, there exist rare regions of finite-size with a ferromagnetic order, Fig. 6. In the ferromagnetic Griffiths phase, the rare regions have a more complex structure: they are locally ordered *islands* decoupled from the rest of the system, Fig. 7. Inside the Griffiths phases, the free-energy is a singular function of an external control parameter. In the original paper of R. Griffiths [17], the control parameter is the magnetic field  $H$ .

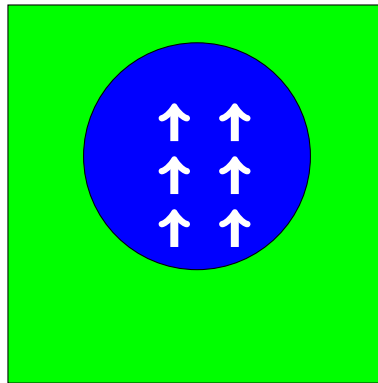


Figure 6: The paramagnetic Griffiths phase. Locally ferromagnetic rare regions (blue) inside a paramagnetic bulk (green).

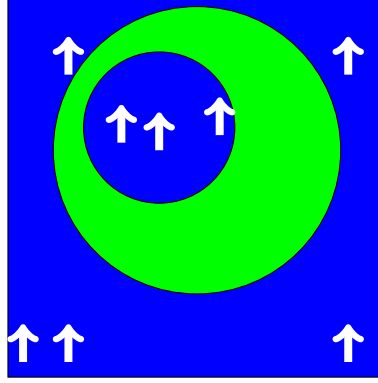


Figure 7: The ferromagnetic Griffiths phase. Locally ordered rare islands (blue) decoupled from the rest of the system by a paramagnetic shell (green).

We consider a disordered system in the paramagnetic Griffiths phase of Fig. 6 and we apply a weak magnetic field  $h$ . Locally ordered rare regions act as a large super-spin, with a magnetic moment proportional to its volume

$$\mu_{\text{rare}} \sim L_{\text{rare}}^d,$$

where  $L_{\text{rare}}$  is the linear size of the rare region and  $d$  the dimension of the space. The energy needed for the magnetic moment to be aligned by the external magnetic field  $h$  is  $|\Delta E| = -h\mu_{\text{rare}} \sim -hL_{\text{rare}}^d$ . If  $|\Delta E| > E_s$ , the rare region is fully polarized in the field direction while for  $|\Delta E| < E_s$ , it remains disordered,  $E_s$  is the energy of the system. The singular contribution to the total magnetization of the system in the Griffiths phase is estimated by summing all the rare regions which are aligned:

$$m_{\text{rare}} \sim \sum_{|\Delta E| > E_s} \rho_{\text{rare}} \mu_{\text{rare}},$$

$\rho_{\text{rare}}$  is the probability of a locally ordered rare region which behaves as

$$\rho_{\text{rare}} \sim e^{-cL_{\text{rare}}^d}.$$

By performing the sum, Griffiths proved the existence of singularities in the thermodynamic limit under these assumptions. A similar analysis is applied to the ferromagnetic Griffiths phase.

---

 QUANTUM PHASE TRANSITION IN RANDOM SYSTEMS
 

---

## 4.1 THE RANDOM QUANTUM ISING CHAIN

## 4.1.1 The model

The random quantum Ising model in one-dimension is defined by the Hamiltonian

$$H = - \sum_i J_i \sigma_i^z \sigma_{i+1}^z - \sum_i h_i \sigma_i^x, \quad (54)$$

where the  $\sigma_i^x, \sigma_i^z$  are the Pauli matrices

$$\sigma^x = \begin{pmatrix} 0 & 1 \\ 1 & 0 \end{pmatrix}, \quad \sigma^z = \begin{pmatrix} 1 & 0 \\ 0 & -1 \end{pmatrix}$$

acting on the  $i$ -th spin of the chain.

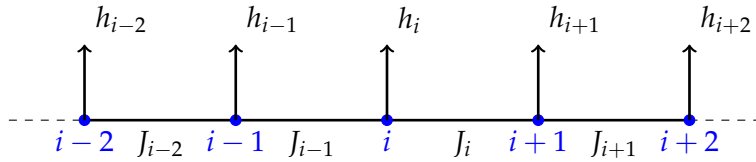


Figure 8: One-dimensional quantum Ising chain of Hamiltonian (54).

The coupling  $J_i$  corresponds to the interaction between spins on neighboring sites, i.e. the sites  $i$  and  $i + 1$ , and  $h_i$  is a transverse field which acts on every site, Fig. 8. Both the couplings  $J_i$  and the fields  $h_i$  are independent random variables distributed according to the probability distributions  $P(J)$  and  $R(h)$ . In the following, we restrict ourselves to positive couplings, i.e. we exclude any possibility of frustration. At zero temperature, the random Ising chain undergoes a quantum phase transition whose quantum control parameter is defined by

$$\delta = \frac{[\ln h]_{av} - [\ln J]_{av}}{\text{var}[\ln h] + \text{var}[\ln J]}, \quad (55)$$

where  $var$  is the variance of the coupling or the field. The symbol  $[..]_{av}$ , denotes the average over quenched disorder. The critical point is found when the transverse fields are related to the exchange couplings by  $\prod_i J_i = \prod_i h_i$  as proved by Pfeuty [18]. This condition is equivalent to  $\delta = 0$ . The quantum critical point separates a ferromagnetic phase, where the interaction couplings are larger than the fields,  $J_i \gg h_i$  ( $\delta < 0$ ) from a paramagnetic phase where the transverse fields are larger than the interactions,  $J_i \ll h_i$  ( $\delta > 0$ ).

The average magnetization of the model vanishes asymptotically [19] as

$$m \sim (-\delta)^\beta, \quad (56)$$

where

$$\beta = 2 - \phi, \quad \phi = \frac{1 + \sqrt{5}}{2} \quad (57)$$

$\phi$  is the golden-mean. The average surface magnetization behaves similarly but with a different critical exponent [20–22]

$$m_s \sim (-\delta)^{\beta_s}, \quad \beta_s = 1. \quad (58)$$

For a finite chain of length  $L$ , the surface magnetization scales at the critical point  $\delta = 0$  of the infinite system as

$$m_s \sim L^{-x_m^s}, \quad x_m^s = 1/2. \quad (59)$$

The average correlation function between two spins on two sites  $i$  and  $i + r$ ,  $G(r) \sim [\langle \sigma_i^x \sigma_{i+r}^x \rangle]_{av}$ , decays algebraically at the critical point:

$$G(r) \sim r^{-2x_m}, \quad x = \beta/\nu \quad (60)$$

where  $x_m$  is the scaling dimension of magnetization. Away from the critical point, the average correlation function  $G(r)$  decays exponentially with a correlation length  $\xi$  which asymptotically diverges [19] as

$$\xi \sim |\delta|^{-\nu}, \quad \nu = 2 \quad (61)$$

as the critical point is approached. In contrast, the typical correlation length decays with a different exponent

$$\xi_{typ} \sim |\delta|^{-\nu_{typ}}, \quad \nu_{typ} = 1. \quad (62)$$

At the critical point, the time scale,  $t_r$  and the length scale,  $\xi$  are related by

$$\ln t_r \sim \xi^\psi, \quad \psi = 1/2. \quad (63)$$

Such a relation is a consequence of an infinite dynamical exponent  $z$ . The critical exponents of the RTFIM are summarized in the table 2.

As we noted earlier, the critical point separates two phases, the *paramagnetic* and *ferromagnetic* phases. Both include so-called *Griffiths phases* [17,23,24] due to the existence of macroscopically large regions

$\beta$	$\beta_s$	$x_m$	$x_m^s$	$\nu$	$\nu_{typ}$	$\psi$
$(3 - \sqrt{5})/2$	1	$(3 - \sqrt{5})/4$	1/2	2	1	1/2

Table 2: Critical exponents of the random transverse field Ising model.

with a high density of strong (or weak) couplings that may display magnetic order before or after the rest of the system (§ 3.3.2). In the *ordered* or *disordered* Griffiths phases, the magnetic order of these clusters differs from the rest of the system. The probability to find a rare region is exponentially small. The energy gap is also exponentially small,  $\Delta E \sim e^{-A t_{rare}}$ , where  $A$  is a constant. One can show that in the Griffiths phase, time and length scales are related by an anisotropic scaling relation

$$t_r \sim \xi^z, \quad (64)$$

where the dynamical exponent  $z \neq 1$  depends on the distance from critically  $\delta$ .

#### 4.1.2 SDRG approach

The Strong-Disorder Renormalization Group (SDRG) approach is the most powerful method to study quantum disorder systems at an infinite-disorder Fixed point. Despite its simplicity, the method is expected to become exact at such a fixed point. The method was first introduced by Ma, Hu and Dasgupta for the random Heisenberg chain [25], [26]. Twelve years later, the method was extended by Fisher [19] to the random Ising chain in a transverse field. He managed to compute analytically exact values of various critical exponents, as well as scaling functions [27].

##### 4.1.2.1 RG rules

For the RTFIM, the largest energy scale is associated either to an exchange interaction or to a transverse field and is denoted as  $\Omega \in \{J_i, h_i\}$ . The ground state of the largest coupling, isolated from the rest of the system, is first determined. The full Hilbert state is truncated by a projection onto its ground state. Finally, effective interactions between the remaining degrees of freedom are obtained by second-order perturbation theory. Each iteration leads to a decrease of  $\Omega$ .

When the largest coupling is the exchange coupling  $J_i$  between the spins on sites  $i$  and  $i + 1$ , the part of the Hamiltonian which is diagonalized is  $-J_i \sigma_i^z \sigma_{i+1}^z$ . The ground states are the ferromagnetic states  $|\psi\rangle_0 = a |\uparrow_i \uparrow_{i+1}\rangle + b |\downarrow_i \downarrow_{i+1}\rangle$ . In these states the two spins  $\sigma_i$  and  $\sigma_{i+1}$  are fully correlated and behave as a single spin 1/2 macro-spin.

By treating with second-order perturbation theory the action of the two transverse fields  $h_i$  and  $h_{i+1}$  on these ground states, an effective transverse field acting on the newly defined macro-spin is obtained (Fig. 9a and § .1.2):

$$h_{\text{eff}} = \frac{h_i h_{i+1}}{J_i}. \quad (65)$$

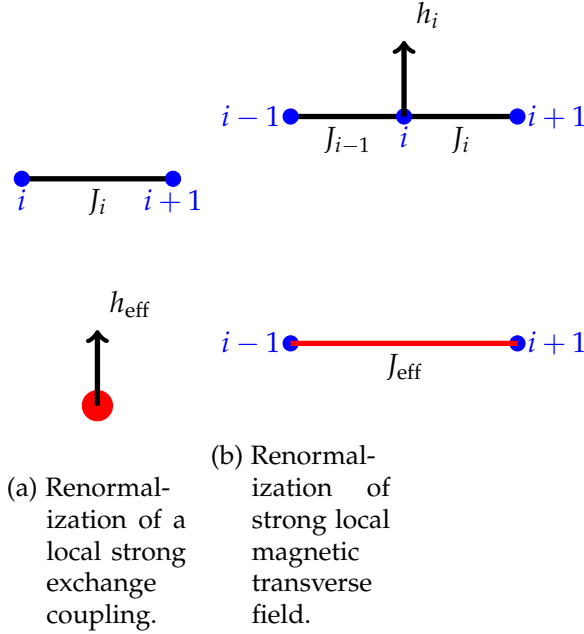


Figure 9: SDRG rules for RTFIM.

The second case corresponds to the situation where the largest local energy is a transverse field  $h_i$  acting on the spin at the site  $i$ . In contrast to the first case, the ground state is not degenerated:  $|\psi\rangle_0 = |\uparrow_x\rangle_i$ . As a result of the projection of the full Hilbert space onto this ground state, the spin  $\sigma_i$  is frozen and can be decimated out. Since this spin was interacting with the spins  $\sigma_{i-1}$  and  $\sigma_{i+1}$  via the exchange couplings  $J_{i-1}$  and  $J_i$ , an effective coupling is generated between them by perturbation theory (Fig. 9b and § .1.3)

$$J_{\text{eff}} = \frac{J_{i-1} J_i}{h_i}. \quad (66)$$

#### 4.1.2.2 RG flow

The couplings  $J_i$  and  $h_i$  are random variables whose distribution functions,  $P(J, \Omega)$  and  $R(h, \Omega)$ , evolve during the RG process. If the largest energy  $\Omega$  is lowered by  $d\Omega$ , i.e.  $\Omega \rightarrow \Omega - d\Omega$ , this amounts to

eliminating a number of couplings  $d\Omega[P(\Omega, \Omega) + R(\Omega, \Omega)]$ . The flow equation for the renormalization of an exchange coupling is

$$-dR(h; \Omega) = d\Omega P(\Omega; \Omega) \left[ -2R(h; \Omega) + \int dh_i dh_{i+1} R(h_i; \Omega) R(h_{i+1}; \Omega) \delta\left(h - \frac{h_i h_{i+1}}{\Omega}\right) \right] + d\Omega [R(\Omega; \Omega) + P(\Omega; \Omega)] R(h; \Omega). \quad (67)$$

The first term of the right part of Eq. (67) corresponds to the removal of the two fields  $h_i, h_{i+1}$ . The second term is associated to the introduction of a new effective one. The delta function in the integral enforces the SDRG rule. The third term of the Eq. (67) keeps the probability distribution  $R(h; \Omega)$  normalized at each RG iteration. In an analogous way, by replacing the probability distribution of fields with that of interactions,  $R(h; \Omega) \rightarrow P(J; \Omega)$  we get the flow equation for the renormalization of strong transverse fields. The RG flow equations for the decimation of transverse field or interaction coupling from the SDRG rules (65) and (66) are finally written in compact form as

$$-\frac{\partial P}{\partial \Omega} = [P_\Omega - R_\Omega]P + R_\Omega \int dJ_{i-1} dJ_i P(J_{i-1}; \Omega) P(J_i; \Omega) \delta\left(J - \frac{J_{i-1} J_i}{\Omega}\right). \quad (68)$$

$$-\frac{\partial R}{\partial \Omega} = [R_\Omega - P_\Omega]R + P_\Omega \int dh_i dh_{i+1} R(h_i; \Omega) R(h_{i+1}; \Omega) \delta\left(h - \frac{h_i h_{i+1}}{\Omega}\right), \quad (69)$$

where  $P = P(J; \Omega)$ ,  $R = R(h; \Omega)$ ,  $P_\Omega = P(\Omega; \Omega)$  and  $R_\Omega = R(\Omega; \Omega)$ . The flow equations (68) and (69) can be solved more easily by introducing logarithmic variables. The largest energy scale is parametrized by

$$\Gamma = \ln(\Omega_I / \Omega) \quad (70)$$

where  $\Omega_I$  is the initial value of the energy cutoff. The logarithmic variables for the coupling and the field are

$$\zeta = \ln(\Omega / J), \quad \beta = \ln(\Omega / h). \quad (71)$$

The flow equations in terms of the new variables (70) and (71) are now

$$\frac{\partial P}{\partial \Gamma} = \frac{\partial P}{\partial \zeta} + [P_0 - R_0]P + R_0 \int_0^\zeta d\zeta_i P(\zeta_i; \Gamma) P(\zeta - \zeta_i; \Gamma) \quad (72)$$

$$\frac{\partial R}{\partial \Gamma} = \frac{\partial R}{\partial \beta} + [R_0 - P_0]R + P_0 \int_0^\beta d\beta_i R(\beta_i; \Gamma) R(\beta - \beta_i; \Gamma) \quad (73)$$

with  $P = P(\zeta; \Gamma)$  and  $R = R(\beta; \Gamma)$  while  $P_0 = P(0, \Gamma)$  and  $R_0 = R(0, \Gamma)$ .

## 4.1.2.3 Fixed-point solution

The flow equations (110) and (111) have been solved exactly by Fisher [19]. He considered an exponential solution for each distribution function given by the ansatz

$$R(\beta; \Gamma) = R_0(\Gamma)e^{-R_0(\Gamma)\beta}, \quad P(\zeta; \Gamma) = P_0(\Gamma)e^{-P_0(\Gamma)\zeta}. \quad (74)$$

Both flow equations end up in the form

$$\frac{dP_0}{d\Gamma} = -R_0P_0 \quad (75)$$

$$\frac{dR_0}{d\Gamma} = -R_0P_0. \quad (76)$$

The flow equations (72) and (73) for  $P(\zeta; \Gamma)$  and  $R(\beta; \Gamma)$  are transformed to simpler differential equations for the coefficients  $P_0$  and  $R_0$ .

At the critical point for the RTFIM, first derived by Pfeuty [18], the product of the exchange couplings is equal to that of the transverse fields, i.e.  $\prod_i J_i = \prod_i h_i$ . The coefficients  $R_0$  and  $P_0$  are expected to be equal. The two flow equations (75) and (76) are written at the critical point

$$\frac{dR_0}{d\Gamma} = -R_0^2, \quad (77)$$

with solution

$$P_0 = R_0 = \frac{1}{\Gamma - \Gamma_0}.$$

Therefore, the fixed-point solution (with a redefinition of  $\Gamma$  to absorb the constant  $\Gamma_0$ ) of Eq. (74) is given by

$$R(\beta; \Gamma) = \frac{1}{\Gamma}e^{-\beta/\Gamma}, \quad P(\zeta; \Gamma) = \frac{1}{\Gamma}e^{-\zeta/\Gamma}. \quad (78)$$

The above fixed-point, identified by Fisher [19], is called *Infinite-Randomness Fixed-Point* (IRFP) or *Infinite-Randomness Critical point* because in the low energy limit  $\Gamma \rightarrow \infty$  the distribution functions (78) becomes arbitrarily broad. Equivalently, the randomness in the system become extremely strong.

During the renormalization procedure the lattice is reduced by one site. If  $n_\Omega$  is the number of remaining sites or clusters after renormalization at the energy scale  $\Omega$ , its variation is

$$dn_\Omega = -n_\Omega(P_\Omega + R_\Omega)d\Omega, \quad (79)$$

or in terms of the logarithmic variables

$$\frac{dn_\Gamma}{d\Gamma} = -(P_\Gamma + R_\Gamma)n_\Gamma = -\frac{2}{\Gamma}n_\Gamma \quad (80)$$

at the critical point. The solution of this equation is

$$n_\Gamma \sim \Gamma^{-2} \quad (81)$$

or in terms of the original variables

$$n_\Omega \sim \ln \left( \frac{\Omega_I}{\Omega} \right)^{-2}. \quad (82)$$

In the following, the number of remaining clusters  $n_\Omega$  will be referred to as the lattice size  $L$  of the chain at a given energy scale. Note that in general, one introduces an exponent  $\psi$  as

$$n_\Omega \sim \ln \left( \frac{\Omega_I}{\Omega} \right)^{-1/\psi} \quad (83)$$

which implies  $\psi = 1/2$  for the random Ising chain in a transverse field. In the following, the size of the lattice  $L$  will be identified for simplicity to the number of remaining clusters  $n_\Omega$ .

#### 4.1.2.4 Renormalization of lengths and magnetic moments

The renormalization of exchange couplings and transverse fields affects also the geometry of the lattice. The length of a bond,  $\ell_i^b$ , the size of a site  $i$ ,  $\ell_i^s$  and the magnetic moment of a cluster  $\mu_i$  also evolve during the renormalization. Initially, one has  $\ell_i^b = \ell_i^s = 1/2$  and  $\mu_i = 1$ . When a strong bond  $J_i$  is decimated out according to rule (65), the length of the site and the magnetic moment are renormalized as

$$\tilde{\ell}_{i,i+1}^s = \ell_i^s + \ell_i^b + \ell_{i+1}^s, \quad \tilde{\mu}_{i,i+1} = \mu_i + \mu_{i+1}. \quad (84)$$

When a strong field  $h_i$  is decimated out according to rule (66), the length of the new bond is

$$\tilde{\ell}_{i-1,i}^b = \ell_{i-1}^b + \ell_i^s + \ell_i^b. \quad (85)$$

The scaling of lengths and magnetic moments as the energy is lowered, was studied by Fisher [19] and presented later by Iglói [28]. They both studied the RG evolution of the probability distributions  $P(J; \Omega)$  and  $R(h; \Omega)$  inserting the RG rules for lengths and magnetic moments (84), (85). The average magnetic moment, after a lengthy mathematical calculation, is found to behave as

$$\bar{\mu} = \bar{\mu}_0 \left[ \ln \frac{\Omega_I}{\Omega} \right]^\phi, \quad \phi = \frac{1 + \sqrt{5}}{2} \quad (86)$$

where  $\bar{\mu}_0$  is a constant.

## 4.1.3 Numerical test

Here we present some elementary numerical SDRG calculations of the random Ising chain in a transverse field. We have considered lattice sizes up to  $L \simeq 10^6$ , which is large enough to have a good approximation of the thermodynamic limit. We have chosen a uniform distribution for both interaction couplings and transverse fields:

$$J_i \in [0, 1[ \quad \text{and} \quad h_i \in [0, 1[. \quad (87)$$

Only one realization of disorder has been considered.

In Fig. 10, we present the scaling of the average magnetization versus the energy  $\Omega$  for five different lattice sizes. As the largest energy  $\Omega$  is lowered during the renormalization process, the magnetization increases in agreement with the analytical prediction of Eq. (86). Performing a 3-parameter non-linear fit

$$\mu = a_1 \left( \ln \frac{a_2}{\Omega} \right)^{a_3} \quad (88)$$

for each lattice sizes  $L$ , we obtain estimates of the exponent  $\phi = a_3$ . These estimates are reported in table 3. As expected, the best fit, i.e. closest to the theoretical value, is obtained for the largest lattice length  $L_e$ . The smaller sizes,  $L_a$  to  $L_d$  are affected by strong finite-size effects. The critical regime is not reached yet by the renormalization procedure, unlike in the largest lattice size.

$L$	$\phi$
$L_a = 10^2$	1.40(4)
$L_b = 10^3$	1.42(1)
$L_c = 10^4$	1.444(4)
$L_d = 10^5$	1.454(1)
$L_e = 10^6$	1.589(1)

Table 3: Exponent  $\phi$  for the RTFIM model for five different lattice sizes.

Focusing now on the lattice size  $L_e = 10^6$ , we perform a log-log fit of the magnetization as

$$\mu \sim L^{-\phi/2} \quad (89)$$

where  $L = L(\Omega)$  is here the lattice size during the renormalization procedure, i.e. initially equal to  $L_e$  and decreasing each time a site is decimated. The result of the fit depends on the range of sizes where the fit is performed. In table 4, we present numerical estimates of the exponent  $\phi$  for different ranges of lattice sizes. The exponent for the middle window  $L_2$  is in very good agreement with the exact value Eq. (86), confirming that the renormalization group flows to

the IDFP. In the first window, the system has not reached the critical regime since most of the couplings have not been renormalized yet. In the last window  $L_3$ , the renormalization procedure has left too few lattice sites for the system to be critical.

$L$	$\phi$
$L_1 = 10^6 - 10^4$	1.489(1)
$L_2 = 10^4 - 10^2$	1.614(1)
$L_3 = 10^2 - 10^0$	1.578(6)

Table 4: Exponent  $\phi$  for the random quantum ising model for lattice length  $L_e$ .

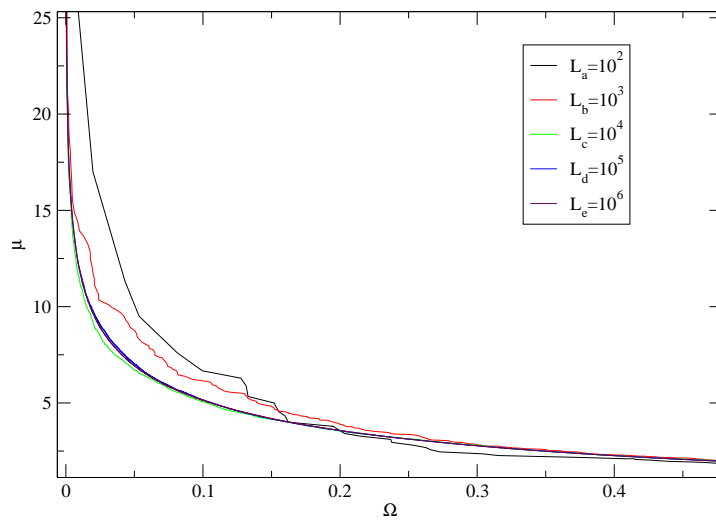


Figure 10: Scaling of the average magnetic moment versus the energy scale  $\Omega$  for the RTFIM. The different curves corresponds to different  $L$ .

The scaling of the number of remaining sites  $L$  with the largest energy  $\Omega$  is presented on Fig. 11. Again a 3-parameter non-linear fit, to the formula Eq. (83) as

$$L = a_1 \ln \left( \frac{a_2}{\Omega} \right)^{a_3} ,$$

is performed. The parameter  $a_2$  corresponds to the energy cut-off  $\Omega_I$ . We estimate the exponent as

$$1/\psi = 1.979(3) \tag{90}$$

which is close to the theoretical exponent  $1/\psi = 2$  given by Eq. (83).

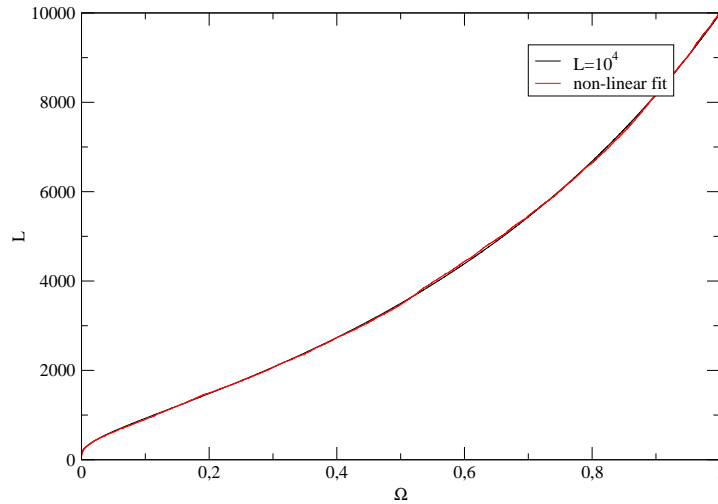


Figure 11: Scaling of the number of remaining clusters  $L$  with the largest energy  $\Omega$  for the RTFIM.

## 4.2 THE RANDOM QUANTUM POTTS MODEL

### 4.2.1 Hamiltonian limit

The classical Potts model [29] is defined by the Hamiltonian

$$H = - \sum_{\langle i,j \rangle} J_{i,j} \delta_{\sigma_i, \sigma_j}. \quad (91)$$

On each site of the lattice lies a *Potts spin* taking  $q$  possible states, i.e.  $\sigma_i = \{0, 1, \dots, q-1\}$ . The coupling  $J_{i,j}$  is the nearest-neighbor exchange interaction. The Hamiltonian (91) is invariant under the group  $Z_q$  of permutations of  $q$  objects. When  $q = 2$ , the two Potts states are mapped onto Ising spins  $\pm 1$  by using the identity  $\delta(\sigma_i, \sigma_j) = \frac{1}{2}(1 + \sigma_i \sigma_j)$ . The Ising Hamiltonian is recovered by making the change  $J \rightarrow 2J$ .

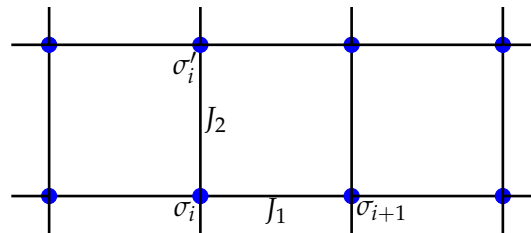


Figure 12: Two-dimensional square lattice of the Potts model.

The partition function of the Potts model on a finite lattice of  $N$  sites is given as a sum of the  $q^N$  terms

$$Z_N = \sum_{\{\sigma\}} \exp \left[ \beta \sum_{\langle ij \rangle} J_{ij} \delta(\sigma_i, \sigma_j) \right]. \quad (92)$$

On the 2D square lattice, the Hamiltonian of the Potts model [30] is given by

$$-\beta H = \sum_{x,y} J_1 \delta_{\sigma_{x,y}, \sigma_{x+1,y}} + \sum_{x,y} J_2 [\delta_{\sigma_{x,y}, \sigma_{x,y+1}} - 1] \quad (93)$$

where different couplings have been introduced on horizontal and vertical bonds (12). For convenience, a constant term has been added. The transfer matrix for the 2D classical Potts model is defined by [31] [32]

$$\mathcal{Z}_{L+1}(\sigma'_i, \sigma'_{i+1}, \dots) = \sum_{\sigma_i, \sigma_{i+1}} T(\sigma'_i, \sigma'_{i+1}, \dots; \sigma_i, \sigma_{i+1}, \dots) \mathcal{Z}_L(\sigma_i, \sigma_{i+1}, \dots) \quad (94)$$

where  $\mathcal{Z}_L(\sigma_1, \sigma_2, \dots)$  is the partition function of a strip of width  $L$  for which the spins are  $\sigma_i, \sigma_{i+1}, \dots$  on the last row. The transfer matrix can be written

$$\langle \sigma | T | \sigma' \rangle = \langle \sigma | U | \sigma \rangle \langle \sigma | V | \sigma' \rangle \quad (95)$$

where the horizontal part is given by

$$\langle \sigma | U | \sigma \rangle = \exp \left\{ \sum_i J_1 \delta_{\sigma_i, \sigma_{i+1}} \right\} \quad (96)$$

and the vertical one

$$\langle \sigma | V | \sigma' \rangle = \exp \left\{ \sum_i J_2 [\delta_{\sigma_i, \sigma'_i} - 1] \right\}. \quad (97)$$

In the following, we consider the extreme anisotropic limit  $J_1 \rightarrow 0$  and  $J_2 \rightarrow +\infty$ . Using the identity

$$\delta_{\sigma_i, \sigma_{i+1}} = \frac{1}{q} \sum_{\sigma}^{q-1} \exp \left[ i \frac{2\pi\sigma}{q} (\sigma_i - \sigma_{i+1}) \right], \quad (98)$$

the term (96) becomes to first-order in  $J_1$

$$U = 1 + \sum_i \frac{J_1}{q} \sum_{\sigma=0}^{q-1} (\hat{\Omega}_i)^\sigma (\hat{\Omega}_{i+1})^{-\sigma} \quad (99)$$

where the Potts operators (2.1) were defined as

$$\hat{\Omega}_i = \mathbb{1} \otimes \dots \otimes \mathbb{1} \otimes \begin{pmatrix} 1 & 0 & 0 & 0 \\ 0 & \omega & 0 & 0 \\ 0 & 0 & \omega^2 & 0 \\ 0 & 0 & 0 & \omega^3 \end{pmatrix} \otimes \mathbb{1} \otimes \dots \otimes \mathbb{1}$$

for  $q = 4$  for example, with  $\omega = e^{\frac{2i\pi}{q}}$ . The non-diagonal part of the transfer matrix (97) is

$$V = 1 + \sum_i \exp[-J_2] \sum_{\sigma=1}^{q-1} N_i^\sigma + \dots \quad (100)$$

where  $M$  is given in matrix form by

$$M_i = \sum_{\sigma=1}^{q-1} N_i^\sigma = \mathbb{1} \otimes \dots \otimes \mathbb{1} \otimes \begin{pmatrix} 0 & 1 & 1 & 1 \\ 1 & 0 & 1 & 1 \\ 1 & 1 & 0 & 1 \\ 1 & 1 & 1 & 0 \end{pmatrix} \otimes \mathbb{1} \otimes \dots \otimes \mathbb{1}.$$

$N_i$  is the ladder operator  $N_i |\sigma_i\rangle = |\sigma_i + 1\rangle$ . Finally, the two transfer matrices are rewritten

$$\begin{aligned} U &= 1 + \tau \sum_i^{L-1} J \sum_{\sigma=1}^{q-1} (\hat{\Omega}_i)^\sigma (\hat{\Omega}_{i+1})^{-\sigma} + O(\tau^2) \\ V &= 1 + \tau \sum_i^{L-1} h \sum_{\sigma=1}^{q-1} N_i^\sigma + O(\tau^2) \end{aligned} \quad (101)$$

where

$$J = \frac{J_1}{\tau q}, \quad h = \frac{\exp(-J_2)}{\tau}. \quad (102)$$

In the extreme anisotropic limit where  $J_1 \rightarrow 0$  and  $J_2 \rightarrow \infty$  [33], the two couplings of Eq. (102) remain finite for  $\tau \rightarrow 0$ . The transfer matrix of the classical system in  $d$ -dimensions is associated to the quantum Hamiltonian in  $(d-1)$ -dimensions [33] by the relation

$$T \equiv e^{-\tau H}, \quad \text{for } \tau \rightarrow 0. \quad (103)$$

Then by Eq. (95) and (101) we get the quantum Hamiltonian

$$H = - \sum_i \sum_{\sigma=0}^{q-1} J (\hat{\Omega}_i)^\sigma (\hat{\Omega}_{i+1})^{-\sigma} - \sum_i \sum_{\sigma=0}^{q-1} h N_i^\sigma. \quad (104)$$

The phase transition of the pure 1-dimensional quantum Potts model ( $J_i = J$  and  $h_i = h$ ) is equivalent to that of the (1+1)-classical model [30] [34]. Therefore, it undergoes a first-order transition for  $q > 4$  and

a second-order one for  $q \leq 4$ . All the critical exponents depends on the value of the number of states  $q$  [30] [35] [36].

#### 4.2.2 Strong-Disorder RG approach for the random quantum Potts model

The Hamiltonian of the one-dimensional quantum Potts model is given by [31] [32]

$$H = - \sum_i \sum_{\sigma=0}^{q-1} [J_i (\hat{\Omega}_i)^\sigma (\hat{\Omega}_{i+1})^{-\sigma} + h_i N_i^\sigma]. \quad (105)$$

We are interested in the random case where the interaction couplings between nearest-neighbor spins  $J_i$  and the transverse fields  $h_i$  are random independent variables (105). Senthil and Majumdar [37], showed by the SDRG approach that the critical behavior of the disordered quantum Potts are controlled by the same IRFP as the disordered quantum Ising model. Therefore the two models belong to the same universality class. This result was surprising because it was in contrast with the results for the classical models with homogenous disorder.

Here, we present the SDRG approach for the Potts model as well as a confirmation of the basic results of [37] by numerical simulations. We follow the same analysis as in section 4.1.2 for the SDRG approach of the RTFIM. We eliminate the strongest coupling  $\Omega = \{h_i, J_i\}$ . If the largest energy is the transverse field  $h_i$  on a site  $i$ , the dominant part of the Hamiltonian is  $-h_i \sum_{\sigma=1}^{q-1} N_i^\sigma$ . In the limit of a large field, the Potts spin  $|\sigma_i\rangle$  is frozen in the ground-state  $|\sigma_i\rangle = \frac{1}{\sqrt{N}}(|0_i\rangle + |1_i\rangle + \dots + |(N-1)_i\rangle)$ . The spin can therefore be decimated out and, using perturbation theory, an effective coupling is introduced between its neighbours (see the details in the appendix .2.2)

$$\tilde{J} = \frac{J_{i-1} J_i}{\kappa h_i}, \quad (106)$$

where  $\kappa = q/2$ .

On the other side, if the largest coupling corresponds to a bond  $J_i$  then the dominant part in the Hamiltonian is  $-J_i \hat{\Omega}_i^\sigma \hat{\Omega}_{i+1}^{-\sigma}$ . In the ground state, the two Potts spins are always found in the same state. They behave as a single  $q$ -state Potts macro-spin. By perturbation theory, the two fields  $h_i$  and  $h_{i-1}$  that act on the spins are combined in an effective field given (see .2.3) by

$$\tilde{h} = \frac{h_i h_{i+1}}{\kappa J_i}. \quad (107)$$

The flow equation for the probability distributions of the couplings and fields (68) and (69) is very similar to the Ising case:

$$-\frac{\partial P}{\partial \Omega} = [P_\Omega - R_\Omega]P + R_\Omega \int dJ_{i-1} dJ_i P(J_{i-1}; \Omega) P(J_i; \Omega) \delta\left(J - \frac{2J_{i-1}J_i}{q\Omega}\right) \quad (108)$$

$$-\frac{\partial R}{\partial \Omega} = [R_\Omega - P_\Omega]R + P_\Omega \int dh_i dh_{i+1} R(h_i; \Omega) R(h_{i+1}; \Omega) \delta\left(h - \frac{2h_i h_{i+1}}{q\Omega}\right). \quad (109)$$

In terms of the logarithmic variables (70) and (71) the flow equations are

$$\frac{\partial R}{\partial \Gamma} = \frac{\partial R}{\partial \beta} + [R_0 - P_0]R + P_0 \int_0^\beta d\beta_i R(\beta_i; \Gamma) R(\beta - \beta_i - \ln \kappa; \Gamma) \quad (110)$$

$$\frac{\partial P}{\partial \Gamma} = \frac{\partial P}{\partial \zeta} + [P_0 - R_0]P + R_0 \int_0^\zeta d\zeta_i P(\zeta_i; \Gamma) P(\zeta - \zeta_i - \ln \kappa; \Gamma). \quad (111)$$

Considering the fixed-point solution (74) for the Eq. (110) and (111), we extract the differential equations (75) and (76)

$$\begin{aligned} \frac{dP_0}{d\Gamma} &= -aR_0P_0 \\ \frac{dR_0}{d\Gamma} &= -bR_0P_0, \end{aligned} \quad (112)$$

with  $a = k^{P_0}$  and  $b = k^{R_0}$ . Therefore, the parameter  $\ln \kappa$  is irrelevant [37] at the fixed-point so that the critical behavior of the model is controlled by the IRFP (78). Senthil and Majumdar [37] also claimed that all other physical quantities are independent of  $q$  in the scaling limit.

### 4.2.3 Numerical test

We now perform the same analysis of numerical data produced by SDRG as for the Ising model (4.1.3) but for the quantum Potts model. We have considered several numbers of states  $q$ .

In order to test the validity of the exponent  $\phi$  of Eq. (86), we combine the equations (83) and (86) and write

$$\bar{\mu} \sim \bar{\mu}_0 L^{-\phi/2}. \quad (113)$$

On figure 13 we present the renormalization of the average magnetic moment with the lattice size for various number of states  $q$  with a lattice of length  $L = 10^6$  sites. The random exchange couplings and transverse fields are given by Eq. 87. We considered a single realization of disorder.

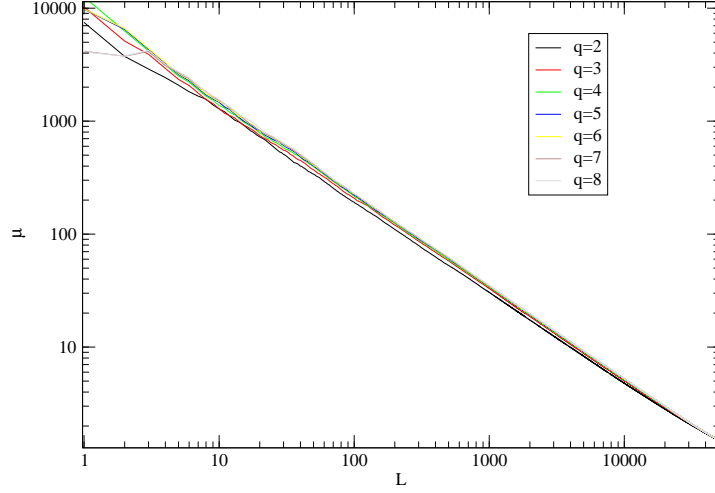


Figure 13: Average magnetization  $\mu$  versus the lattice length  $L$  for  $q = 2$  to 8 Potts states. Different curves correspond to different numbers of states  $q$ .

Performing a log-log fit of each curve of figure 13, we extract the exponent  $\phi/2$ . The results are presented in table 5. We studied five different ranges where the fit was performed: the full data  $L$ , as well as four windows  $L_a$ ,  $L_b$ ,  $L_c$  and  $L_d$ . The best agreement comes from the region  $L_b = 10^4 - 10^2$  where the extracted exponent is much closer to the exact value  $\phi/2 = 0.8090$ . We have to note that the error was  $\sim 10^{-4}$  in all cases. It is not reported in table 5.

$q$	$L = 10^6$	$L_a = 10^6 - 10^4$	$L_b = 10^4 - 10^2$	$L_c = 10^2 - 10^1$	$L_d = 10 - 1$
2	0.7864	0.7489	0.8012	0.8303	0.8335
3	0.7877	0.7728	0.8010	0.8045	0.8887
4	0.7956	0.7832	0.8017	0.8064	0.9408
5	0.8000	0.7894	0.8166	0.8160	0.8315
6	0.8036	0.7929	0.8189	0.8213	0.8228
7	0.8051	0.7929	0.8173	0.8226	0.8350
8	0.8070	0.7929	0.8192	0.8437	0.8456

Table 5: Exponent  $\phi/2$  for the random quantum Potts model for a chain of length  $L$ . The different ranges  $L_a$ ,  $L_b$ ,  $L_c$  and  $L_d$  are the windows where the fit has been performed.

On Fig. 14 is presented the scaling of the average magnetization with the lattice length. Performing the 3-parameter non-linear fit

$$\mu = a_1 \left( \log \frac{a_2}{\Omega} \right)^{a_3} \quad (114)$$

the corresponding exponent  $\phi = a_3$  is shown to be compatible with the exponent of the RTFIM for all values of  $q$ .

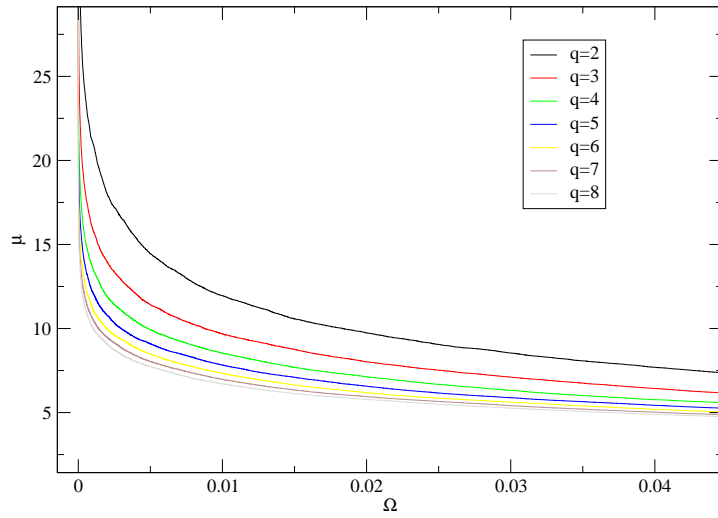


Figure 14: Renormalization of the average magnetization  $\mu$  with the length with  $q = 2$  to 8 states.

The same analysis is applied to (90) with the fit

$$L = a_1 \left( \log \frac{a_2}{\Omega} \right)^{a_3} \tag{115}$$

The exponent  $\psi = -1/a_3$  which is found to be similar for all the values of  $q$ , as can be seen on Fig. 15.

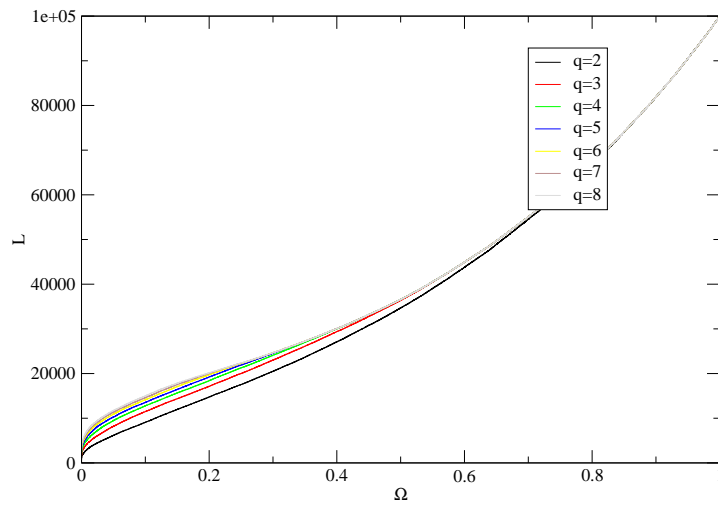


Figure 15: Length scale versus energy for the Potts model with  $q = 2$  to 8 states.

## 4.3 THE RANDOM QUANTUM ASHKIN-TELLER MODEL

## 4.3.1 The model

J. Ashkin and E. Teller [38] introduced an Ising-like classical lattice model with a four spin exchange interaction. The quantum Hamiltonian was obtained by Kohmoto *et al.* [39] as well as the phase diagram of the model. The phase diagram of the random model was studied by Carlon *et al.* [40] by DMRG and by Hrahsheh *et al.* [41] by SDRG.

The Hamiltonian of the random one-dimensional quantum Ashkin-Teller (AT) model is given by

$$H = - \sum_{a=1}^2 \sum_i (J_i \sigma_{a,i}^z \sigma_{a,i+1}^z + h_i \sigma_{a,i}^x) - \sum_i (K_i \sigma_{1,i}^z \sigma_{1,i+1}^z \sigma_{2,i}^z \sigma_{2,i+1}^z + g_i \sigma_{1,i}^x \sigma_{2,i}^x). \quad (116)$$

The model is equivalent to two coupled quantum Ising chains in a transverse field. The index  $a = 1, 2$  is referred to as a “color” in order to distinguish the two chains. As usual the coupling  $J_i$  denotes the interaction constant between nearest-neighbor spins and  $h_i$  is the transverse field which act on every spins. The two nearest-neighbor spins of one color interact with the two spins of the other color with a coupling  $K_i$ . Moreover, each spin of the first chain interacts in the  $\hat{x}$  direction with the corresponding spin of the second chain with the coupling  $g_i$ . In the following, we will use the parameters  $\epsilon_{J,i} = K_i/J_i$  and  $\epsilon_{h,i} = g_i/h_i$ . The AT model is invariant under the duality transformation  $\sigma_{a,i}^z \sigma_{a,i+1}^z \rightarrow \eta_{a,i+1}^x$ ,  $\sigma_{a,i}^x \rightarrow \eta_{a,i}^z \eta_{a,i+1}^z$ ,  $J_i \rightleftharpoons h_i$  and  $\epsilon_{J,i} \rightleftharpoons \epsilon_{h,i}$ , where  $\eta^x$  and  $\eta^z$  are the dual Pauli operators.

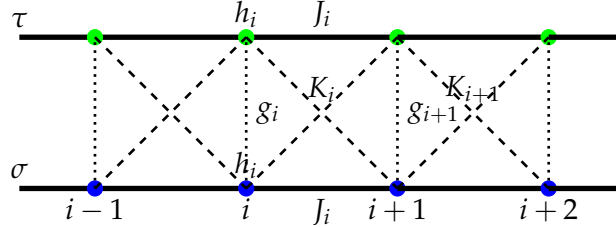


Figure 16: Ashkin-Teller chain with the couplings between the spins  $\sigma_i$  and  $\tau_i$ .

In the following, we will use the equivalent form of the Hamiltonian (116)

$$H = - \sum_i [J_i \sigma_i^z \sigma_{i+1}^z + h_i \sigma_i^x] - \sum_i [J_i \tau_i^z \tau_{i+1}^z + h_i \tau_i^x] - \sum_i [K_i \sigma_i^z \sigma_{i+1}^z \tau_i^z \tau_{i+1}^z + g_i \sigma_i^x \tau_i^x], \quad (117)$$

where  $\sigma_i$  and  $\tau_i$  denote the two spins  $\sigma_{a,i}$  (Fig. 16). The model possesses two  $\mathbb{Z}_2$ -symmetries, corresponding to the invariance of the Hamiltonian under the reversal of all spins  $\sigma_i$  (or  $\tau_i$ ) and of both  $\sigma_i$  and  $\tau_i$ . The breaking of these symmetries can be monitored using the two order parameters

$$M = \sum_i \langle \sigma_i^z \rangle, \quad P = \sum_i \langle \sigma_i^z \tau_i^z \rangle \quad (118)$$

referred to as magnetization and polarization. The critical properties of the 1d pure quantum model, where  $J_i = J$ ,  $K_i = K$ ,  $h_i = h$  and  $g_i = g$  [38], [42], [43] are identical to those of the classical 2d pure AT model [39] [44]. For  $\epsilon = K/J \in [-1/\sqrt{2}; 1]$ , the two  $\mathbb{Z}_2$ -symmetries are simultaneously broken and the AT model undergoes a single second-order quantum phase transition with the control parameter  $\delta = J/h$ . A critical line separates the paramagnetic ( $M = P = 0$ ) from the ordered or Baxter phase ( $M, P \neq 0$ ). When  $\epsilon > 1$  the critical line is splitted into two lines which separate the previous two phases from an intermediate mixed phase ( $M = 0, P \neq 0$ ). Both lines belongs to the Ising universality class.

The phase diagram of the random AT model was studied first by Carlon *et al.* [40] in the regime  $\epsilon < 1$  using the DMRG approach. The couplings where parametrized as

$$\frac{K_i}{J_i} = \frac{g_i}{J_i} = \epsilon \quad (119)$$

where  $\epsilon$  is a site-independent fixed parameter. The system undergoes a single quantum phase transition with the control parameter

$$\delta = \overline{\ln J} - \overline{\ln h}. \quad (120)$$

when  $\epsilon < 1$ . They analyzed the cross-over effect between the strong and weak-coupling regime. The critical behavior of the strong-coupling region,  $\epsilon > 1$  is controlled by the IRFP as shown by the SDRG method. On the other side, the weak-coupling region,  $\epsilon < 1$  is controlled by the fixed point of the pure model. Finally between these two regimes is located an intermediate one, where the model presents a non-universal critical behavior.

Using the SDRG approach, Hrahsheh *et al.* [45] proved that, for finite strength  $\epsilon$  at the critical line  $\delta = 0$ , the inter-chain couplings  $K_i$  and  $g_i$  are irrelevant and the model behaves as two uncoupled random Ising chains when  $\epsilon < 1$ . The phase diagram of the model [41] was found to be very similar to the pure AT model where the two Ising lines still meet at the tricritical or multicritical point located at  $\delta = 0$  and  $\epsilon = 1$ , Fig. 17. This line separates the ferromagnetic phase from the paramagnetic one. When the multicritical point is approached by varying  $\delta$ , the model is in the Ising universality class.

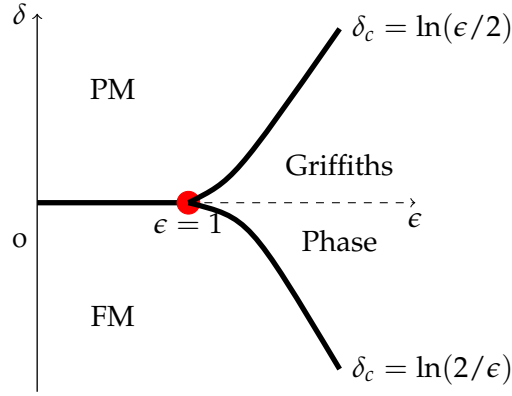


Figure 17: Ground-state phase diagram of the quantum random Ashkin-Teller model obtained in [41].

However, when approaching this point along the half-line  $\delta = 0$  and  $\epsilon > 1$ , the critical behavior is governed by different exponents:

$$\beta = \frac{6 - 2\sqrt{5}}{1 + \sqrt{7}}, \quad \nu = \frac{8}{1 + \sqrt{7}}. \quad (121)$$

Between the two Ising lines in the regime  $\epsilon > 1$ , SDRG indicates the existence of a double Griffiths phase. The two order parameters, magnetization and polarization, display power-law Griffiths singularities controlled by different dynamical exponents  $z_m$  and  $z_p$  respectively. The magnetic sector corresponds to a disordered Griffiths phase while the electric one is in an ordered Griffiths phase. Both dynamical exponents display a divergence but a different value of  $\delta$ , as depicted on figure 18.

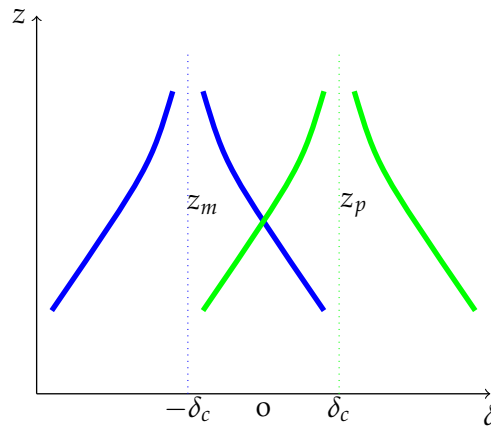


Figure 18: Schematic of the two dynamical exponents associated to magnetization and polarisation as a function of  $\delta$  (from [41]).

### 4.3.2 DMRG study of the random Ashkin-Teller model

In the following, we present a DMRG study of the random Ashkin-Teller model in the regime  $\epsilon > 1$ .

#### 4.3.2.1 Numerical Details

We consider for the exchange couplings  $J_i$  the binary distribution

$$\wp(J_i) = \frac{1}{2}[\delta(J_i - J_1) + \delta(J_i - J_2)]. \quad (122)$$

In our case, we assume that the two transverse fields  $h_i$  and  $g_i$  are uniform over all the lattice. The strength between the inter and intra-chain couplings is parametrized as

$$\frac{K_i}{J_i} = \frac{g}{h} = \epsilon. \quad (123)$$

This choice is made in order to minimize the number of disorder configurations. If  $L$  is the lattice size, the number of  $J_i$  couplings is  $L - 1$  when considering open boundary conditions, and the total number of disorder configurations is  $2^{L-1}$ . For simplicity, we consider the case

$$J_2 = 1/J_1 \Leftrightarrow \overline{\ln J_i} = 0 \quad (124)$$

and we have chosen a strong disorder by setting  $J_1 = 4$  and  $J_2 = 1/4$ . The quantum control parameter is now

$$\delta = -\ln h. \quad (125)$$

The critical properties of the AT model was obtained by the time-dependent Density-Matrix Renormalization Group approach (Appendix § .3). The ground-state was obtained by combining the Infinite-size DMRG algorithm .3.2.1 as well as the Finite-Size algorithm .3.2.2. Truncating the Hilbert space of the left or right block, we keep a number of  $m = 64$  states. The maximal truncation error was imposed to:  $10^{-5}$  during the initial Infinite-Size step,  $10^{-6}$ ,  $10^{-7}$ ,  $10^{-8}$  and  $10^{-9}$  during the Finite-Size sweeps.

The average magnetization and polarization densities are given by

$$\overline{\langle m \rangle} = \overline{\langle 0 | \sigma_{L/2}^z | 0 \rangle}, \quad \overline{\langle p \rangle} = \overline{\langle 0 | \sigma_{L/2}^z \tau_{L/2}^z | 0 \rangle}, \quad (126)$$

and were measured at the center of the chain.  $|0\rangle$  denotes the ground state and the over-line bar stands for the average over disorder. Non-vanishing averages are obtained by breaking the two  $\mathbb{Z}_2$  symmetries. We add a longitudinal magnetic field  $B$ , for the magnetization and a longitudinal electric field  $E$  for the polarization. The two fields

added to the two boundary spins of the chain are described by the Hamiltonian

$$H_1 = B\sigma_1^z + E\sigma_1^z\tau_1^z + B\sigma_L^z + E\sigma_L^z\tau_L^z. \quad (127)$$

We observed that, after imposing the two boundary fields, the convergence of DMRG algorithm becomes faster.

The spin-spin and polarization-polarization autocorrelation functions, defined as

$$\overline{A_\sigma(t)} = \overline{\langle 0 | \sigma_{L/2}^z(t) \sigma_{L/2}^z(0) | 0 \rangle} - \overline{\langle m \rangle^2}, \quad (128)$$

$$\overline{A_{\sigma\tau}(t)} = \overline{\langle 0 | \sigma_{L/2}^z(t) \tau_{L/2}^z(t) \sigma_{L/2}^z(0) \tau_{L/2}^z(0) | 0 \rangle} - \overline{\langle p \rangle^2}, \quad (129)$$

were estimated using a discretized imaginary-time evolution operator:

$$\overline{A_\sigma(n\Delta t)} = \left[ \frac{\langle 0 | \sigma_{L/2}^z (1 - H\Delta t)^n \sigma_{L/2}^z | 0 \rangle}{\langle 0 | (1 - H\Delta t)^n | 0 \rangle} \right] - \overline{\langle m \rangle^2} \quad (130)$$

We have used the values  $\Delta t = 10^{-3}$  and computed autocorrelation functions up to  $t = 10$ .

#### 4.3.2.2 Phase boundaries

The magnetization and polarization of the random AT model, calculated from the Eq. (126) are presented in Fig. 19 and 20. Both order parameters present the typical behavior of a system undergoing a single phase transition. The transition occurs at the same  $\delta$  for magnetization and polarization when  $\epsilon \leq 1$  but at different ones when  $\epsilon > 1$ .

However, because of the finite-size of the system, magnetization and polarization curves are too smooth to provide accurate estimates of the location of the transitions.

#### 4.3.2.3 Integrated autocorrelation time

A quantity that allows to get more accurate results about the location of the phase transition, is the correlation function. As we discussed for the RTFIM, in non-critical regions, the average spatial correlation function  $C(r)$  decays exponentially with a correlation length  $\xi$ . The same argument applies to correlation between spins in different time moments, provided by the average autocorrelation function  $A(t)$ , which decays with an autocorrelation time  $\xi_t$ . At large time  $t$ , connected autocorrelation functions  $\overline{A(t)}$  are dominated by an expo-

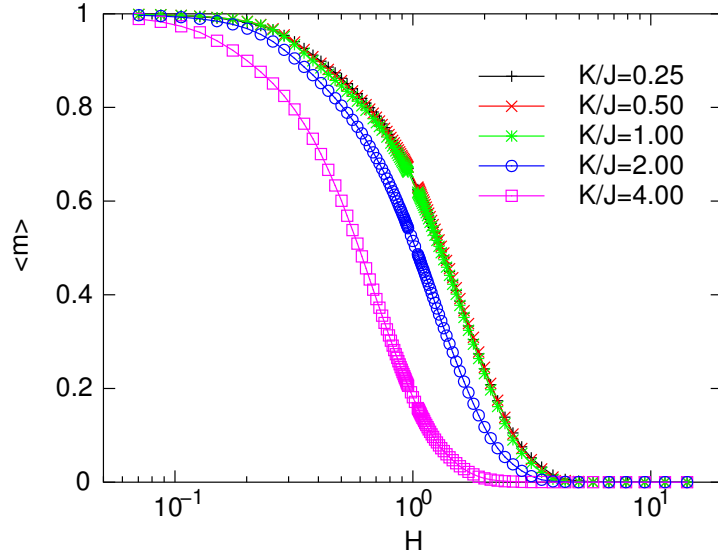


Figure 19: Magnetization for the random Ashkin-Teller model chain versus the field  $h$ . The different curves corresponds to different values of  $\epsilon = K_i/J_i$  and for lattice size  $L = 12$ .

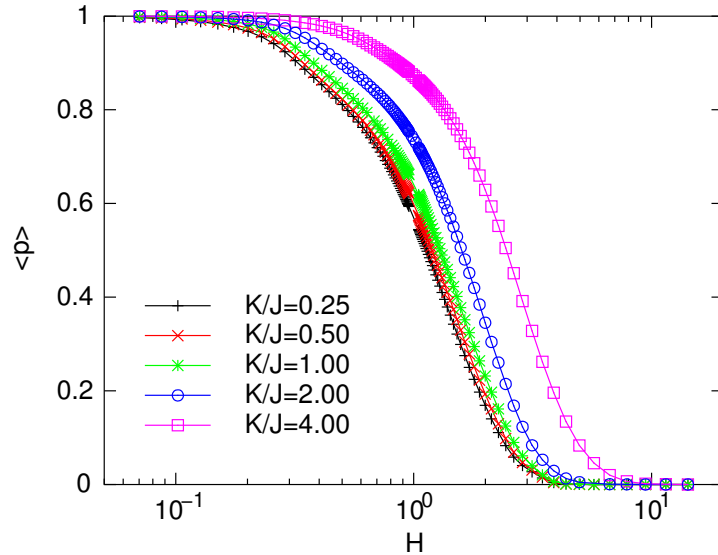


Figure 20: Polarization for the random Ashkin-Teller model chain versus the field  $h$ . The different curves corresponds to different values of  $\epsilon = K_i/J_i$  and for lattice size  $L = 12$ .

ponential decay of the variable  $t/\zeta_t$ . Performing an integration of the autocorrelation function we get

$$\tau = \int_0^{+\infty} \overline{A(t/\zeta_t)} dt = \zeta_t \int_0^{+\infty} \overline{A(u)} du, \quad (131)$$

where  $\tau$  is the *integrated autocorrelation time*. In the random system, a divergence of  $\zeta$  and  $\zeta_t$  is expected in the whole Griffiths phase. However, in a finite system, these divergences are smoothed and replaced

by a finite peak. The same behavior is expected for  $\tau$ . We have computed the integrated autocorrelation time  $\tau$  for spin-spin,  $A_\sigma(t)$  in Fig. 21, and polarization-polarization,  $A_{\sigma\tau}(t)$ , in Fig. 22, average autocorrelation functions. The upper bound of integral (131) was replaced by the largest time  $t = 10$  considered.

Both autocorrelation functions display two peaks. The first peak in both figures occurs for the value of the transverse field  $h \simeq 1/4$  which is in the same order with the weak coupling  $J_2$ . Therefore, this peak is probably associated to the ordering transition of the disorder configurations with a majority of weak couplings  $J_2$ . The height of this peak does not increase significantly with the lattice size so one can conjecture that this peak will remain finite in the thermodynamic limit and is not associated to any phase transition.

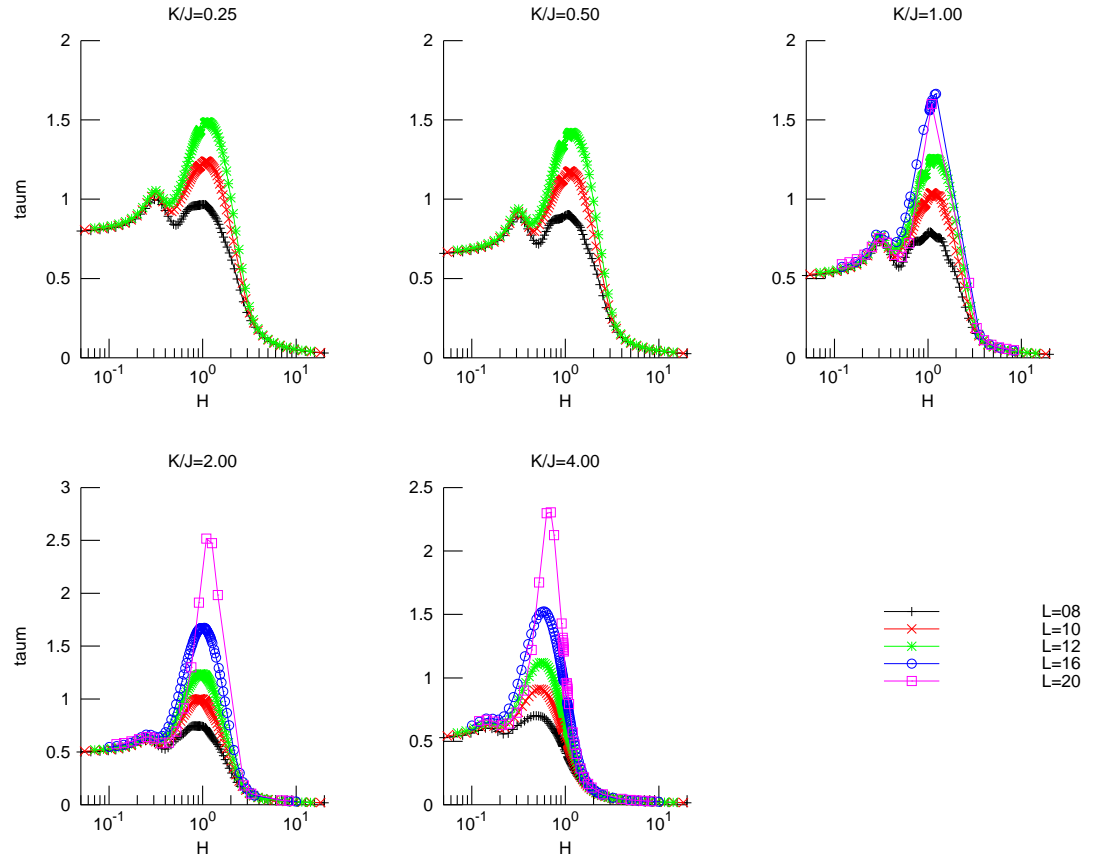


Figure 21: Autocorrelation time  $\zeta_t$  estimated by the integration of the average spin-spin autocorrelation function  $A_\sigma(t)$ . The different graphs correspond to different values of  $\epsilon$  and the different curves to different lattice sizes  $L$ .

The second peak increases with the lattice size. For  $\epsilon \leq 1$ , the location of the peak is roughly the same for both the autocorrelation times. In the other side for  $\epsilon > 1$  the peak occurs for positive

control parameter  $\delta$ , which corresponds to transverse field  $h < 1$ , for spin-spin autocorrelation function and negative field,  $h < 0$  for polarization-polarization ones. This indicates that the system undergoes a transition from magnetic to electric phase, as we discussed in the context of magnetization and polarization curves, 4.3.2.2. The location of the two transitions was predicted by Hrahsheh *et al.* [41] to be  $\delta_c = \pm \ln \frac{\epsilon}{2}$  for  $\epsilon \gg 1$ . For  $\epsilon = 4$ , as can be seen on Fig. 17, the two peaks are located at  $\delta_c = -\ln h_c \simeq 0.54$  and  $\delta_c \simeq -0.99$  for  $L = 16$  for instance, still far from  $\pm \ln \frac{\epsilon}{2} \simeq \pm 0.69$ . We note that, in contrast to Fig. 17, the transition lines are not symmetric around the point  $\delta = 0$  as required by self-duality. These difference can be understood by the fact that only small lattice sizes could be computed. Moreover, finite-size effects are enhanced by the two fields (magnetic and electric) on the boundaries (127) so that the phase diagram is shifted into the direction of the disordered Griffiths phase.

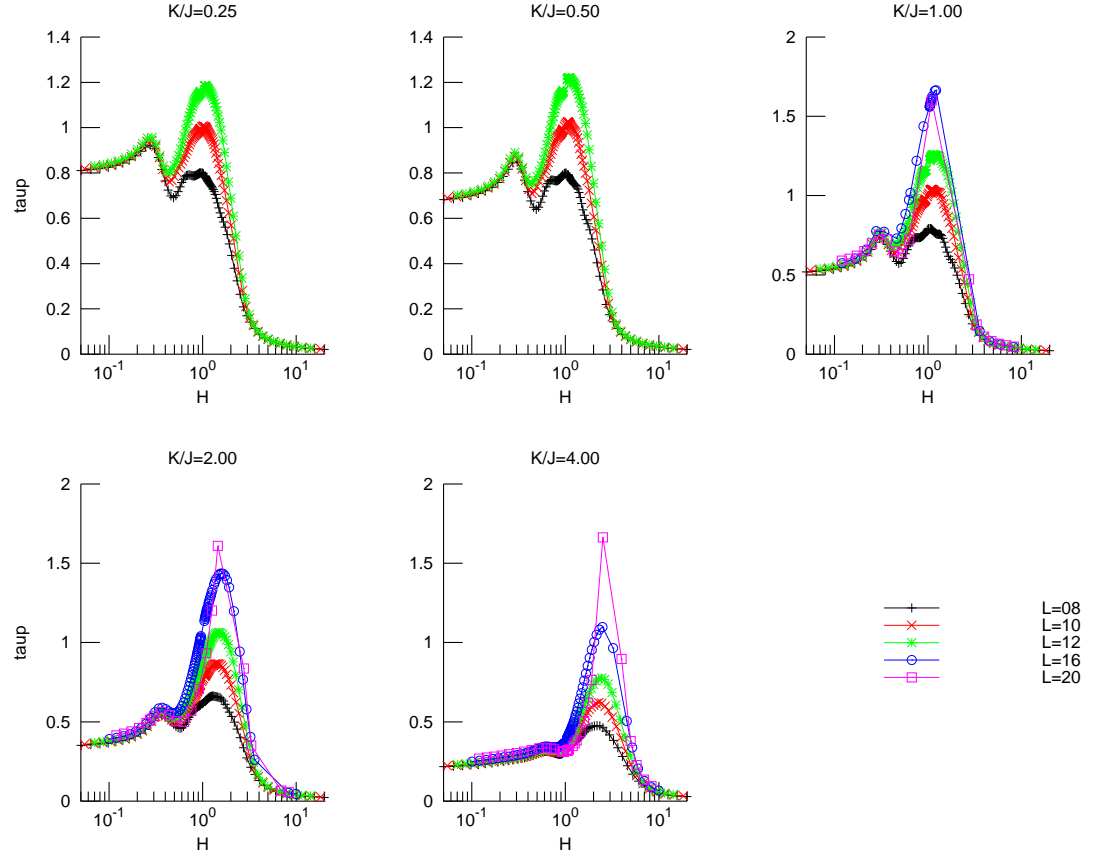


Figure 22: Autocorrelation time  $\zeta_t$  estimated by the integration of the average polarization-polarization autocorrelation function  $A_{\sigma\tau}(t)$ . The different graphs correspond to different values of  $\epsilon$  and the different curves to different lattice sizes  $L$ .

An other interesting object in our problem is the first moment, given by the expression

$$\int_0^{+\infty} t \overline{A(t)} dt / \int_0^{+\infty} \overline{A(t)} dt, \tag{132}$$

which, after integration, is equal to the autocorrelation time  $\zeta_t$  if the connected autocorrelation function  $\overline{A(t)}$  displays a purely exponentially decay  $\overline{A(t)} \sim e^{-t/\zeta_t}$ . The first moment for spin-spin and polarization-polarization autocorrelation time behaves similarly (figures 21 and 22).

The phase diagram of the model obtained by the first moment of spin-spin and polarization-polarization function is given by Fig. 23. It is qualitatively similar to the one presented in Fig. 17. However, it is not symmetric under the transformation  $\delta \leftrightarrow -\delta$ . As discussed above, finite-size effects are here strengthened by the boundary magnetic and electric fields that globally shift the phase diagram.

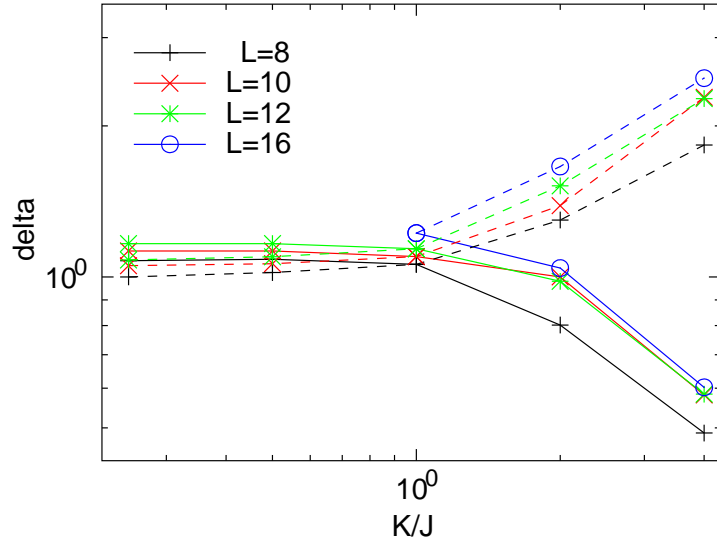


Figure 23: Phase diagram in the parameter in the parameter space  $(\epsilon, h)$  obtained from spin-spin (continuous lines) and polarization-polarization (dashed lines) first moment.

#### 4.3.2.4 Disorder fluctuations

Another interesting object to study phase transitions in disordered systems is the variance of a physical quantity  $X$ . In systems which are controlled by an IRFP, the disorder fluctuations dominate over quantum fluctuations. In the random AT model, any thermodynamic average  $\overline{\langle X \rangle}$  is the result of a quantum average

$$\langle X \rangle = \langle \psi_0 [J_i, K_i] X [\psi_0 [J_i, K_i]] \rangle \tag{133}$$

followed by an average over coupling configurations

$$\overline{\langle X \rangle} = \int \langle \psi_0[J_i, K_i] X[\psi_0[J_i, K_i]] \rangle \wp(\{J_i, K_i\}) \prod_i dJ_i dK_i \quad (134)$$

where  $|\psi_0[J_i, K_i]\rangle$  is the ground state of the AT chain for a given coupling configuration  $\{J_i, K_i\}$  and  $\wp(\{J_i, K_i\})$  the probability of this configuration.

The strength of the disorder average is measured by the variance

$$V_X = \overline{\langle X \rangle^2} - \overline{\langle X \rangle}^2. \quad (135)$$

We present the variance of the disorder average of magnetization,  $V_\sigma$  on Fig. 24 and polarization,  $V_{\sigma\tau}$  on Fig. 25.

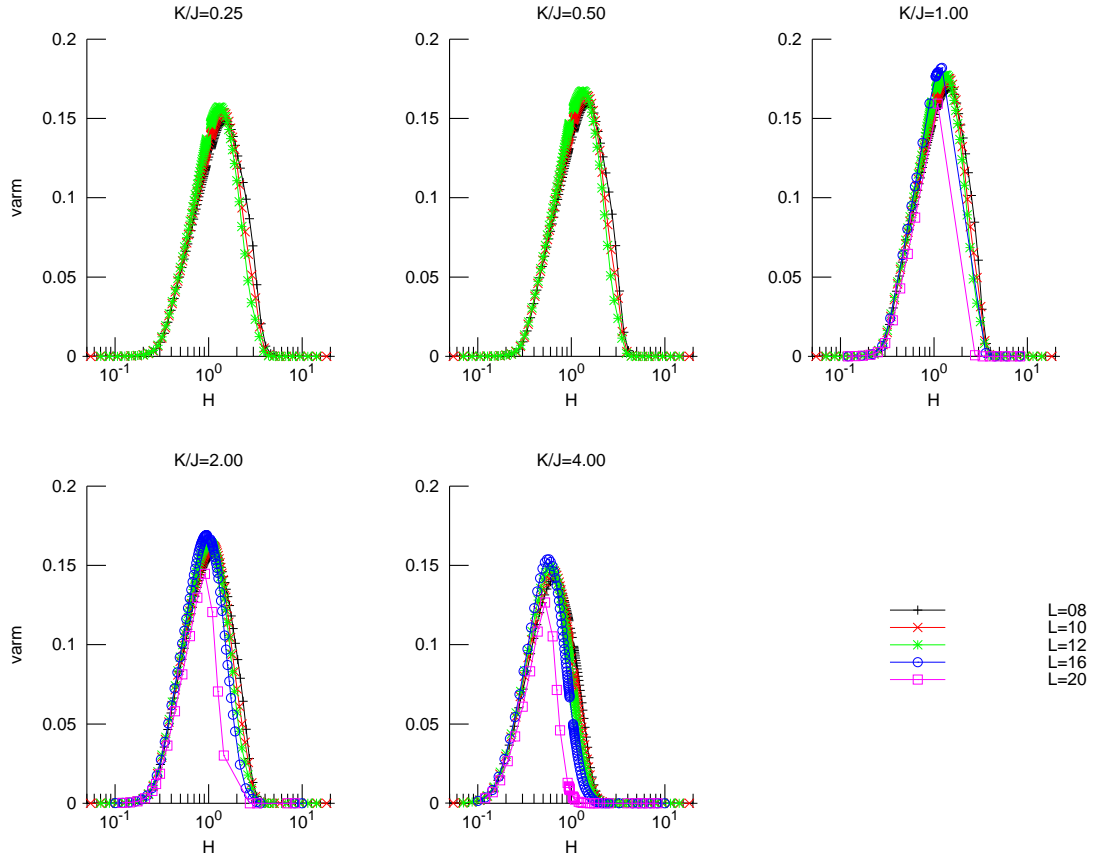


Figure 24: Variance of disorder fluctuations of magnetization. The different graphs corresponds to different values of  $\epsilon$  and the different curves to different lattice sizes  $L$

Both variances are numerically very stable for all the lattice sizes. They vanish at high and low transverse fields  $h$  and display a well-defined single peak. The peak is located at the same control param-

eter  $\delta$  as the second peak of the autocorrelation functions (Fig. 21, 22). The difference with the previous results is the absence of the first peak at  $h \sim J_2$ . The same conclusion can be drawn: the magnetic and electric transitions occur at very close control parameters  $\delta$ , probably the same, for  $\epsilon \leq 1$ , while a finite shift is observed for  $\epsilon > 1$ . Unfortunately, due to the small lattice sizes that were studied, a weak dependence on  $L$  is observed in both figures of the variances. For the case of  $\epsilon \leq 1$ , as the lattice size is increased the distance between the two critical lines decreases confirming the prediction of a single phase transition in this region.

We have to note that the variance at the lattice size  $L = 20$  displays a smaller peak than smaller lattice sizes. This is probably due to the fact that for  $L = 20$  the average has not been computed over all possible disorder configurations but only over a subset ( $\sim 10\%$ ) of them. To avoid any potential under-sampling, we will consider safer to discard them.

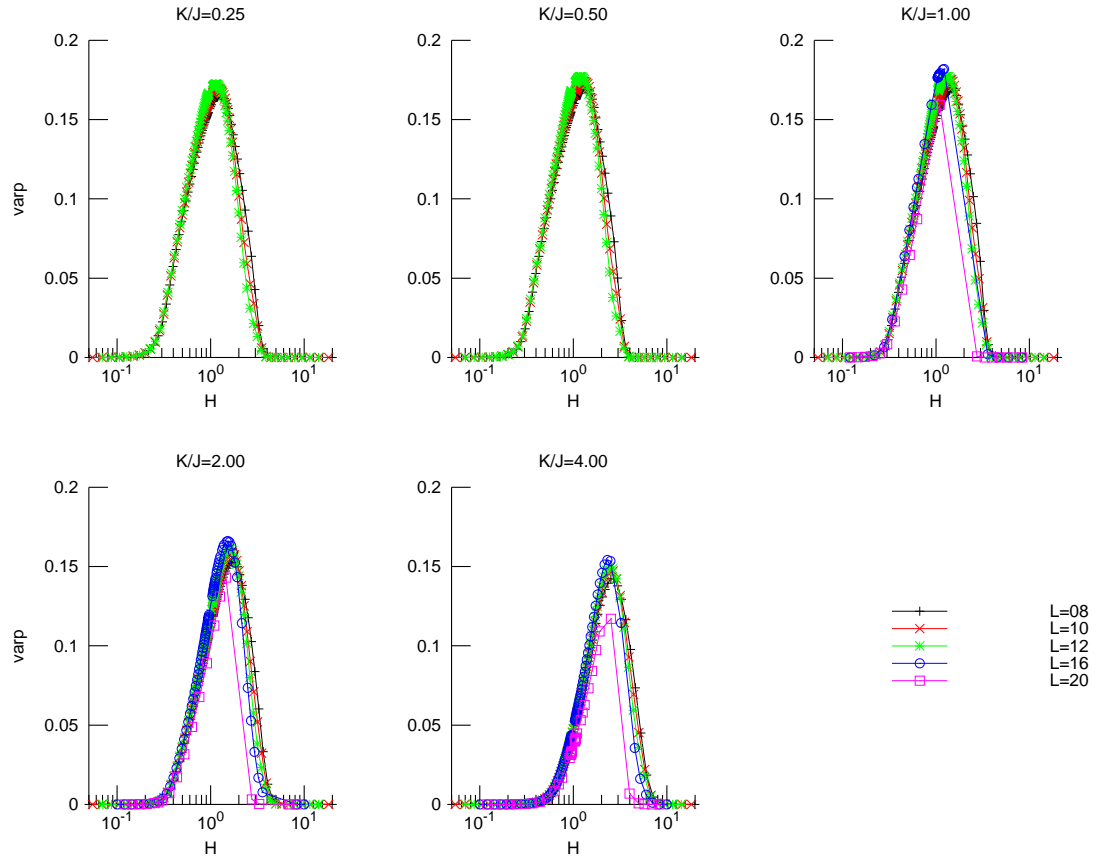


Figure 25: Variance of disorder fluctuations of polarization. The different graphs corresponds to different values of  $\epsilon$  and the different curves to different lattice sizes  $L$

## 4.3.2.5 Autocorrelation functions

The average connected spin-spin and polarization-polarization autocorrelation functions  $\overline{A(t)}$  of the random quantum AT chain are presented on Fig. 26 and Fig. 27 respectively. As discussed before, both quantities present a different behavior in the different regions of the phase diagram. At the critical point, the autocorrelation function scales logarithmically with time [46],

$$\overline{A(t)} \sim (\ln t)^{-2x_m}, \quad 2x_m = 2\beta/\nu = 1 - \frac{1 + \sqrt{5}}{4}. \quad (136)$$

In the Griffiths phases, the autocorrelation functions are affected by the rare regions and they present an algebraic decay [47]

$$\overline{A(t)} \sim t^{-1/z}, \quad (137)$$

with the dynamical exponent  $z$ . Finally, in the other regions a purely exponential decay is observed

$$\overline{A(t)} \sim e^{-t/\xi_t}. \quad (138)$$

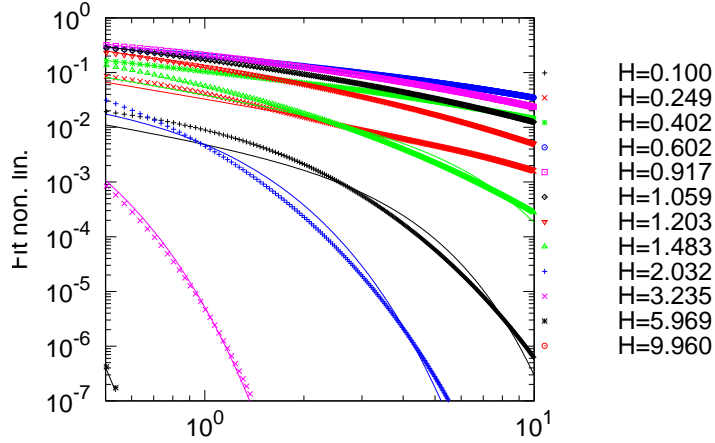


Figure 26: Spin-spin autocorrelation function of the random Ashkin-Teller chain versus time  $t$ . The different graphs correspond to different values of the transverse field  $h$ . The continuous lines correspond to a fit, either with ansatz (140) or with an exponential (141).

In the case of the random quantum Ising chain, the algebraic decay of autocorrelation functions in the Griffiths phase was numerically shown by exploiting the mapping onto a gas of free fermions [48]. Due to the small lattice sizes that we were able to reach by DMRG numerical calculations, the algebraic decay is not present for the spin-

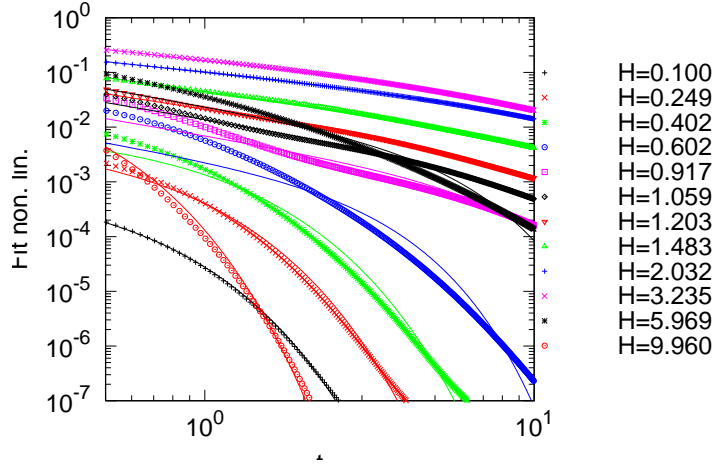


Figure 27: Polarization-polarization autocorrelation function of the random Ashkin-Teller chain versus time  $t$ . The different graphs correspond to different values of the transverse field  $h$ . The continuous lines correspond to a fit, either with ansatz (140) or with an exponential (141).

spin and polarization-polarization autocorrelation functions of the random quantum AT chain. An algebraic decay is expected to hold in these kind of systems only for large time  $t \gg 1$  and in the thermodynamic limit  $L \gg 1$ . The intermediate regime between small and large time  $t$  was checked by plotting the effective exponent  $\frac{d \ln \overline{A(t)}}{d \ln t}$  with  $t$ . Still, no algebraic decay was observed in the region expected inside of the double-Griffiths phase. The numerical data is fitted by an extended expression of the one proposed by Rieger *et al.* for autocorrelation function in the Griffiths phase of the quantum Ising model [47]. Consider in the paramagnetic phase a rare region of linear size  $\ell$ . The region has a probability to be ordered which scales with the size, as  $\wp \sim e^{-c\ell}$ , with  $c$  is a small number compared to the  $\ell$ . The spins inside the rare region have a relaxation or tunneling time given by  $\tau(\ell) \sim e^{\sigma'\ell}$  with  $\sigma'$  a surface tension. In a finite system of width  $L$ , the linear size of rare regions is bounded by  $L$  so the average autocorrelation function reads

$$\begin{aligned} \overline{A(t)} &= \int_0^L \wp(\ell) e^{-t/\tau(\ell)} d\ell = \frac{t^{-c/\sigma'}}{\sigma'} \int_{te^{-\sigma'L}}^t u^{c/\sigma'-1} e^{-u} du \\ &= \frac{t^{-1/z}}{\sigma'} [\gamma(1/z, t) - \gamma(1/z, te^{-\sigma'L})] \end{aligned} \quad (139)$$

where  $u = te^{-\sigma'\ell}$ ,  $\sigma'/c = z$  is the dynamical exponent, and  $\gamma(a, x)$  is the incomplete gamma function. In the limit of large time  $t$  and lattice size  $L$ , one recovers the prediction  $\overline{A(t)} = \frac{\Gamma(1/z)}{\sigma'} t^{-1/z}$  obtained in the saddle-point approximation. The numerical estimate of the

connected autocorrelation functions were fitted with the 4-parameter non-linear *ansatz*

$$\overline{A(t)} = a_1 t^{-a_2} |\gamma(a_2, a_3 t) - \gamma(a_2, a_4 t)|, \quad (140)$$

where  $a_1 = 1/\sigma'$ ,  $a_2 = 1/z$ ,  $a_3 = 1$  and  $a_4 = e^{-\sigma' L}$ . The bounds  $0 < a_2 \leq 1$  were imposed during the fitting procedure. The quality of the fit was quantified by the mean-square deviation  $\chi^2$ . In figures 26 and 27 the data were also fitted with an exponential decay

$$\overline{A(t)} = a_1 e^{-a_2 t} \quad (141)$$

On the figures, the continuous lines correspond to the best fit, either (140) or (141).

The data is reproduced by an exponential decay for large transverse fields for spin-spin autocorrelation function but for small transverse field in the case of polarization-polarization, confirming the phase diagrams of Fig. 17 and 23. On the other hand, for intermediate transverse fields, the data is reproduced by *ansatz* (140) which confirms that our data are located into the Griffiths phase. For  $\epsilon \leq 1$  the two phases are centered around  $h = 1$  with boundaries similar for both autocorrelation functions. For  $\epsilon = 4$ , the Griffiths phases are shifted to smaller values of the transverse field for spin-spin autocorrelation functions and to larger ones for polarization-polarization autocorrelation functions, as was expected from the phase diagrams 23 and 17. For  $\epsilon = 2$ , the shift is only seen for the polarization-polarization autocorrelation functions. At the boundaries of the Griffiths phase the data is not well fitted, neither by the *ansatz* nor by the exponential form for both the autocorrelation functions. In the other side, for some values of the transverse field, the fit deviates from the numerical data, which probably corresponds to a cross-over region where the autocorrelation functions behave in a more complex way.

The parameters  $a_2$  of Eq. (140) which corresponds to the inverse of dynamical exponent  $z$  is extracted and plotted with the transverse field  $h$  for spin-spin (Fig. 28) and polarization-polarization autocorrelation functions (Fig. 29). In agreement with figure 18, the dynamical exponent for the spin-spin autocorrelation function displays a peak which is associated to the magnetic transition and correspondingly the polarization-polarization autocorrelation a peak which is associated to an electric transition. Both transitions are located at the critical point. As we saw in the case of the autocorrelation times (Fig. 21, 22) and disorder fluctuations (Fig. 24, 25), the electric and magnetic transitions take place at the same control parameter for  $\epsilon \leq 1$  but for different ones when  $\epsilon > 1$ . This phenomenon is also present for the dynamical exponent for the two autocorrelation functions (Fig. 28 and 29) as well as the maxima of all the peaked quantities, found to be at the same location. The region between the two phase transi-

tions and with a dynamical exponent  $z$  larger than one is the double Griffiths phase (in agreement with 17 and 23). In our case, the double-Griffiths phase is not infinite because of the construction of the binary distribution of the couplings  $J_i$  and  $K_i$ .

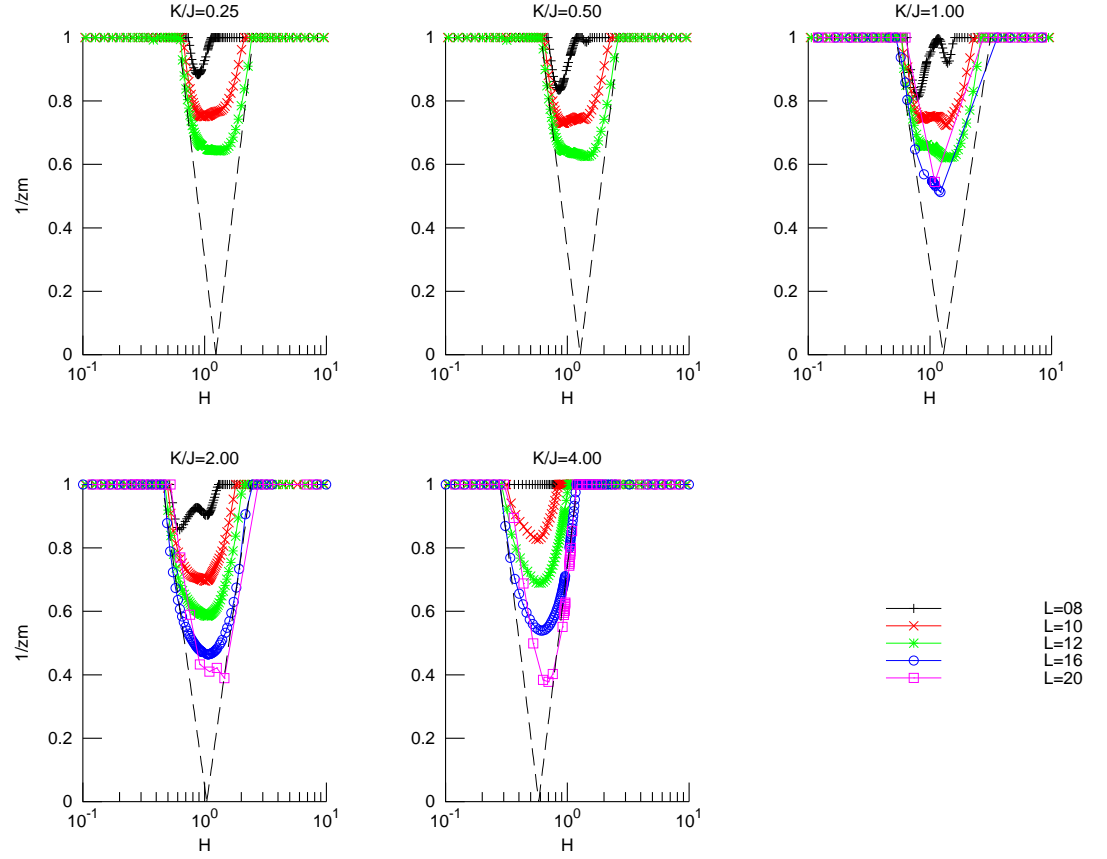


Figure 28: Inverse of the dynamical exponent  $z$  estimated from the spin-spin autocorrelation function, versus the transverse field  $h$ . The different curves correspond to different lattice sizes and the different graphs to different values of  $\epsilon$ .

For the RTFIM the dynamical exponent away from the critical point [19], [27] scales with the distance from criticality as

$$z \sim \frac{1}{2|\delta|}. \quad (142)$$

In order to study this behavior in the case of the random quantum AT chain, we define the boundaries  $\delta_+ = -\ln h_+$  and  $\delta_- = -\ln h_-$  of the first and the last point with  $z > 1$  that are inside the Griffiths phase.

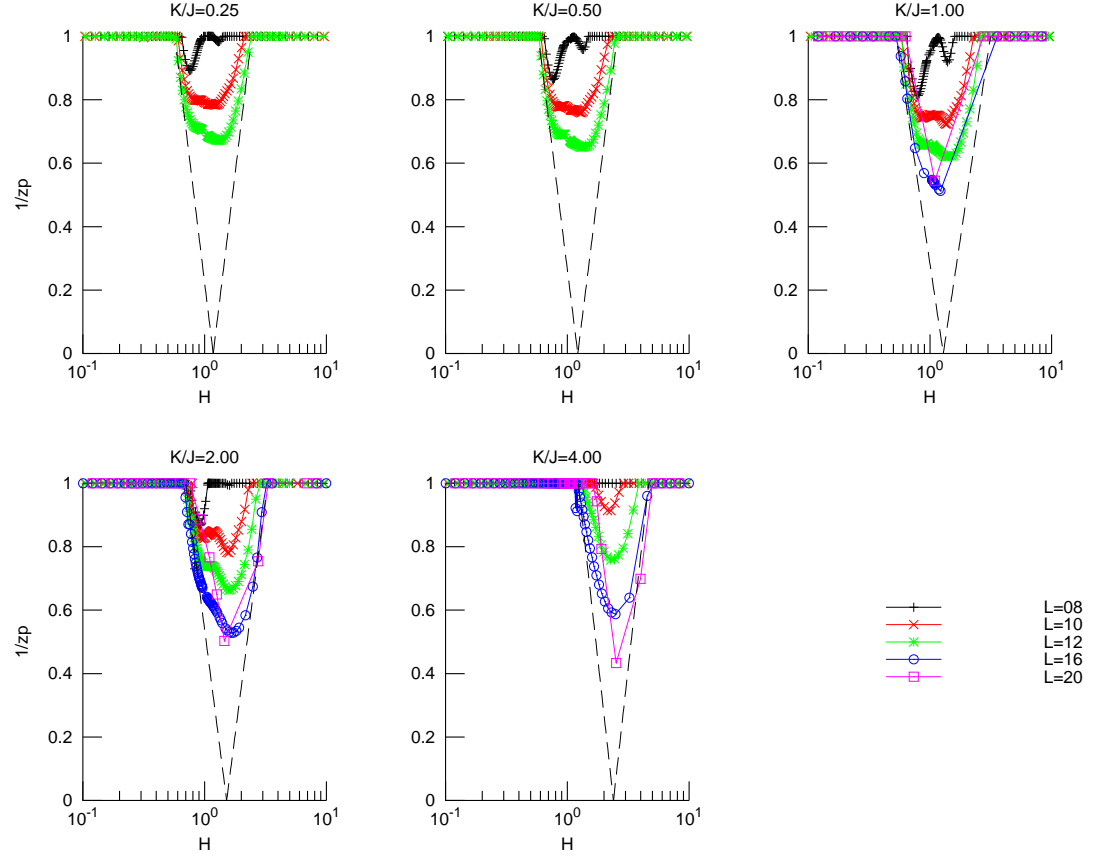


Figure 29: Inverse of the dynamical exponent  $z$  estimated from the polarization-polarization autocorrelation function, versus the transverse field  $h$ . The different curves correspond to different lattice sizes and the different graphs to different values of  $\epsilon$ .

Then, the critical point is defined from the two boundary parameters as

$$\delta_c = \frac{\delta_- + \delta_+}{2}. \quad (143)$$

On the figures 28 and 29, the two dashed lines correspond to the straight lines:

$$\frac{1}{z(\delta)} = \begin{cases} \frac{\delta - \delta_c}{\delta_+ - \delta_c}, & \text{for } \delta \in [\delta_c; \delta_+] \\ \frac{\delta - \delta_c}{\delta_- - \delta_c}, & \text{for } \delta \in [\delta_-; \delta_c] \end{cases}. \quad (144)$$

The slope of the two lines is not equal to two as in the RTFIM (142) but is in the range of  $1 - 1.5$ . We see that, as the lattice size increases, the numerical data tend to accumulate to the straight lines of Eq. (144).

### 4.3.3 Conclusion

In this part of the thesis, we presented our contribution to the study of quantum random spin chains. We briefly discussed the general critical properties and critical exponents of the one-dimensional random quantum Ising chain, the paradigmatic example in the field of quantum phase transitions. Subsequently, we discussed the SDRG approach that was applied to the quantum random Ising model and quantum random Potts model, extracting in both cases evidences of the existence of an IDFP. We confirmed by preliminary numerical calculations the values of three basic critical exponents which were found to be very close to the exact values.

In the second part of the chapter, the study of the random quantum Ashkin-Teller chain by DMRG was presented. The critical properties were analyzed using the integrated autocorrelation times obtained from the spin-spin and polarization-polarization autocorrelation functions as well as the variance of disorder fluctuations of magnetization and polarization. Both quantities present peaks at the locations of the phase transition. The phase diagram of the model is obtained by the first moment of both autocorrelation functions and is found to be in agreement with the phase diagram obtained by SDRG by Hrahsheh *et al.* [41]. Finally, a double-Griffiths phase is found to be located at  $\epsilon > 1$ . The two dynamical exponents  $1/z_m$  and  $1/z_p$  were extracted from the algebraic decay of the two autocorrelation functions in the Griffiths phase. Both present a peak but at a different location.

---

## QUANTUM PHASE TRANSITIONS IN APERIODIC SYSTEMS

---

### 5.1 INTRODUCTION

The study of aperiodic systems in condensed matter physics and statistical mechanics started to develop after the discovery of *quasi-crystals* [49]. A *quasi-crystal* or *quasi-periodic crystal* corresponds to a crystallographic structure that is ordered but not periodic. Even though they are characterized by a violation of translational symmetry, quasi-crystals fill all the available space and their diffraction pattern shows sharp peaks. They were experimentally discovered in 1982, when an unusual quasi-periodic form was observed in alloys of aluminium-manganese. From the side of mathematics, the field of aperiodic tiling with a set of tiles copied to form a non periodic structure, was discovered in the early 1960s with the famous example of the Penrose tiling [50]. It is only twenty years after its discovery in mathematics that aperiodic tiling was applied to physics and, more specifically, to the study of quasi-crystals.

In theoretical physics, the early research on quasi-crystals includes the work of Henley [51] and Janssen [52] who described a tiling method generating a quasi-crystal and reproducing the two and three dimensional diffraction patterns of experimentally observed quasi-crystals. Guyot *et al.* [53] and Janot *et al.* [54] extensively studied quasi-crystalline materials and their diffraction properties.

In the field of critical phenomena, the first model on which the influence of a quasi-periodic perturbation was studied is the Ising model. The real-space Renormalization Group (RG) introduced by Migdal-Kadanoff [55] was used by Godr che *et al.* [56] to study the phase transition of the 2D ferromagnetic Ising model on a Penrose lattice. During the renormalization, four nonequivalent effective exchange couplings are considered. One year later, Ayoma *et al.* [57] studied the same model, as well as the percolation model, but with eight types of renormalized bond interactions. They proved that the aperiodic model belongs to the same universality class as the periodic one. This work was extended to three-dimensional ferromagnetic sys-

tems by Bose [58]. In the same way, Tracy [59] introduced aperiodicity only in the vertical bonds of the 2D Ising model. The Hamiltonian is

$$H = -J_1 \sum_j \sum_k \sigma_{j,k} \sigma_{j,k+1} - \sum_j \sum_k J_2(j) \sigma_{j,k} \sigma_{j+1,k}, \quad \sigma_{i,j} = \pm 1 \quad (145)$$

where  $J_2(j)$  follows the Fibonacci sequence while  $J_1$  is uniform on the lattice. Tracy proved that the specific heat displays a logarithmic singularity but suggested that aperiodic modulation could lead to different universality classes.

In parallel with RG methods, free-fermion techniques [60] were also applied to the aperiodic Ising chain. Indeed, in the extreme anisotropic limit  $J_1(i) \rightarrow \infty$  and  $J_2(i) \rightarrow 0$ , the 2D model defined by the classical Hamiltonian (145) is equivalent to the quantum Ising chain in a transverse field of Hamiltonian

$$H = -\frac{1}{2} \sum_{i=1}^{\infty} [\sigma_i^x + \lambda_i \sigma_i^z \sigma_{i+1}^z] \quad (146)$$

where  $\lambda_i = J_2(i)/J_1^*(i)$  is the ratio of horizontal bonds with the dual of vertical ones. Luck et al. [61] considered an aperiodic modulation of the exchange couplings of the quantum XY spin chain with a uniform transverse magnetic field. They obtained exact results for the zero-temperature magnetization, the zero-field specific heat as well as for the magnetic susceptibility. They observed that aperiodic systems display a behavior that may be described as intermediate between those of random and homogeneous systems. The 1D quantum Ising chain was first studied by Ceccatto [62] who calculated the energy gap and the singularities of the ground-state energy of the model at its critical point. Iglói [63] considered both aperiodic exchange couplings and transverse fields of the quantum Ising chain. By exactly solving the model, he proved that the finite-size behavior was in agreement with Conformal Field Theory (CFT) predictions.

An important breakthrough in this field was accomplished by Luck [64], who extended the Harris criterion [13], originally introduced for disordered system, to aperiodic models. The argument is known as Luck criterion or Harris-Luck criterion. By calculating the exponent describing the growth of geometrical fluctuations in an aperiodic sequence, the wandering exponent  $\omega$ , and comparing with the correlation length exponent  $\nu$  of the pure model, the criterion allows to predict whether aperiodic modulation is an irrelevant, marginal or relevant perturbation at the fixed point of the pure model. The argument was initially formulated for the 1D quantum Ising model using the free-fermion approach but was later extended to higher dimensions [65].

A lot of attention was later given to the semi-infinite layered 2D Ising model with the exchange interactions  $J_1(i)$  parallel to the surface and  $J_2(i)$  perpendicular. After a mapping onto a free-fermion

model, Peschel [66] had shown that the surface magnetization is given by the simple formula

$$m_s = \left( 1 + \sum_{j=1}^{\infty} \prod_{i=1}^j \lambda_i \right)^{-1/2}. \quad (147)$$

Using this expression, Turban *et al.* [67,68] studied the quantum Ising model (146) at its critical point for three different kinds of aperiodic modulation. For an irrelevant modulation the surface magnetization  $m_s$  vanishes with a square root singularity, like the homogeneous model, and the surface exponent is found to be  $\beta_s = 1/2$ . For a marginal modulation, the surface magnetization has a weaker singularity and the exponent  $\beta_s$  is a continuous function of the modulation amplitude. For the Period-Doubling sequence, they found

$$\beta_s = \frac{\ln[(1 + \lambda_s)(1 + \lambda_s^{-1})]}{4 \ln 2},$$

where  $\lambda_s$  is the critical coupling. For a relevant aperiodic modulation, the surface magnetization  $m_s$  either vanishes with an essential singularity or remains finite.

Iglói *et al.* [69] studied the critical behavior in the case of a relevant aperiodic modulation, the Rubin-Shapiro sequence. They managed to obtain the exact form of the surface magnetization, showing an essential singularity. In Ref. [70], by a detailed comparison between random and aperiodic systems at critical point, they found that in both systems the length scales anisotropically with time as

$$L \sim (\ln t)^{1/\omega}. \quad (148)$$

where  $\omega$  is the wandering exponent. The dynamical exponent is therefore formally infinite, as in the random Ising chain in a transverse field. In the same work, they calculated the critical exponents of autocorrelation functions and magnetization of the Rubin-Shapiro sequence. In addition, they proved that there is no Griffiths region in aperiodic systems. In Ref. [71], they showed that different relevant aperiodic modulations lead to different universality classes and that the energy gap at the critical point scales with the length as

$$\Delta E \sim \exp(-\text{const} L^\omega). \quad (149)$$

Using the exact expression of the surface magnetization (147), Karevski *et al.* [72] calculated exactly the magnetic surface exponent for the Freedholm sequence and the surface energy density exponent by finite-size scaling. In Ref. [73], they studied the log-periodic oscillations that are characteristic of aperiodic systems at the critical point. For

the marginal Fredholm sequence, the exact expression of the log-periodic amplitude is given by

$$A_s = \frac{r^{-2} - 1}{\ln m} \Gamma\left(\frac{\ln r^{-2} - 2\pi s}{\ln m}\right). \quad (150)$$

where  $r$  is the ratio of the couplings forming the aperiodic sequence and  $m$  the characteristic coefficient of the Fredholm sequence. The study of surface magnetization was extended to marginal and relevant sequences. B. Berche *et al.* [74] proved that a system with marginal perturbation is scale invariant but not conformal invariant. The scaling dimension of the surface energy  $x_{es}$  is related to the dynamical exponent  $z$  and to the surface magnetization exponent  $\beta_s$  by

$$x_{es} = z + 2\beta_s.$$

This result was confirmed by P.E. Berche *et al.* [75] in the case of other marginal sequences.

Using an exact RG approach [76], Iglói *et al.* [77] confirmed many results previously obtained, as the surface magnetization exponent, the dynamical exponent, . . . . This exact RG approach was extended by Hermisson *et al.* to derive and confirm the Harris-Luck criterion [78] and to get exact results for the surface magnetization of the quantum Ising chain [79]. It was later applied to study the aperiodic XY model [80].

Further critical properties of aperiodic systems were studied by numerical methods. In the early years, Monte Carlo (MC) approaches were applied to the 2D classical ferromagnetic Ising model on a Penrose lattice. Okabe *et al.* [81] combined MC simulations and finite-size scaling to calculate the critical temperature, confirming the prediction of self-duality, and the magnetization critical exponent. Sørensen *et al.* [82], computed the critical temperature, the exponents  $\eta$  and  $\nu$  for the same model but with three different geometries (rational, spherical and toroidal). The critical exponents were found to be the same for all geometries. Finally, the Penrose lattice was shown to lead to the same universality class as the homogeneous Ising model. Langie *et al.* [83] computed the critical exponent  $\nu$  for different types of random walk models on the Penrose lattice and observed that it is the same as the 2D periodic lattice.

Some years later, attention was given to the critical behavior of the aperiodic 2D Potts model. P.E. Berche *et al.* [84] studied the eight-state model with aperiodic exchange couplings. Using MC techniques, it was shown that the strong first-order phase transition of the pure model is smoothed by aperiodic fluctuations and that the transition becomes continuous. The same authors [85] later extended the results to more aperiodic sequences, calculating the exponents  $\beta/\nu$ ,  $\gamma/\nu$  as well as surface properties.

The critical behavior of aperiodic quantum Ising model on Bethe lattice was studied numerically by M.S. Faria *et al.* [86]. They calculated the exact critical temperature and the critical exponents  $\beta$ ,  $\gamma$  and  $\delta$ . Iglói *et al.* [87] studied analytically the surface critical behavior as well as the relevance criterion for the model.

Strong-Disorder Renormalization Group (SDRG) was first applied to aperiodic chains by Hida [88] to study the critical behavior of a Fibonacci modulation of the couplings of the XXZ model. The same model was then considered by A.P. Vieira [89,90] who applied SDRG numerically. The approach was extended to the Heisenberg and XX models. A few years later, F.J. Oliveira Filho *et al.* [91] determined the critical behavior of the quantum Ising model in a transverse field for a family of aperiodic couplings, as well as for the Rubin-Shapiro sequence. The results were confirmed by a comparison with free-fermion techniques. Entanglement Entropy (EE) was also determined for aperiodic spin chains. Iglói *et al.* [92] considered the Heisenberg, XX and Ising models and showed that for marginal and relevant aperiodic modulations, EE is a logarithmic function of the block size with logarithmic periodic oscillations. Juhasz *et al.* [93] studied the EE in the XXZ chain. Finally, Barghathi *et al.* [94] combined SDRG approach and MC numerical techniques to study the non-equilibrium phase transition of the contact process model with aperiodic modulation.

A very challenging issue that we want to answer in this chapter is the critical behavior of the aperiodic quantum Potts chain. Performing analytical and numerical SDRG, we aim at answering the questions: is the critical point controlled by an IDFP? Do the critical exponents or the dynamical exponent  $z$  depend on the number of Potts state  $q$  and on the coupling ratio?

This chapter is divided as follows: In 5.2, we construct the aperiodic sequences and study their properties, we then discuss the Harris-Luck criterion and give a list of the most considered aperiodic sequences. In 5.3, we present the known results of the SDRG approach on the quantum Ising chain in transverse magnetic field with a modulation of the exchange coupling in the cases of relevant, marginal and relevant aperiodic modulations. We study by numerical SDRG the scaling of average magnetization as well as the largest energy with the lattice size during the renormalization, extracting the dynamical exponent  $z$ . In 5.4, we finally extend the SDRG approach to the quantum  $q$ -state Potts chain.

## 5.2 APERIODIC SEQUENCES

### 5.2.1 Substitution Matrix

The aperiodic sequences are generated by iterating substitution rules on letters  $A, B, \dots$  such that  $A \rightarrow S(A)$  and  $B \rightarrow S(B) \dots$ . The proper-

ties of any sequence is controlled by a substitution matrix, which is defined as

$$\mathbb{M} = \begin{pmatrix} n_A^{S(A)} & n_A^{S(B)} & \cdots \\ n_B^{S(A)} & n_B^{S(B)} & \cdots \\ \vdots & \vdots & \ddots \end{pmatrix}, \tag{151}$$

where for example the matrix element  $n_A^{S(A)}$  gives the number of letter  $A$  in the pattern  $S(A)$ . A simple example of aperiodic system is the *Thue-Morse* sequence which is given by the substitution rules (for simplicity we denote here the letters  $A$  as 0 and  $B$  as 1)

$$S(0) \rightarrow 01 \quad S(1) \rightarrow 10.$$

The sequence after the  $n$  first iterations of the substitution rules are

$$\begin{aligned} n = 0 & \quad 0, \\ n = 1 & \quad 01, \\ n = 2 & \quad 0110, \\ n = 3 & \quad 01101001, \\ n = 4 & \quad 0110100110010110, \\ & \quad \dots \end{aligned}$$

The substitution matrix of the Thue-Morse sequence is

$$\mathbb{M}_{\text{thue-morse}} = \begin{pmatrix} 1 & 1 \\ 1 & 1 \end{pmatrix}.$$

If we define a vector  $U_0$ , whose two components are the numbers of letters  $A$  and  $B$  in the initial sequence ( $U_0 = (1, 0)$  in the above example of the Thue-Morse sequence), then the components of  $U_n = \mathbb{M}^n U_0$  are the number of letters  $A$  and  $B$  after  $n$  iterations of the substitution rules. For  $n$  large, the dominant contribution to  $U_n$  is due to the largest eigenvalue  $\zeta_1$  of  $\mathbb{M}$ . The length of the sequence grows as

$$L_n \sim \zeta_1^n. \tag{152}$$

The asymptotic density of letters  $A$  in the sequence can be shown to be

$$\rho_\infty^A = \frac{V(1)}{\sum_i V(i)} \tag{153}$$

where  $V$  is the eigenvector associated to  $\zeta_1$ . For a finite chain, the deviation from this asymptotic density grows with the second largest eigenvalue

$$\rho_n^A - \rho_\infty^A \sim \left( \frac{\zeta_2}{\zeta_1} \right)^n \tag{154}$$

and therefore

$$\rho_n^A - \rho_\infty^A \sim L^{\omega-1} \tag{155}$$

where

$$\omega \equiv \frac{\ln |\zeta_2|}{\ln \zeta_1} \quad (156)$$

is the so-called *wandering exponent* [101] of the aperiodic sequence.

### 5.2.2 Irrelevant/Relevant Criterion

In the following, we consider one-dimensional quantum spin models, for example the Ising model in a transverse field, with exchange couplings between nearest spins either equal to  $J_A$  or  $J_B$  according to an aperiodic sequence. Introduce the notations

$$J_A = \bar{J} + \rho_\infty^B \delta, \quad J_B = \bar{J} - \rho_\infty^A \delta, \quad (157)$$

where  $\delta = J_A - J_B$  and  $\bar{J}$  is the average coupling. The fluctuations around the average coupling are

$$\Delta J = \frac{1}{L_n} \sum_{k=1}^{L_n} (J_k - \bar{J}) \sim \delta L_n^{\omega-1}, \quad (158)$$

where  $\omega$  is the wandering exponent of the sequence.

In chapter 4, we showed that the Harris criterion [13] allows to determine whether a random perturbation is relevant or not. When the specific heat exponent  $\alpha$  of the pure system is positive, randomness is a relevant perturbation. This argument has an extension to aperiodic systems [65, 95], where under some circumstances the aperiodic modulation might be an irrelevant, marginal or relevant perturbation at the pure fixed point. It is then called *Harris-Luck* or *Luck* criterion. The deviation  $t$  from the critical point is compared to the spatially averaged temperature shift  $\overline{\delta t} \sim \overline{\delta J(\zeta)}$ , which is produced by the geometric fluctuations at a length scale  $\zeta$ . Since the correlation length grows as  $\zeta \sim t^{-\nu}$  [64] in the neighborhood of the critical point, one has

$$\frac{\overline{\delta t}}{t} \sim t^{-\phi}, \quad \phi = 1 + \nu(\omega - 1). \quad (159)$$

When the exponent  $\phi$  is negative, the ratio vanishes at the critical point. The aperiodicity is then an irrelevant perturbation. In the other side, when  $\phi$  is positive, the ratio diverges and the aperiodic modulation is a relevant perturbation. Finally, when  $\phi = 0$ , the aperiodic modulation is marginal and may lead the system to a non universal critical behavior. The same results are recovered from the calculation of the scaling dimension of the modulation amplitude  $\delta$ , which is equal to  $\phi/\nu$  [96].

From the Harris-Luck criterion, we easily see that the wandering exponent  $\omega$  controls whether the geometric fluctuations will be a relevant, marginal or irrelevant perturbation. Of course, the argument has different consequences for each model, Ising or Potts for example,

since the correlation length exponent  $\nu$  varies from one model to the other.

### 5.2.3 Aperiodic Sequences

We are now presenting the most considered aperiodic sequences and we give a short description of their basic properties. More aperiodic sequences can be found in the reference [97].

#### 5.2.3.1 The Thue-Morse Sequence

We have already presented the Thue-Morse sequence at the paragraph 5.2.1. The sequence has a wandering exponent  $\omega = -\infty$  and from the Harris-Luck criterion, we conclude that in any model that we are interested in, the aperiodic modulation will lead to an irrelevant perturbation. The critical behavior is therefore the same as in the pure model.

#### 5.2.3.2 The Fibonacci Sequence

The Fibonacci sequence is the most studied aperiodic sequence in statistical mechanics and condensed matter physics. It is defined by the substitution rules  $A \rightarrow S(A) = AB$ ,  $B \rightarrow S(B) = A$ . The evolution of the sequence with the identification,  $A = 0$  and  $B = 1$ , is

$$\begin{aligned} n = 0 & \quad 0, \\ n = 1 & \quad 01, \\ n = 2 & \quad 010, \\ n = 3 & \quad 01001, \\ n = 4 & \quad 01001010, \\ & \quad \dots \end{aligned}$$

and the substitution matrix is then

$$\mathbb{M}_{\text{fibonacci}} = \begin{pmatrix} 1 & 1 \\ 1 & 0 \end{pmatrix}.$$

The eigenvalues of the matrix are  $\zeta_1 = 1.618$  and  $\zeta_2 = -0.618$ , and the wandering exponent of the sequence is  $\omega = -1$ . Therefore, a modulation of the couplings of the Ising or Potts models with the Fibonacci sequence is expected to be irrelevant.

5.2.3.3 *The Period-Doubling Sequence*

The Period-Doubling sequence [98] is generated by the substitution rules  $A \rightarrow S(A) = AB$ ,  $B \rightarrow S(B) = AA$ . The iteration of the sequence can be sketched as

$$\begin{aligned} n = 0 & \quad 0, \\ n = 1 & \quad 01, \\ n = 2 & \quad 0100, \\ n = 3 & \quad 01000101, \\ n = 4 & \quad 0100010101000101, \\ & \quad \dots \end{aligned}$$

and the substitution matrix is then

$$\mathbb{M}_{\text{period-doubling}} = \begin{pmatrix} 1 & 1 \\ 2 & 0 \end{pmatrix}.$$

The eigenvalues are  $\zeta_1 = 2$ ,  $\zeta_2 = -1$  and the wandering exponent is  $\omega = 0$ . Interestingly, the modulation of the couplings with the Period-Doubling sequence is a marginal perturbation for the Ising model and is relevant for the 3 and 4-state Potts models.

5.2.3.4 *The Paper-Folding Sequence*

The Paper-Folding sequence [99] is defined in a more complex way. The origin of the sequence comes from the recurrent folding of a sheet of paper onto itself, right over left. The substitution rules are defined by,  $A \rightarrow S(A) = AC$ ,  $B \rightarrow S(B) = DB$ ,  $C \rightarrow S(C) = DC$ , and  $D \rightarrow S(D) = AB$ . For simplicity we are doing the identification  $A = 00$ ,  $B = 11$ ,  $C = 10$  and  $D = 01$ , then the substitution rules are

$$\begin{aligned} 00 \rightarrow S(00) = 1000, \quad 01 \rightarrow S(01) = 1001, \\ 10 \rightarrow S(10) = 1100 \quad 11 \rightarrow S(11) = 1101. \end{aligned}$$

Starting from the two values 00, the first iterations of the substitution rules lead to

$$\begin{aligned} n = 0 & \quad 00, \\ n = 1 & \quad 1000, \\ n = 2 & \quad 11001000, \\ n = 3 & \quad 1101100011001000, \\ & \quad \dots \end{aligned}$$

with the substitution matrix

$$\mathbb{M}_{\text{paper-folding}} = \begin{pmatrix} 1 & 0 & 1 & 0 \\ 0 & 1 & 0 & 1 \\ 0 & 0 & 1 & 1 \\ 1 & 1 & 0 & 0 \end{pmatrix}.$$

The largest eigenvalues are  $\zeta_1 = 2$ ,  $\zeta_2 = 1$  and the wandering exponent is  $\omega = 0$ , like the Period-Doubling sequence. The same conclusions are therefore drawn: the perturbation is marginal for the Ising model and relevant for the 3 and 4-state Potts models.

5.2.3.5 *The Three-Folding Sequence*

The Three-Folding sequence [100] is defined by the subsection rules  $A \rightarrow S(A) = ABA$   $B \rightarrow S(B) = ABB$ . The sequence has the property to triple at each iteration. The first iterations of the rules lead to

$$\begin{aligned} n = 0 & & 0, \\ n = 1 & & 010, \\ n = 2 & & 010011010, \\ n = 3 & 010011010010011011010011010, \\ & & \dots \end{aligned}$$

and the substitution matrix is

$$\mathbb{M}_{\text{three-folding}} = \begin{pmatrix} 2 & 1 \\ 1 & 2 \end{pmatrix}.$$

The eigenvalues are  $\zeta_1 = 3$ ,  $\zeta_2 = 1$  and the wandering exponent is  $\omega = 0$ , like the Period-Doubling and Paper-Folding sequences.

5.2.3.6 *The Rubin-Shapiro Sequence*

A more complex example of aperiodic sequence is the 4-letter Rubin-Shapiro (RS) sequence [101] where now the substitution rules apply on four letters,  $A, B, C$  and  $D$ :

$$\begin{aligned} A \rightarrow S(A) &= AB, & B \rightarrow S(B) &= AC, \\ C \rightarrow S(C) &= DB, & D \rightarrow S(D) &= DC. \end{aligned}$$

The evolution of the sequence is

$$\begin{aligned}
 n = 0 & \quad A, \\
 n = 1 & \quad AB, \\
 n = 2 & \quad ABAC, \\
 n = 3 & \quad ABACABDB, \\
 n = 4 & \quad ABACABDBABACDCAC, \\
 & \quad \dots\dots\dots
 \end{aligned}$$

and the substitution matrix

$$\mathbb{M}_{\text{rubin-shapiro}} = \begin{pmatrix} 1 & 1 & 0 & 0 \\ 1 & 0 & 1 & 0 \\ 0 & 1 & 0 & 1 \\ 0 & 0 & 1 & 1 \end{pmatrix}.$$

with the eigenvalues  $0, \pm\sqrt{2}, 2$  and the wandering exponent  $\omega = 1/2$ . This sequence is a relevant perturbation for the Ising and 3-state and 4-state Potts model.

Sequence	$\omega$	$\phi_{IM}$	$\phi_p (q \geq 3)$	IM	Potts
Thue-Morse	$-\infty$	$< 0$	$< 0$	Irr.	Irr.
Fibonacci	-1	$< 0$	$< 0$	Irr.	Irr.
Paper-Folding	0	0	$> 0$	Marg.	Rel.
Period-Doubling	0	0	$> 0$	Marg.	Rel.
Three-Folding	0	0	$> 0$	Marg.	Rel.
Rubin-Shapiro	1/2	$> 0$	$> 0$	Rel.	Rel.

Table 6: Wandering exponent  $\omega$  of each sequence and cross-over exponent  $\phi$  at the Ising and Potts critical points. The last two columns correspond to the Harris-Luck criterion prediction for the Ising and Potts model. Irr. means irrelevant, Marg. marginal and Rel. relevant.

### 5.3 THE APERIODIC QUANTUM ISING MODEL

#### 5.3.1 Application to a family of aperiodic sequences

In this paragraph we summarize the results of F. J. Oliveira Filho *et al* [91] for the aperiodic quantum Ising chain in a transverse field. We consider the family of aperiodic sequences generated by the substitution rules:

$$a \rightarrow ab^k, \quad b \rightarrow a \quad \text{for} \quad b^k \equiv \underbrace{bb \dots b}_{k \times \text{letters}} \quad (160)$$

where  $k$  is a positive integer. For  $k = 1$  the *Fibonacci* sequence is recovered. In the case  $k = 2$  for example, the substitution rules are

$$a \rightarrow abb, \quad b \rightarrow a \quad (161)$$

and the first iterations of the substitution rules lead to

$$\begin{aligned} n = 0 & \quad a, \\ n = 1 & \quad abb, \\ n = 2 & \quad abbaa, \\ n = 3 & \quad abbaaabbabb, \\ & \quad \dots \end{aligned} \quad (162)$$

In the case of a general  $k$ , we obtain the substitution matrix

$$\mathbb{M}_k = \begin{pmatrix} 1 & 1 \\ k & 0 \end{pmatrix}, \quad (163)$$

whose eigenvalues are

$$\zeta_k^\pm = \frac{1}{2} \pm \frac{1}{2} \sqrt{1 + 4k}, \quad (164)$$

so that the wandering exponent is

$$\omega_k = \frac{\ln |\zeta_k^-|}{\ln \zeta_k^+} = \frac{\ln k}{\ln \zeta_k^+} - 1, \quad (165)$$

Computing the wandering exponents for each integer values of  $k$ , we see that, according to the Harris-Luck criterion for the Ising model, the aperiodicity is an irrelevant perturbation for  $k = 1$ . For  $k = 2$ , the aperiodic modulation is marginal and for  $k \geq 3$  it is relevant.

#### 5.3.1.1 RG rules

The Strong Disorder Renormalisation Group, introduced to study random quantum spin chains, is applied here to the case of an aperiodic modulation of the couplings. The only difference with the random model is that clusters of  $k$  identical couplings are present in the lattice. These clusters should be renormalized into a single effective coupling as a whole.

Consider two nearest-neighbor couplings  $J_a$  and  $J_b$ , following the above aperiodic sequence (160). The transverse magnetic field  $h$  is assumed to be uniform across the lattice and we consider the inequality  $J_a < h < J_b$ . The largest coupling, which will be decimated, is denoted as  $\Omega \in \{J_b, h, J_a\}$ . Assuming that the coupling  $J_b$  is larger than  $h$  and  $J_a$ ,  $\Omega$  is the interaction coupling  $J_b$ , which is present only as clusters of  $k$  couplings (Figure 30). These clusters contain  $k + 1$  spins, each of them interacting with a transverse field  $h$ . The cou-

plings at the left and right edges of the cluster, are denoted  $J_l$  and  $J_r$  respectively. After renormalization, the relative state of the  $k + 1$  spins is frozen, i.e. their quantum state is a superposition of the two ferromagnetic states of the cluster. The latter is therefore equivalent to a single spin  $1/2$ , interacting with the rest of the chain via the couplings  $J_l$  and  $J_r$ . In addition, this effective spin is subject to a renormalized transverse field:

$$h^{(j+1)} = \frac{[h^{(j)}]^{k+1}}{[J_b^{(j)}]^k} \quad (166)$$

at the  $j$ -th iteration of the renormalization group. The new effective field, has replaced all the couplings  $J_b$ , as depicted on Fig. 30. The couplings  $h^{(j)}$  and  $J_b^{(j)}$  represent the values of the parameters after  $j$  iterations of the RG method.

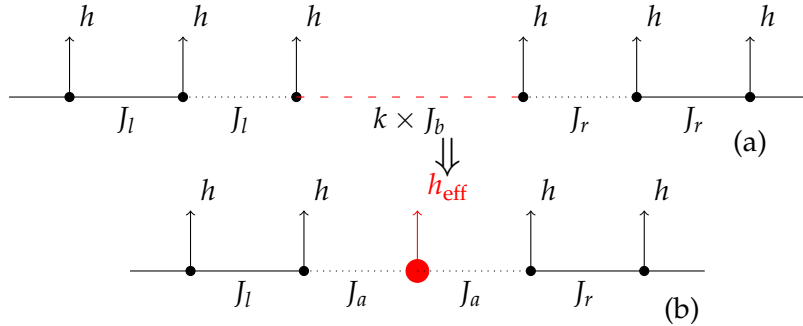


Figure 30: Renormalization of a cluster of strong bond  $J_b$ . (a) Lattice before renormalization, where the red cluster will be decimated out. (b) Lattice with the new effective field.

After the decimation of all couplings  $J_b$ , the next largest energy is the transverse field  $h$ , which we assume to be larger than the coupling  $J_a \ll h$ . Now, the field  $h$  appears in the chain as clusters of  $k$  spins which are coupled to the same field (Figure 31). These spins are coupled via a nearest-neighbor spin coupling  $J_a$ . After renormalization, these  $k$  spins are frozen in the quantum state  $|\uparrow\uparrow \dots\rangle_x$  and do not interact anymore with the rest of the system. Therefore, the cluster can be decimated out. Applying again perturbation theory, an effective coupling  $J_{\text{eff}}$  between the two spins at respectively the left and the right of the frozen spins is introduced (Fig. 31):

$$J_a^{(j+1)} = \frac{[J_a^{(j)}]^{k+1}}{[h^{(j)}]^k}. \quad (167)$$

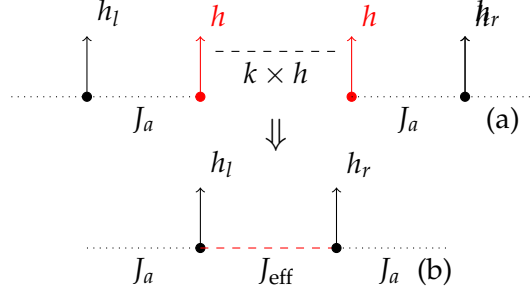


Figure 31: Renormalization of a cluster of strong fields  $h$ . (a) Lattice before the renormalization, with a cluster of spins coupled to the same transverse field  $h$  and interacting via a next-neighbor interaction  $J_a$ . (b) The lattice after renormalization with the new effective interaction coupling at the location of the cluster.

After the renormalization of  $J_b$  and  $h$ ,  $J_a$  is now the largest coupling in the system. The original aperiodic sequence is recovered when  $J_b$  is replaced by

$$J_b^{(j+1)} = J_a^{(j)}. \quad (168)$$

The couplings  $J_a^{(j+1)}$  and  $h^{(j+1)}$  have been defined above. After this substitution, the renormalization is the same as the one at iteration  $j$ .

### 5.3.1.2 Eigenvalues and critical field

Defining the ratios

$$r^{(j)} = \frac{h^{(j)}}{J_b^{(j)}}, \quad s^{(j)} = \frac{J_a^{(j)}}{h^{(j)}}, \quad (169)$$

the SDRG rules, Eq. (166), (167) and (168) can be written in a matrix form as

$$\begin{pmatrix} \ln r^{(j+1)} \\ \ln s^{(j+1)} \end{pmatrix} = \begin{pmatrix} k & -1 \\ -k & k+1 \end{pmatrix} \begin{pmatrix} \ln r^{(j)} \\ \ln s^{(j)} \end{pmatrix}. \quad (170)$$

Equation (170) can be expressed in terms of the eigenvalues of the substitution matrix. Indeed, define

$$|u_j\rangle = \begin{pmatrix} \ln r^{(j)} \\ \ln s^{(j)} \end{pmatrix} \quad \text{and} \quad \mathbb{T}_k = \begin{pmatrix} k & -1 \\ -k & k+1 \end{pmatrix}. \quad (171)$$

and

$$\mathbb{T}_k |v_k\rangle = \lambda_k |v_k\rangle, \quad (172)$$

where  $\lambda_k$  and  $\nu_k$  are the eigenvalues and the eigenvectors of the matrix  $\mathbb{T}_k$ . The set of eigenvectors  $\nu_k$  forms the matrix  $\mathbb{V}_k$  of change of basis. If no eigenvalue of  $\mathbb{T}_k$  vanishes, this change of basis is invertible, i.e.

$$\mathbb{T}_k = \mathbb{V}_k \mathbb{D}_k \mathbb{V}_k^{-1} \quad (173)$$

where in the last expression,  $e_i$  is the natural basis vector and the diagonal matrix  $\mathbb{D}_k$  contains the eigenvalues  $\lambda_k^\pm$ . Diagonalizing the matrix  $\mathbb{T}_k$ , we observe that its eigenvalues are related to the eigenvalues Eq. (164) of the substitution matrix by the relation

$$\lambda_k^\pm = k + \zeta_k^\pm = (\zeta_k^\pm)^2 \quad (174)$$

so that the matrices  $\mathbb{V}_k$  and  $\mathbb{V}_k^{-1}$  can be written as

$$\mathbb{V}_k = \begin{pmatrix} 1 & 1 \\ -\zeta_k^+ & -\zeta_k^- \end{pmatrix} \quad \text{and} \quad \mathbb{V}_k^{-1} = \frac{1}{\zeta_k^+ - \zeta_k^-} \begin{pmatrix} -\zeta_k^- & \zeta_k^+ \\ -1 & 1 \end{pmatrix}. \quad (175)$$

Constructing the expression (173) using (175) and substituting into Eq. (170), we get

$$\ln r^{(j)} = \frac{1}{\zeta_k^+ - \zeta_k^-} [ -(\lambda_k^+)^j a_k^- + (\lambda_k^-)^j a_k^+ ] \quad (176)$$

and

$$\ln s^{(j)} = \frac{1}{\zeta_k^+ - \zeta_k^-} [ (\lambda_k^+)^j \zeta_k^+ a_k^- + (\lambda_k^-)^j \zeta_k^- a_k^+ ] \quad (177)$$

with

$$a_k^\pm = \zeta_k^\pm \ln r^{(0)} + \ln s^{(0)}. \quad (178)$$

The SDRG rules, in the matrix form Eq. (170), is transformed into the expressions (176) and (177). The two ratios  $r^{(j)}$  and  $s^{(j)}$  depends on the eigenvalues  $\lambda_k^\pm$  and the initial values of the couplings. The first term of the right part of the equations (176) and (177) is the most important in the SDRG analysis. For large  $j$ , the behavior of the two ratios under renormalization is dominated by the largest eigenvalue  $\lambda_k^+$  of the matrix  $\mathbb{T}_k$ . This eigenvalue controls the location of the critical point. When  $a_k^-$  is positive, then  $\ln r^{(j)} < 0$  and  $\ln s^{(j)} > 0$  which, by Eq. (169), means that the effective coupling is much larger than the effective field so that the system is in the ferromagnetic phase. Conversely, if  $a_k^-$  is negative then  $\ln r^{(j)} > 0$  and  $\ln s^{(j)} < 0$ . The effective fields are then much larger than the effective couplings and the systems is in the paramagnetic phase. If  $a_k^- = 0$ , the logarithms in equation (176) and (177) vanish, which means by Eq. (169) that the transverse field is equal to the interaction couplings. This case

corresponds to the *critical point*. Solving Eq. (178), the critical field is given by

$$h_{\text{crit}} = J_a^{\frac{1}{1-\zeta_k}} J_b^{\frac{-\zeta_k}{1-\zeta_k}} = J_a^{d_a} J_b^{d_b}, \quad (179)$$

where  $d_a$  and  $d_b = 1 - d_a$  are the fractions of letters  $a$  and  $b$  in the infinite aperiodic sequence after the evolution of the substitution rules.

The above result calculated using the SDRG completely agrees with the condition of criticality of a general quantum Ising chain in a transverse field derived by Pfeuty [?]. Note that the expression for the *critical field* preserves the duality exploited in the SDRG rules.

### 5.3.1.3 Renormalization of lengths and magnetic moments

During the renormalization of the couplings, there is also a renormalization of the magnetic moments. On Fig. 30, each spin in the cluster of  $k$  couplings  $J_b$  carries a magnetic moment corresponding to his contribution to the total magnetization. During the renormalization of the  $k$  couplings, the  $k + 1$  spins will be replaced by a single macro-spin carrying the magnetic moment:

$$\tilde{\mu}^{(j+1)} = (k + 1)\mu^{(j)}. \quad (180)$$

During the renormalization of a cluster of  $k$  identical transverse fields, the  $k$  spins will be frozen in a state with zero magnetic moment. An effective coupling is introduced between the spins at the left and the right of this cluster. However, these two spins were not nearest-neighbors in the original lattice but separated by a distance that will be defined in the following as the length of the bond associated to the new effective coupling. During the renormalization of the cluster of  $k$  identical transverse fields, the new length will be the sum of the lengths of the  $k + 1$  bonds joining the  $k$  spins. Similarly, for the different situations discussed above the renormalization of the lengths of the bonds can be written as

$$\begin{pmatrix} \ell_a^{(j+1)} \\ \ell_b^{(j+1)} \\ \ell_h^{(j+1)} \end{pmatrix} = \begin{pmatrix} k+1 & 0 & k \\ 1 & 0 & 0 \\ 0 & k & k+1 \end{pmatrix} \begin{pmatrix} \ell_a^{(j)} \\ \ell_b^{(j)} \\ \ell_h^{(j)} \end{pmatrix}, \quad (181)$$

where  $\ell_a$  and  $\ell_b$  are the lengths of the couplings  $J_a$  and  $J_b$  respectively.  $\ell_h$  denotes the size of a single site. It will increase during the renormalization of the couplings when several spins will be merged into a single one. All these effective lengths grows asymptotically with the largest eigenvalue of the substitution matrix  $S_k$  Eq. (181) as

$$\ell_a^{(j)} \sim \ell_b^{(j)} \sim \ell_h^{(j)} \sim (\lambda_k^+)^j \quad (182)$$

## 5.3.1.4 Analysis at the critical point

At the critical point ( $a_k^- = 0$ ) the recursion relations become

$$\ln r^{(j)} = \frac{a_k^+}{\zeta_k^+ - \zeta_k^-} (\lambda_k^-)^j \quad \text{and} \quad \ln s^{(j)} = \frac{\zeta_k^- a_k^+}{\zeta_k^+ - \zeta_k^-} (\lambda_k^-)^j. \quad (183)$$

The second largest eigenvalue  $\lambda_k^-$  will control the critical behavior of the ratios  $\ln r^{(j)}$  and  $\ln s^{(j)}$ . In the case of the family of aperiodic sequences (160), the eigenvalue  $\lambda_k^-$  depends on  $k$ . SDRG predicts therefore a different critical behavior according to the value of  $k$ , like the Harris-Luck criterion. For  $k = 1$  the aperiodic modulation is an irrelevant perturbation (Fibonacci sequence). The eigenvalue which appears in Eq. (183) is  $\lambda_k^- \simeq 0.38$  and, by replacing the values of  $\zeta_{k=1}^\pm$ , we see that the two ratios asymptotically vanish. The SDRG method is therefore not applicable and we conclude that the critical behavior corresponds to the one of the pure model, with a dynamical behavior

$$\Omega \sim \ell^{-z}, \quad z = 1. \quad (184)$$

For  $k = 2$ , we find  $\lambda_k^- = 1$  and then, the ratios in Eq. (183) read

$$\ln r^{(j)} = \frac{a_k^+}{\zeta_k^+ - \zeta_k^-} \quad \text{and} \quad \ln s^{(j)} = \frac{\zeta_k^- a_k^+}{\zeta_k^+ - \zeta_k^-}. \quad (185)$$

Substituting the expression for  $a_k^+$  in terms of the initial values of  $J_a$ ,  $J_b$  and using the formula (179) for the field  $h$ , the ratios become

$$r^{(j)} = \left( \frac{J_a}{J_b} \right)^{d_a} \quad \text{and} \quad s^{(j)} = \left( \frac{J_a}{J_b} \right)^{1-d_a}, \quad (186)$$

in terms of the initial fractions  $d_a$  and  $d_b$  of the letters  $A$  and  $B$  in the sequence. The effective ratio between the couplings

$$\rho^{(j)} = \frac{J_a^{(j)}}{J_b^{(j)}} = \frac{J_a}{J_b} = \rho \quad (187)$$

remains constant during renormalization. The fixed point depends on the initial ratio of the two couplings. Equivalently, the phase diagram of the  $k = 2$  Fibonacci sequence displays a line of fixed points. This conclusion is compatible with the Harris-Luck criterion which states that the perturbation is marginal. In the SDRG analysis, the energy  $\Omega_j$  is equal to the strongest coupling at the  $j$ -th step:

$$\Omega_j \sim \rho^j J_b. \quad (188)$$

while its length Eq. (182) scales with the largest eigenvalue of the matrix (163) as

$$\ell_j \sim \ell_b \sim (\lambda_2^+)^j = 4^j. \quad (189)$$

Therefore, the dynamical scaling is in the marginal case

$$\Omega_j \sim \ell_j^{-z(\rho)}, \quad (190)$$

with the dynamical exponent

$$z(\rho) = -\frac{\ln \rho}{\ln 4}. \quad (191)$$

Finally, for  $k \geq 3$ , the eigenvalue  $\lambda_k^-$  is always larger than unity. The ratios  $r^{(j)}$  and  $s^{(j)}$  will indefinitely increase. As the SDRG method proceeds with the renormalization of the strong coupling and the energy  $\Omega$  is lowered, the SDRG rules in Eq. (169) become asymptotically exact, as in the random quantum Ising chain. This analysis is compatible with the prediction of the Harris-Luck criterion which states that the perturbation is relevant perturbation when the wandering exponent  $\omega$  is positive. The dynamical scaling is now [91]

$$\Omega_j \sim \exp[-(\ell_j/\ell_\rho)^\omega] \quad (192)$$

where  $\ell_\rho \sim |\ln \rho|^{-1/\omega}$  is a length scale depending on the original couplings. The wandering exponent  $\omega$  is the analogue of  $\psi$  in the random Ising chain.

### 5.3.2 Numerical results at the critical point

In this section, the SDRG approach, which was presented above for the family of Fibonacci sequences 5.3.1, is extended to other aperiodic sequences. We present numerical results for the sequences known as Thue-Morse (§ 5.2.3.1), the case  $k = 2$  of the Fibonacci family (§ 161), Paper-Folding (§ 5.2.3.4), Period-Doubling (§ 5.2.3.3), Three-Folding (§ 5.2.3.5) and Rubin-Shapiro (§ 5.2.3.6).

Strictly speaking, phase transitions and critical behavior only occur in the thermodynamic limit. We considered sequences as long as  $L = 2^{20} \simeq 10^6$ , i.e. 20 iterations of the substitution rules to minimize the finite-size effects. For the Three-Folding sequence (§ 5.2.3.5), only 14 iterations of the substitution rules were considered because the length of the sequence triples at each iteration.

The aperiodic modulation is only applied to the couplings between neighboring spins. Following the aperiodic sequence, they take the two values  $J_a$  and  $J_b$  and their ratio is denoted  $\rho = J_b/J_a$ . The transverse field  $h$  is uniform over the whole lattice and is chosen to satisfy the self-duality condition (179). We consider the case where  $J_b$  is initially the largest coupling of the lattice, i.e.  $J_a < h < J_b$ .

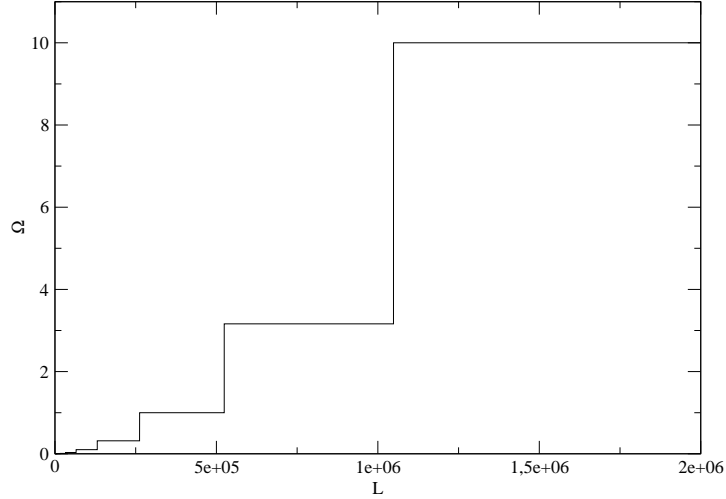


Figure 32: Maximum energy  $\Omega$  versus the lattice length  $L$  during the renormalization for the Paper-Folding sequence. The ratio of the couplings is  $\rho = J_b/J_a = 10$ .

In contrast to the random Ising chain, the renormalization of the aperiodic chain does not lead to a monotonously decaying energy  $\Omega$  but to a set of steps. Indeed, half (in most of the above-mentioned sequences) of the exchange couplings of the lattice take initially the value  $J_b$ . Therefore, of the order of  $L/2$  iterations will consist in the renormalization of these couplings. During these iterations, the largest coupling is constant:  $\Omega = J_b$ . The new effective transverse fields generated during renormalization are not necessarily identical but only a small set of different values are observed in practise. Only when all  $J_b$  couplings will have disappeared, then the renormalization of another coupling will start. On figure 32, the second step corresponds to the renormalization of the transverse field  $h_c \simeq 3.16$ . The third step corresponds to the renormalization of the couplings  $J_a = 1$ . The other smaller steps are due to the renormalization of the effective couplings generated during the first steps.

#### 5.3.2.1 Estimation of the magnetic scaling dimension

In the case of the random quantum Ising chain in a transverse magnetic field (RTFIM), the critical behavior is governed by an infinite-randomness fixed point (IRFP) characterized by an infinite dynamical exponent  $z$ . Therefore, the energy cutoff  $\Omega$  scales as

$$\Omega_j \sim e^{-L^{-\psi}} \Leftrightarrow L \sim \left( \ln \frac{\Omega_I}{\Omega_j} \right)^{-1/\psi} \quad (193)$$

and the magnetization as

$$\mu^{(j)} \sim \left[ \ln \frac{\Omega_I}{\Omega_j} \right]^\phi, \quad (194)$$

with the exponent  $\phi = (\sqrt{5} + 1)/2$ . In both cases, the energy  $\Omega_I$  is a non universal constant. Combining equations (193) and (194), the magnetic scaling dimension  $x_m = \beta/\nu$  is recovered if the total magnetization scales with the lattice size as

$$\mu^{(j)} \sim L^{-\phi\psi}. \quad (195)$$

with  $\beta = \nu(1 - \phi\psi)$ . In aperiodic systems, the dynamical exponent  $z$  may be finite. It is known for example to be the case for the Paper-Folding sequence with the Ising chain [77] for which

$$z = \frac{\ln(\rho^{1/2} + \rho^{-1/2})}{\ln 2}. \quad (196)$$

By definition of the dynamical exponent, the equation (193) is replaced by

$$\Omega \sim L^z. \quad (197)$$

Since equation (195) defines the magnetic scaling dimension, the law (194) should be replaced by

$$\mu \sim \Omega^{(1-\beta/\nu)/z}. \quad (198)$$

Using Eq. (195), we numerically computed the critical exponent  $\beta/\nu$ . Even though this exponent is in principle easily computed numerically for the Ising chain using the mapping onto a free-fermion gas, it is in general not known for most of the aperiodic sequences. Only for the Period-Doubling sequence, F.J. Oliveira Filho *et al* [91] gave the estimate  $\beta/\nu \simeq 0.2075$ . For the Thue-Morse sequence (§ 5.2.3.1), we already know that aperiodicity is an irrelevant perturbation, which means that  $\beta/\nu$  is expected to take the value 1/8 of the pure model.

#### *Thue-Morse sequence*

On Fig. 33, the average magnetic moment is plotted versus the lattice size during renormalization for the irrelevant Thue-Morse sequence. We do not observe any algebraic regime from which the critical exponent  $\beta/\nu$  could be extracted. This is in agreement with the fact that the critical behavior is controlled by the pure fixed point for which the SDRG is not expected to be applicable.

#### *Paper-Folding sequence*

The case of the Paper-Folding sequence (§ 5.2.3.4), marginal at the pure fixed point, is presented on Fig. 34 for two ratios  $\rho$  of the two couplings  $J_b$  and  $J_a$ . The average magnetic moment increases as the renormalization proceeds. The procedure is stopped when most of

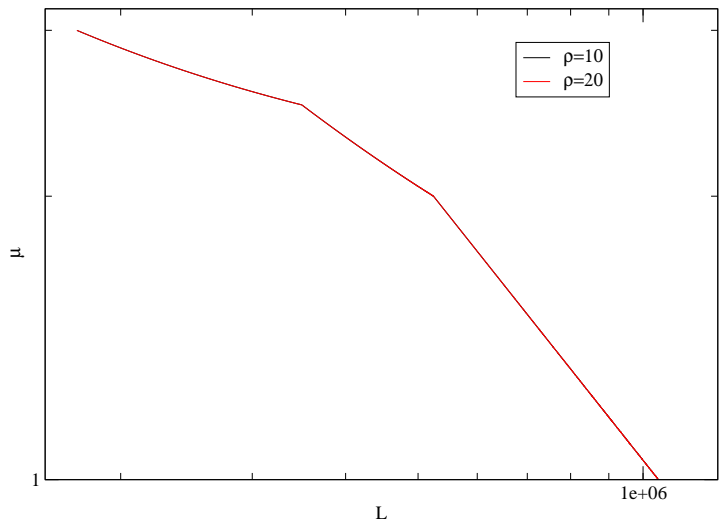


Figure 33: Average magnetization  $\mu$  versus the lattice size during the renormalization of the Ising chain with the Thue-Morse sequence.

the sites have been decimated out and only a single cluster remains with the same coupling or the same field. This cluster corresponds to the last step observed on the curve  $\Omega$  versus  $L$  presented on Fig. 32. The length of this last cluster of couplings, as seen on Fig. 34, is around  $N \simeq 100$ . Finally, we observe the presence of log-periodic oscillations of the average magnetization during the renormalization. Performing a simple log-log fit of the data, we estimate the critical exponent

$$\beta/\nu_{\text{Paper-Folding}} = 0.252(3). \tag{199}$$

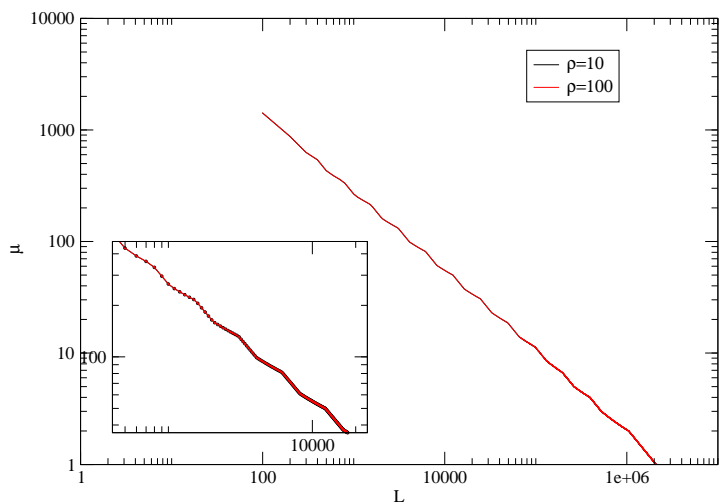


Figure 34: Average magnetic moment versus the lattice size during the renormalization of the Ising chain with the Paper-Folding sequence.

Two observations can be made from Fig. 34. First, the average magnetization is independent of the ratio  $\rho$ . We simulated two systems with  $\rho = 10$  and  $\rho = 100$ . The two curves cannot be distinguished on the figure. This is probably due to the SDRG method itself: the strongest couplings are indeed treated as infinitely stronger than any other coupling in the lattice so  $\rho = 10$  or  $\rho = 100$  does not change the renormalization. With other numerical methods, as free-fermion techniques [91] or Monte-Carlo simulations [85], a dependence on  $\rho$  is observed in many quantities (correlations functions, magnetic susceptibility, ...). Second, the error bar of the critical exponent (199) was estimated to be 0.003 (standard error on the slope given by a linear fit). The fit is stable whatever the region in which it is performed. The log-periodic oscillations do not seem to introduce any bias as long as an integer number of periods are taken into account in the fit.

#### *Period-Doubling sequence*

For the Period-Doubling sequence (§ 5.2.3.3), the average magnetic moment versus the lattice size is presented on Fig. 35. The data appear as divided into bunches of points. This can be understood by a simple analysis of the construction of the aperiodic sequence. As for the Paper-Folding sequence, the renormalization procedure stops when remains only one cluster whose size is  $N \sim 100$  sites. The critical exponent  $\beta/\nu$  is estimated to be

$$\beta/\nu_{\text{Period-Doubling}} = 0.254(6) \quad (200)$$

in very good agreement with the numerical result by F.J. Oliveira Filho *et al* [91]. Because the data is divided in groups of points with some distance between each of them (Fig. 35), the exponent  $\beta/\nu$  is not stable unless the fitting window contains an integer number of such groups and the same number of gaps between them. In each of these groups, a log-log fit gives the same exponent but a different estimate is obtained when considered all the points. The value of Eq. (200) is obtained by a log-log fit over all data points.

#### *Three-Folding sequence*

For the Three-Folding sequence (§ 5.2.3.5), the renormalization of the average magnetic moment is presented on Fig. 36 versus the lattice length. We performed only  $n = 13$  iterations because the sequence triples at each iteration of the substitution rules. Again the sequence is marginal for the quantum Ising model and it behaves as the two previous ones. The log-periodic oscillations are smaller due to the sequence construction. The critical exponent is estimated as

$$\beta/\nu_{\text{Three-Folding}} = 0.139(5) \quad (201)$$

The exponent in Eq. (201) was extracted by performing a fit in the central region. The numerical data was divided into three fitting windows, the difference of the exponent in each window is very

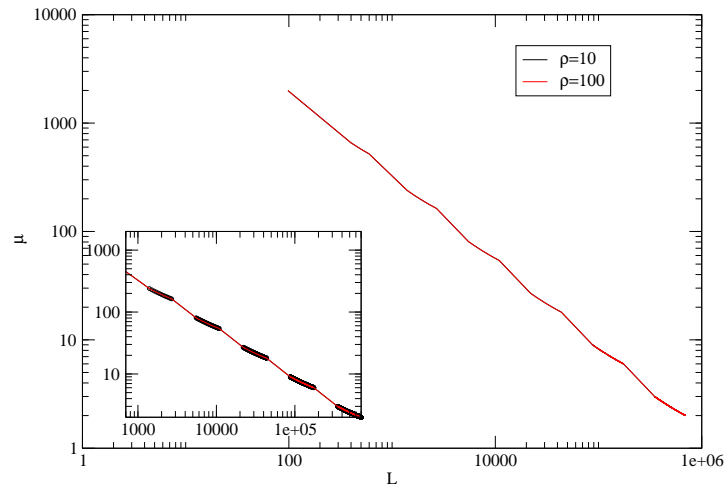


Figure 35: Average magnetization  $\mu$  versus the lattice size  $L$  during the renormalization of the Ising chain with the Period-Doubling sequence.

small. Unfortunately, there is no analytical nor numerical estimate of  $\beta/\nu$  in the literature for the Three-Folding sequence to compare with. The value that we obtain is closer to the pure Ising chain exponent than for the two other marginal sequences, Paper-Folding and Period-Doubling.

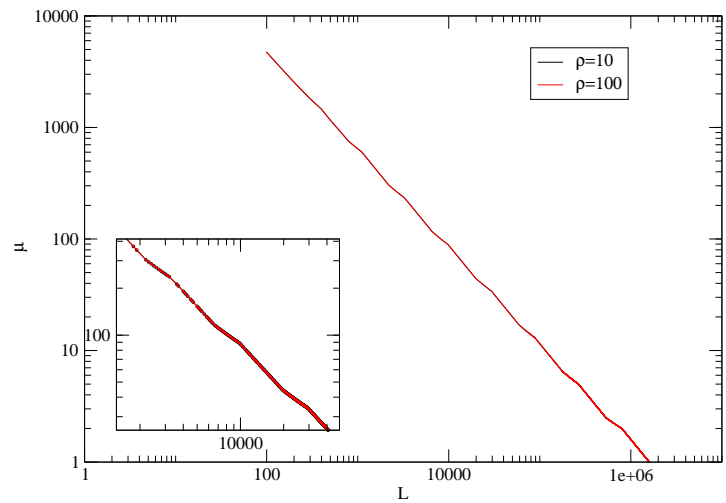


Figure 36: Average magnetization versus the lattice size during the renormalization of the Ising chain with the Three-Folding sequence.

In table 7, we summarize the estimated critical exponent  $\beta/\nu$  for the three marginal sequences that we considered, compared with the corresponding exponent for the pure and random quantum Ising chain. The exponents for the Paper-Folding and Period-Doubling sequences are compatible. This is surprising because the exact expressions for the dynamical exponent  $z$  as well as the surface magnetic

exponent  $x_{m_s}$  differ for both sequences [77]. Also, the exponent  $\beta/\nu$  is independent of the ratio  $\rho$  for all the marginal sequences, in contrast with the results for  $z$  and  $x_{m_s}$  [77].

Sequence	$\beta/\nu$
Pure Ising	0.125
Paper-Folding	0.252(3)
Period-Doubling	0.254(6)
Three-Folding	0.139(5)
Rubin-Shapiro	0.175(6)
Random Ising	0.192...

Table 7: Critical exponent  $\beta/\nu$  computed by SDRG method for the Ising chain with three marginal aperiodic sequences, and values of the pure and random quantum Ising chain.

#### *Rubin-Shapiro sequence*

We also studied the Ising chain with the Rubin-Shapiro sequence (§ 5.2.3.6), which is expected to be a relevant perturbation. The data are shown on Fig. 37. We found the magnetic critical exponent to be

$$\beta/\nu_{\text{Rubin-Shapiro}} = 0.175(6). \quad (202)$$

The exponent found is not compatible with the analytical prediction of F.J. Oliveira Filho *et al* [91] (0.1505). We have no explanation for this discrepancy.

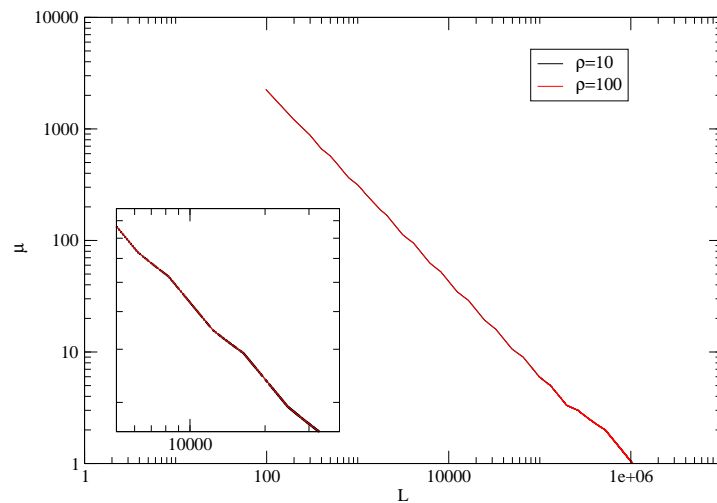


Figure 37: Average magnetization versus the lattice size during the renormalization of the Ising chain with the Rubin-Shapiro sequence.

### 5.3.2.2 Estimation of the dynamical exponent

As discussed in the previous chapter in the case of the random quantum Ising chain, the largest energy is expected to scale with the lattice length as

$$\Omega \sim L^z, \quad (203)$$

when the dynamical exponent  $z$  is finite. In this section, we confirm with SDRG numerical simulations the exact results obtained by F. Iglói *et al* [77] for the exponent  $z$  in the marginal case.

The behavior of  $\Omega$  versus  $L$  is schematically represented on Fig. 32. We have already discussed the fact that  $\Omega(L)$  is not monotonous but displays steps. Each one of these steps corresponds to the renormalization of the couplings with the same value. To fit the data and extract the exponent  $z$ , we considered each step and extracted the corner of the step. A log-log fit is performed only with the points corresponding to these corners. They are represented as red points on Fig. 38. The number of different renormalized couplings is quite small but, as we will see, the deviation from the exact results is nevertheless small.

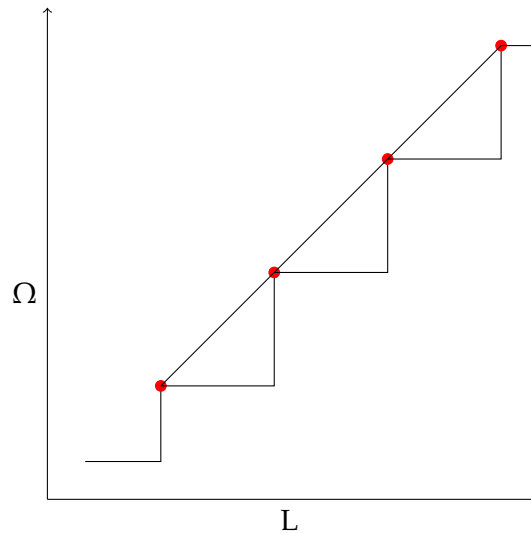


Figure 38: Sketch of the fit of the largest energy with the lattice length for an aperiodic sequence. The red points corresponds to the points that are considered in the fit. The line is the log-log fit.

#### *Fibonacci sequence*

First, we present the marginal case of the Fibonacci family of sequences (§ 5.3.1) when  $k = 2$ . On Fig. 39, we present the energy scaling versus the lattice length for the ratios  $\rho = 3$ ,  $\rho = 6$  and  $\rho = 10$ . The estimated dynamical exponents are given in table 8. They are

compared to the values computed from the formula (191), obtained analytically by SDRG by F.J. Oliveira Filho *et al* [91]. Even though the number of data points is small, the deviation of the numerical results with the analytical predictions is relatively small. What is surprising is the absence of log-periodic oscillations in contrast with what we observed for the scaling of the average magnetization.

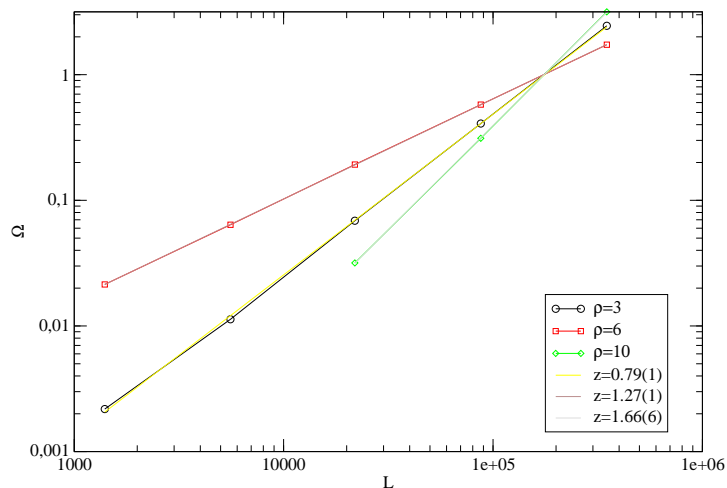


Figure 39: Largest energy  $\Omega$  versus the lattice length for three different values of the ratio  $\rho = 3, 6, 10$  in the case of the Fibonacci family of sequences (§ 5.3.1) when  $k = 2$ . Our estimates of the dynamical exponent  $z$  are shown in the legend.

Fibonacci $k = 2$	$z$ (SDRG theory)	$z$ (SDRG simul.)
$\rho = 3$	0.79248	0.79(1)
$\rho = 6$	1.2925	1.27(1)
$\rho = 10$	1.6610	1.66(6)

Table 8: Dynamical exponents  $z$  for three different ratios obtained by analytical and numerical SDRG approach for the marginal  $k = 2$  Fibonacci sequence.

#### *Paper-Folding sequence*

For the Paper-Folding sequence, the scaling of the largest energy  $\Omega$  with the lattice size is presented on Fig. 40. An exact expression for the dynamical exponent was obtained using free-fermion techniques [77] and is given by (196). In the limit of a large (or equivalently small) ratio  $\rho$ , this expression approaches the SDRG prediction Eq. (191). The results of the log-log fit converges to the same values as in table 8.

#### *Period-Doubling and Three-Folding sequences*

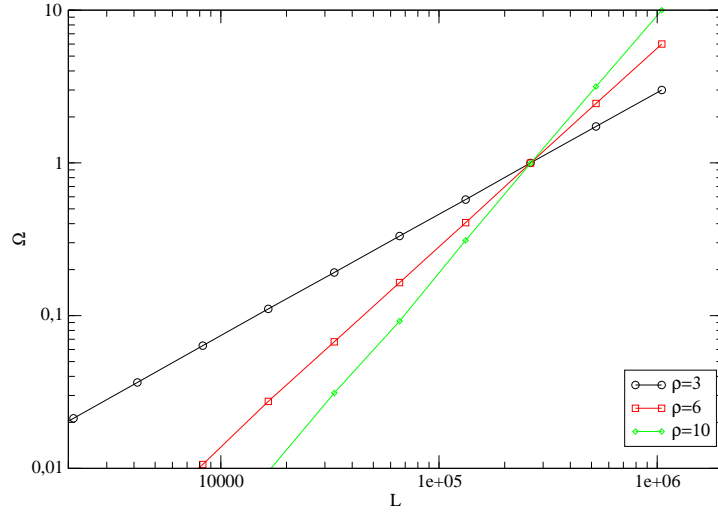


Figure 40: Energy scale versus the lattice length for three different values of the ratio  $\rho = 3, 6, 10$  with the corresponding non universal dynamical exponent  $z$  for the Paper-Folding sequence.

The energy scaling for the Period-Doubling sequence is presented in Fig. 41. The exact expression for the dynamical exponent as a function of the coupling ratio  $\rho$ , for this sequence obtained by Igloi *et al.* [77] is given by

$$z = \frac{\ln(\rho^{1/3} + \rho^{-1/3})}{\ln 2}. \quad (204)$$

Performing a log-log of each curve of different ratio  $\rho$  (Fig.41), we extract the dynamical exponents given in the table 9. As discussed before, for the SDRG approach, the dynamical exponent is compatible with the limit of Eq. (204) when taking a ratio  $\rho = J_b/J_{ba} \gg 1$ , i.e. with

$$z \simeq \frac{\ln \rho}{3 \ln 2}. \quad (205)$$

In table 9, we present the exponents for each case. The dynamical exponent obtained by numerical SDRG calculations are close to the values given by Eq. 205.

The scaling of energy for the Three-Folding sequence is presented on Fig. 42. The exact expression for the dynamical exponent obtained by Igloi *et al.* is given by

$$z = \frac{\ln[(2 + \rho)(2 + \rho^{-1})]}{2 \ln 3}. \quad (206)$$

Like in the previous sequences, the SDRG approach gives only access to the large-coupling limit of Eq. 206:

$$z \simeq \frac{\ln \rho}{2 \ln 3}. \quad (207)$$

coupling ratio	$z$ (exact)	$z$ (asyp.)	$z$ (SDRG)
$\rho = 3$	1.094	0.528	0.56(1)
$\rho = 6$	1.243	0.861	0.91(2)
$\rho = 10$	1.388	1.107	1.15(5)

Table 9: Dynamical exponents  $z$  for three different coupling ratios  $\rho$  in the case of the marginal Period-Doubling sequence. 'exact' denotes the exact value obtained analytically in [77]. 'asyp.' is the value given by Eq. 205 and 'SDRG' our numerical estimate.

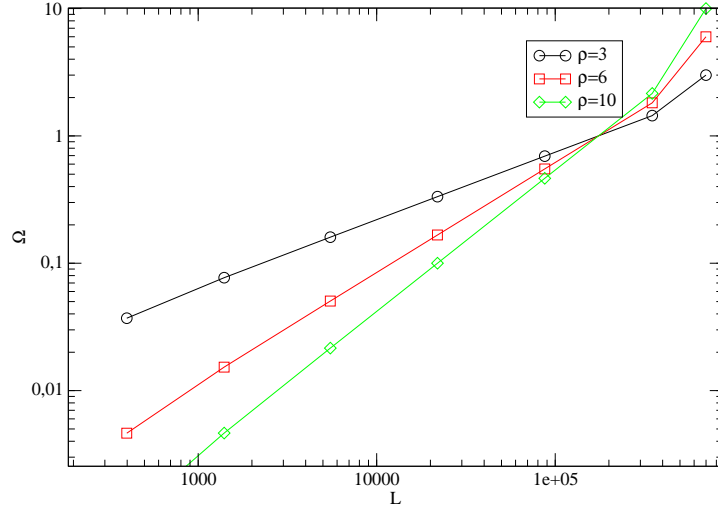


Figure 41: Energy scale versus the lattice length for three different values of the ratio  $\rho = 3, 6, 10$  for the Period-Doubling sequence.

The dynamical exponents obtained by the numerical SDRG calculations, as well as the exact values, are presented in table 10. As in the previous marginal sequences, the estimated exponents are close to Eq. (207).

coupling ratio	$z$ (exact)	$z$ (asyp.)	$z$ (SDRG)
$\rho = 3$	1.118	0.500	0.53(1)
$\rho = 6$	1.298	0.815	0.86(1)
$\rho = 10$	1.468	1.048	1.10(6)

Table 10: Dynamical exponents  $z$  for three different coupling ratios  $\rho$  in the case of the marginal Three-Folding sequence. 'exact' denotes the exact value obtained analytically in [77]. 'asyp.' is the value given by Eq. 205 and 'SDRG' our numerical estimate.

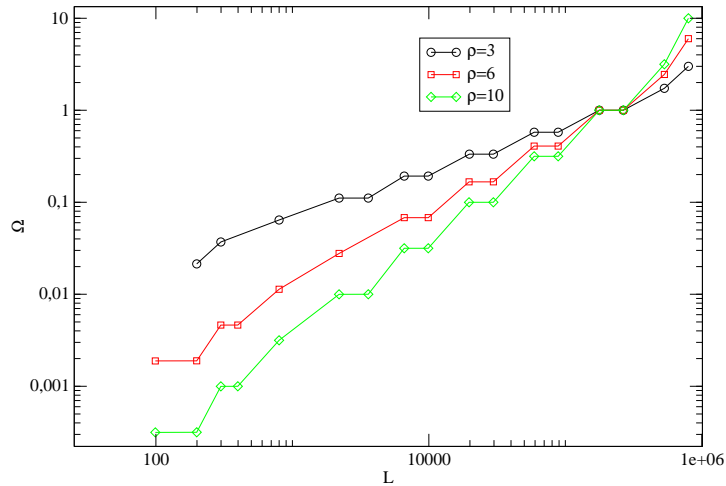


Figure 42: Energy scale versus the lattice length for three different values of the ratio  $\rho = 3, 6, 10$  for the Three-Folding sequence.

We observe that, for the marginal Fibonacci and Paper-Folding sequences, the largest energy  $\Omega$  scales algebraically with the lattice length over all the lengths. The estimated dynamical exponents are in good agreement with the analytical prediction. For the marginal Period-Doubling sequence, after the first two renormalization steps, the scaling becomes also algebraic. For the Three-Folding sequence, a lot of fluctuations are present. Nevertheless, the estimates of the dynamical exponent  $z$  is close to the analytical predictions in the large-coupling limit.

#### *Rubin-Shapiro sequence*

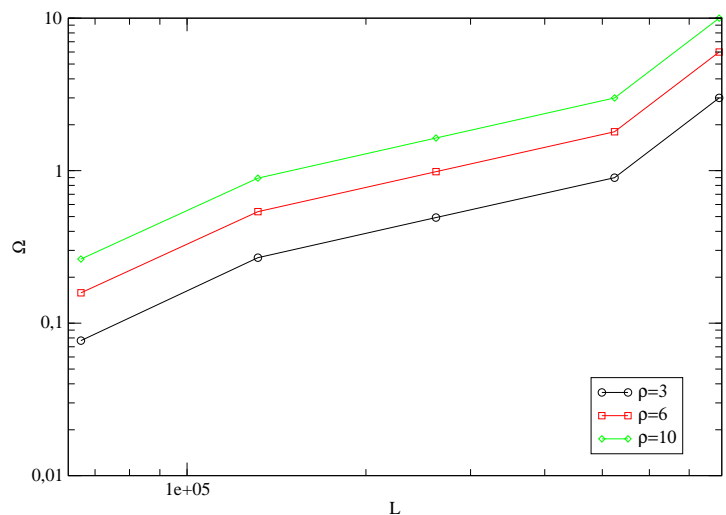


Figure 43: Energy scale versus the lattice length for three different values of the ratio  $\rho = 3, 6, 10$  for the Rudin-Shapiro sequence.

The case of the Rubin-Shapiro sequence, which is a relevant perturbation for the Ising chain, is presented on Fig. 43. In contrast to other sequences, the behavior of  $\Omega$  versus  $L$  does not seem to be algebraic. As expected for a relevant sequence, the dynamical exponent is not finite and the scaling law (83) is expected. Unfortunately, due to the stair-like behavior of  $\Omega$ , we have a too small number of points to make a non-linear fit with Eq. (83). To estimate the exponent  $\psi$ , we considered a chain with a coupling ratio  $\rho = 8$ . We set the initial energy cut-off as  $\Omega_I = 10$ . Plotting  $L$  versus  $\ln \frac{\Omega_I}{\Omega}$ , we estimated, according to Eq. (83), the exponent

$$\psi_{\text{rubin-shapiro}} = 0.5(3). \quad (208)$$

The first point of the numerical data was excluded because it is exactly at the beginning of renormalization procedure and the system is still far from the fixed-point. Unfortunately, due to the small number of points, the error bar is quite large.

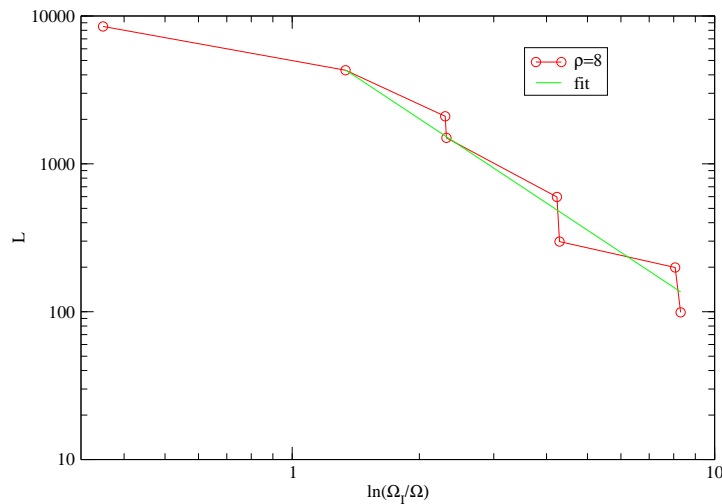


Figure 44: Scaling of lattice length with energy for the Rubin-Shapiro sequence for coupling ratio  $\rho = 8$ .

Finally, for the relevant Rubin-Shapiro sequence, the numerically estimated exponent  $\psi$ , is close to the analytical prediction  $\psi = \omega = 1/2$  of F.J. Oliveira Filho *et al.* [91].

## 5.4 THE APERIODIC QUANTUM POTTS MODEL

The study, performed in the previous section for the quantum Ising chain in a transverse field, is extended to the Potts model.

## 5.4.1 SDRG analysis for the Fibonacci family of aperiodic sequences

We first consider the one-dimensional quantum  $q$ -state Potts model defined by the Hamiltonian (91) with a modulation of the nearest-neighbor couplings following the Fibonacci family of aperiodic sequences (§ 5.3.1). The couplings take the two values  $J_a$  and  $J_b$ . The transverse magnetic field  $h$  is considered as uniform over all the lattice. In analogy with the aperiodic Ising chain, the couplings are assumed to follow the inequality  $J_a < h < J_b$ .

In the original Fibonacci sequence, the couplings  $J_b$  form clusters of  $k$  identical couplings which contain  $k + 1$  Potts spins. Each one of these Potts spins is coupled to a transverse field  $h$ . During the renormalization process, the cluster is replaced by an effective  $q$ -state macro spin whose states correspond to the  $q$  ground states of the Hamiltonian limited to the  $k$  couplings  $J_b$ . The effective transverse field acting on this macro-spin is obtained by  $k + 1$ -th order perturbation theory:

$$h^{(j+1)} = \frac{2^k [h^{(j)}]^{k+1}}{q^k [J_b^{(j)}]^k}. \quad (209)$$

After the renormalization of all couplings  $J_b$ , the transverse magnetic field  $h$  becomes the largest energy scale in the system. It is found only as clusters of  $k$  identical fields acting on  $k$   $q$ -state Potts spins. These spins interact with their neighbors with a coupling  $J_a$ . The quantum state is projected out onto the ground state of the  $k$  transverse fields. The spins are therefore frozen and can be decimated. The effective coupling between the two spins at the left and the right of the cluster is

$$J_a^{(j+1)} = \frac{2^k [J_a^{(j)}]^{k+1}}{q^k [h^{(j)}]^k}. \quad (210)$$

After renormalization of all fields  $h$ , the couplings  $J_a$  are finally the largest couplings. The replacement

$$J_b^{(j+1)} = J_a^{(j)}. \quad (211)$$

brings the system back to its initial state. It follows from the SDRG rules (210), (209) and (211) that the ratios Eq. (169) satisfy

$$\begin{pmatrix} \ln r^{(j+1)} \\ \ln s^{(j+1)} \end{pmatrix} = \begin{pmatrix} k & -1 \\ -k & k+1 \end{pmatrix} \begin{pmatrix} \ln r^{(j)} \\ \ln s^{(j)} \end{pmatrix} + \begin{pmatrix} C_k \\ 0 \end{pmatrix}, \quad (212)$$

with  $C_k = k \ln(\frac{2}{q})$ . The matrix  $\mathbb{T}_k$  resulting from the SDRG analysis of the quantum  $q$ -state Potts model is the same as the one of the quantum Ising model (171). The only difference is the presence of the constant  $C_k$ . If the fixed point of these RG equations corresponds to an Infinite-Disorder Fixed Point then we expect  $\ln r$  and  $\ln s$  to diverge. As a consequence, the constant  $C_k$  which remains finite becomes infinitely smaller than the rest of the equation. The number of states  $q$  is expected to be an irrelevant scaling field at the fixed point. The critical exponents should be identical to those of the Ising chain. In contrast, there may exist fixed points where  $\ln r$  and  $\ln s$  do not diverge, without corresponding to the pure model. This is the case for  $k = 2$  in the Ising case.  $C_k$  cannot be neglected and  $q$  may not be an irrelevant perturbation. It is then interesting to study this case.

#### 5.4.2 Magnetic scaling dimension

We now present our results obtained using a numerical implementation of SDRG for the quantum aperiodic Potts chain. In this section, we first discuss the estimation of the magnetic scaling dimension.

##### *Paper-Folding sequence*

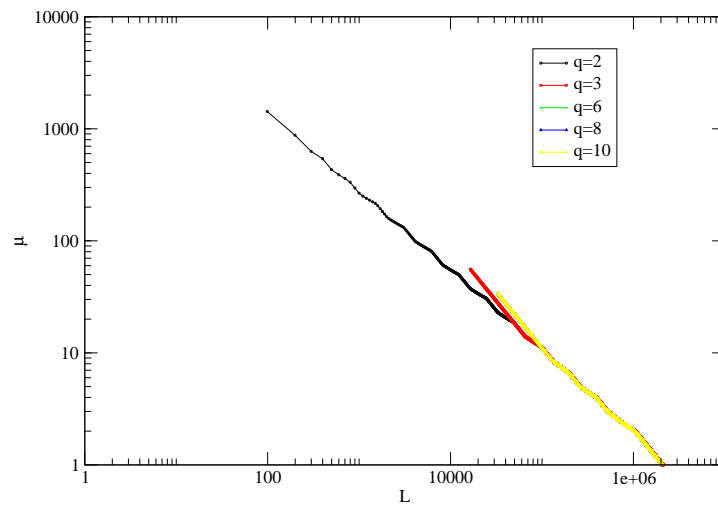


Figure 45: Renormalization of the average magnetization for the Potts model with  $q = 2, 3, 6, 8$  and  $10$  for the Paper-Folding sequence.

The renormalization of the average magnetic moment is now discussed in the case of the Paper-Folding sequence (§ 5.2.3.4). On figure 45, we present the renormalization of the Potts model for five different numbers of states  $q$ . The first curve corresponds to  $q = 2$ , i.e. the quantum Ising model with a transverse field for which the Paper-Folding sequence is a marginal perturbation. The others curves correspond to Potts models with  $q > 2$  for which the sequence is relevant.

The first three renormalization steps are the same for all the curves since the couplings  $J_b$ ,  $h$  and  $J_a$  are the same. The curves overlap exactly down to  $L \simeq 40.000$ . For all the curves, the alternating of segments of different slope, leading to an oscillatory behavior, results from the two kinds of renormalization taking place: renormalization of couplings and renormalization of fields. Indeed, while the lattice site decreases in the same way during these two kinds of renormalization, the total magnetic moment decreases only during the renormalisation of field. For the numbers of states  $q > 2$ , the curves have shorter length. For  $q = 3$  the renormalization procedure stops already at  $L \simeq 20.000$  while for  $q = 6, 8$  and  $10$ , it stops for  $L \simeq 40.000$ . In contrast, the Ising chain is renormalized until  $L \simeq 10^2$  sites are left. In all cases, the renormalization stops when in the system remains a single effective cluster. Unfortunately, we do not have any convincing explanation of why these final clusters depends so drastically on  $q$ . The only difference between the Ising and Potts cases is the presence of a factor  $2/q$  in the denominator of the SDRG rules (209) and (210).

Finally, since the average magnetization is expected to scale as  $\mu \sim L^{1-\beta/\nu}$ , the critical exponent  $\beta/\nu$  is estimated by performing a log-log fit for all the curves. All exponents are found to be compatible with the Ising value Eq. (199). The critical exponent  $\beta/\nu$  is therefore independent of the number of states  $q$ , as in the random Potts chain.

#### *Period-Doubling sequence*

The renormalization of the average magnetization of the Period-Doubling sequence 5.2.3.3 is presented on Fig. 46.

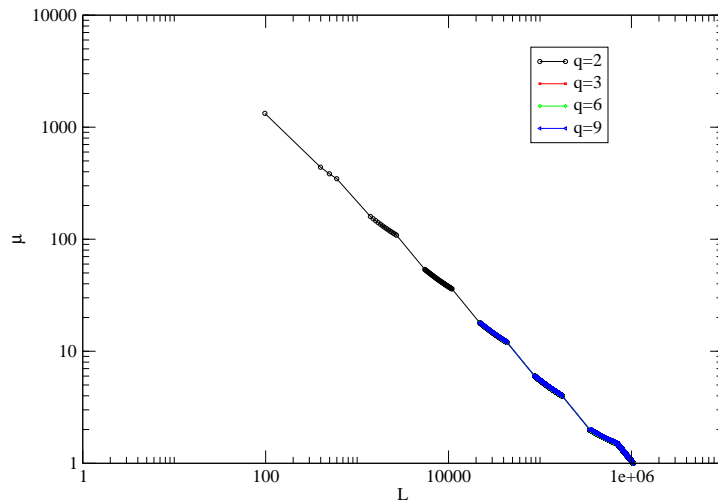


Figure 46: Renormalization of the average magnetization for the  $q = 2, 3, 6$  and  $9$ -state Potts models with the Period-Doubling sequence. The different curves correspond to different numbers of state  $q$ . The curves for  $q = 3, 6$  (red, green) are under the data of  $q = 9$  (blue).

The renormalization of the magnetic moment displays the same evolution as in the aperiodic Ising model: the data form well separated bunches of points. This phenomena is related to the characteristic construction of the substitution rules of the Period-Doubling sequence where there are relatively few couplings  $J_b$  (or letter 1 in 5.2.3.3). The SDRG renormalization procedure decimates first the coupling  $J_b$  and then the critical field  $h_c$ . But, due to the substitution rules, *most* of the weak exchange couplings  $J_a$  disappear during the renormalisation of the largest critical field (210). The next renormalized couplings are the first created effective couplings. The separated bunches of points on Fig. 46 are created by the absence of renormalization of  $J_a$ . The fact that the slope is different in the bunches of points and between two bunches confirms that only effective fields are renormalized.

q	L	$L_a = 10^6 - 277.890$	$L_b = 242.000 - 78.497$	$L_c = 73.980 - 19.310$
2	0.265(7)	0.383(1)	0.419(7)	0.419(7)
3	0.278(8)	0.383(1)	0.419(7)	0.419(7)
6	"	"	"	"
9	"	"	"	"

Table 11: Critical exponent  $\beta/\nu$  for the quantum  $q$ -state Potts chain with a Period-Doubling sequence.  $L$  denotes a fit over all data points while  $L_a$ ,  $L_b$  and  $L_c$  are limited fitting windows.

Performing a log-log fit in four different regions of the numerical data for the Period-Doubling sequence, we estimated the critical exponent  $\beta/\nu$ . The estimates are presented in table 11. The critical exponent is not stable but depends of the range of sizes in which the log-log fit is performed. For the whole lattice,  $\beta/\nu$  is found to be close for any  $q$  with the Ising exponent Eq. (200).

#### *Three-Folding sequence*

For the Three-Folding sequence, the renormalization of the average magnetization is presented on Fig. 47. The picture is very similar to the Paper-Folding sequence. A log-log fit over all data points gives an estimate of the critical exponent  $\beta/\nu$  which is compatible with the corresponding exponent for the aperiodic Ising model Eq. (201) for any value of  $q$ . The numerical estimate is stable for any value of  $q$  and, as in the previous two sequences, the renormalization stops when remains a huge single cluster in the system.

#### *Rubin-Shapiro sequence*

According to Harris-Luck criterion, the Rubin-Shapiro sequence is a relevant perturbation for any value of  $q$ . We present the renormalization of the average magnetization on Fig. 48 for several numbers of states  $q$ . For this sequence, the renormalization stops when remains a

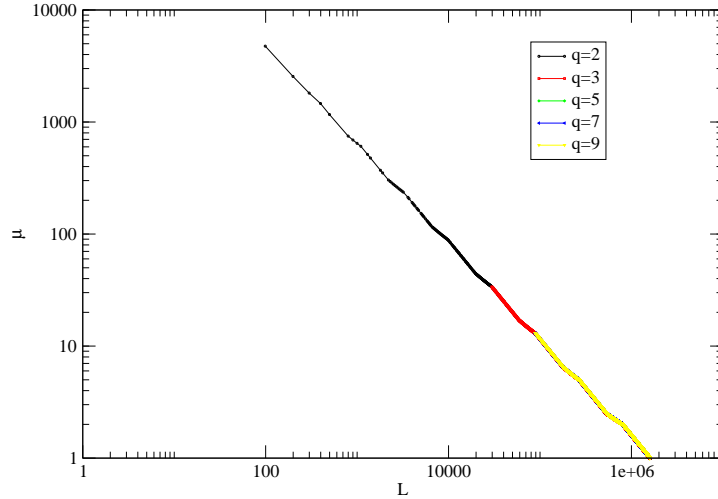


Figure 47: Renormalization of the average magnetic moment for the  $q = 2, 3, 5, 7$  and 9-state Potts model with a Three-Folding sequence. The different curves correspond to different states  $q$ . The curves of  $q = 5, 6$  (green, blue) are under the curve of  $q = 9$  (yellow).

cluster of effective couplings which is much smaller than in previous sequences.

$q$	$L$	$L_a = 10^6 - 10^4$	$L_b = 10^4 - 10^2$
2	0.228(6)	0.216(6)	0.13(3)
3	0.206(4)	0.20(7)	0.12(3)
4	0.205(5)	0.20(7)	0.17(3)
7	0.159(4)	0.156(4)	0.12(6)
12	0.159(4)	0.156(4)	0.21(2)
18	0.159(5)	0.156(4)	0.17(4)
20	0.159(6)	0.156(4)	0.17(4)

Table 12: Critical exponent  $\beta/\nu$  for the Rubin-Shapiro sequence for the quantum  $q$ -state Potts chain.  $L$  denotes a fit over all data points while  $L_a, L_b$  are limited fitting windows.

The results of the fits are given in table 12. The critical exponent  $\beta/\nu$  decreases as the number of states increases. The estimates in the window  $L_a$ , which we expect to be closer to the fixed-point, is not compatible with the exponent of the Ising model, Eq. (202). This surprising discrepancy reflects probably the high sensitivity of the estimate on the fitting window. However, for large values of  $q$ , the exponents come closer to the value given by F.J. Oliveira Filho *et al* [91] (0.1505).

Finally, for the sequences Paper-Folding, Period-Doubling and Three-Folding, the critical exponent  $\beta/\nu$  of the aperiodic quantum Potts model is clearly independent of the number of states  $q$ . In the case of

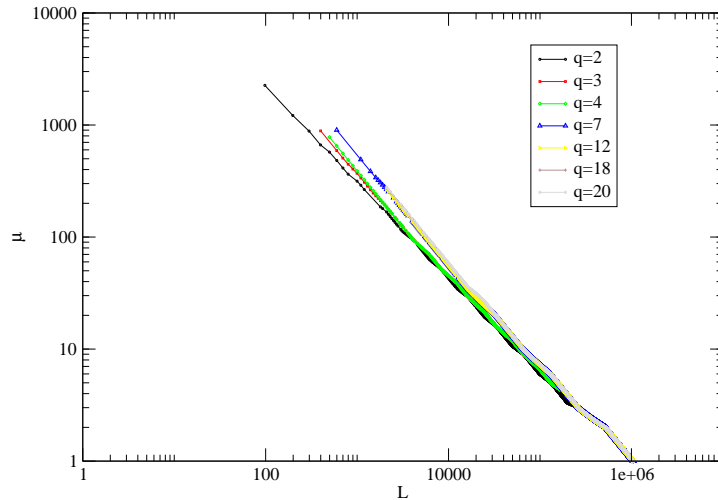


Figure 48: Renormalization of average magnetization for the Potts model of several numbers of state  $q$  with the Rubin-Shapiro sequence.

the Rubin-Shapiro sequence, the critical exponent  $\beta/\nu$  decreases as the increases. A plateau seems however to be reached for large  $q$ .

#### 5.4.3 Dynamical exponent

Here, we study the scaling of the largest energy scale  $\Omega$  with the length of the chain at the critical point and the dependence of the dynamical exponent  $z$  on the ratio  $\rho$ . For the aperiodic quantum Potts model, there is no exact expression of the dynamical exponent  $z$ .

As explained for the aperiodic Ising chain (5.3.2.2), the energy scale  $\Omega$  does not evolve monotonously during the renormalization but displays big *steps*. To estimate the dynamical exponent, we consider the corners of these steps, like in Fig. 38 where each corner corresponds to a different renormalized coupling.

##### 5.4.3.1 Paper-Folding sequence

We begin with the marginal case of the Paper-Folding sequence 5.2.3.4 for the  $q = 2$  quantum Potts model, equivalent to the Ising model. The largest energy scale is plotted with the lattice length for the ratios  $\rho = 3, 6$  and  $10$  is presented in Fig. 49. For this case, log-periodic oscillations are absent as for the Ising model. Performing a log-log fit of the data, we find the dynamical exponent  $z$  for each ratio, table 13. All the values are compatible with the corresponding values of the dynamical exponent for the Ising model in table 8.

On Fig. 50, we present the largest energy scale  $\Omega$  with the lattice size  $L$  for several numbers of Potts states  $q$ . Fig. 50a corresponds to a coupling ratio  $\rho = 10$  and 50b to  $\rho = 50$ . In both figures, the scaling

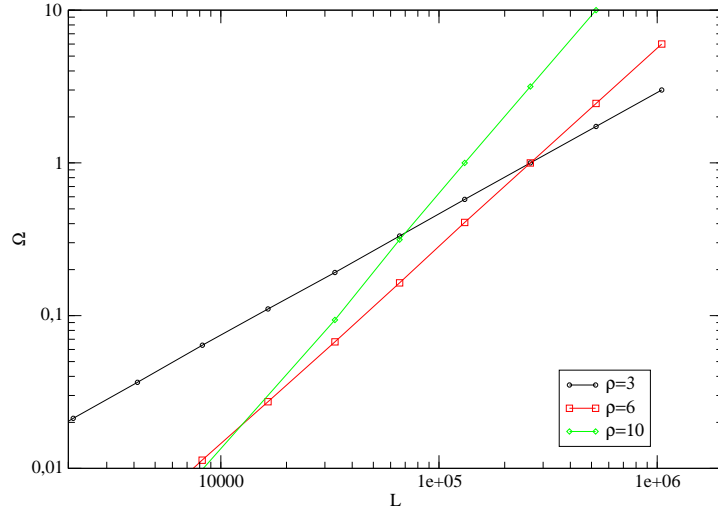


Figure 49: Largest energy scale versus the lattice length for three different values of the ratio  $\rho = 3, 6, 10$  for the  $q = 2$  quantum Potts model with the marginal Paper-Folding sequence.

Paper-Folding $q = 2$	$z$ (SDRG simul.)	$z_{Ising}$ (exact)
$\rho = 3$	0.80(7)	1.278
$\rho = 6$	1.31(5)	1.548
$\rho = 10$	1.69(1)	1.858

Table 13: Dynamical exponents  $z$  for three different ratios obtained by numerical SDRG approach for the marginal  $q = 2$  quantum Potts states for the Paper-Folding sequence.

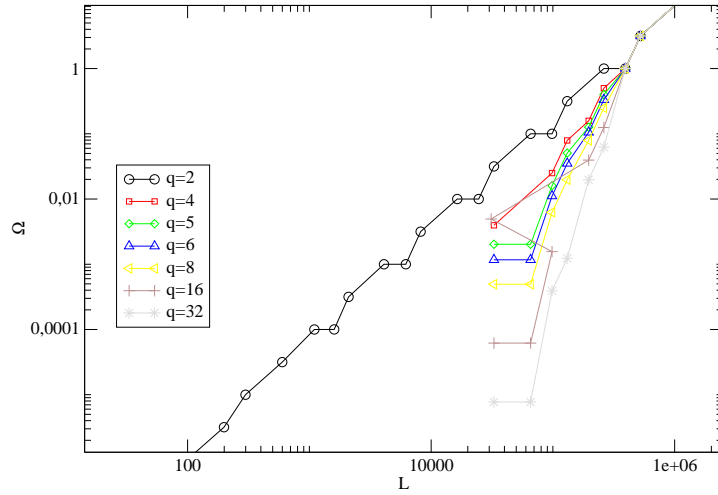
is very similar to the scaling of the average magnetization. For  $q = 2$ , the scaling is continuous until  $L = 100$  while for  $q > 2$  it stops before, i.e. for a large final cluster.

On Fig. 51, we present the scaling of the largest energy  $\Omega$  with the lattice size for five values of the coupling ratio  $\rho$  in the case  $q = 5$  on Fig. 51a and for  $q = 6$  on Fig. 51b. The scaling depends on the ratio  $\rho$ .

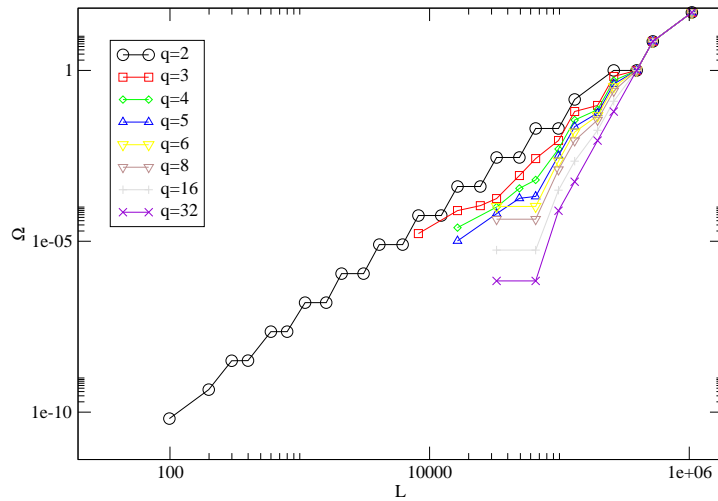
Despite the fact that quality of the curves is not optimal (due to the necessity to keep only the corners of the steps), we performed a log-log fit for several numbers of state  $q$  and several ratios  $\rho$ . Rough estimates of the dynamical exponent  $z$  are presented on Fig. 52. For the marginal case  $q = 2$ , the dynamical exponent is close to the exact analytical prediction of Igloi *et al.* [77]. For  $q > 2$ , i.e. in the relevant case, a finite exponent  $z$  is obtained which increases with the number of states  $q$ .

#### *Period-Doubling sequence*

For the Period-Doubling sequence, the scaling of  $\Omega$  with the lattice length  $L$  for various numbers of states  $q$  and for two different coupling ratios, is presented on Fig. 53. The picture is very similar to



(a)  $\rho = 10$



(b)  $\rho = 50$

Figure 50: Largest energy scale  $\Omega$  with the lattice size  $L$  for various numbers of states  $q$  for the Paper-Folding sequence with two different coupling ratios  $\rho$ . The different curves correspond to different  $q$ .

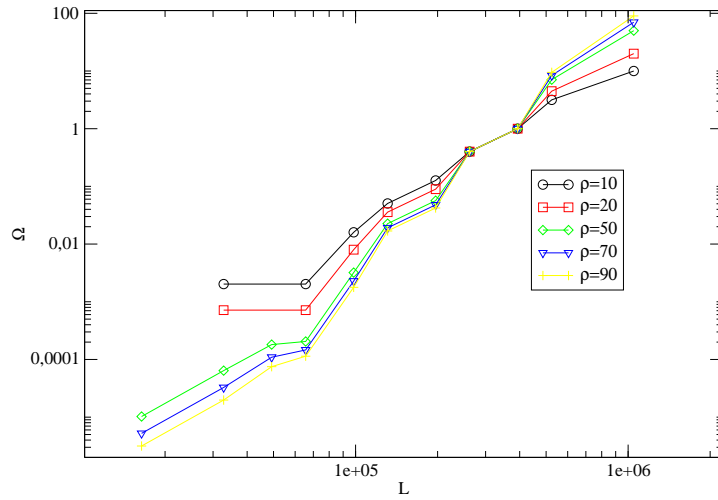
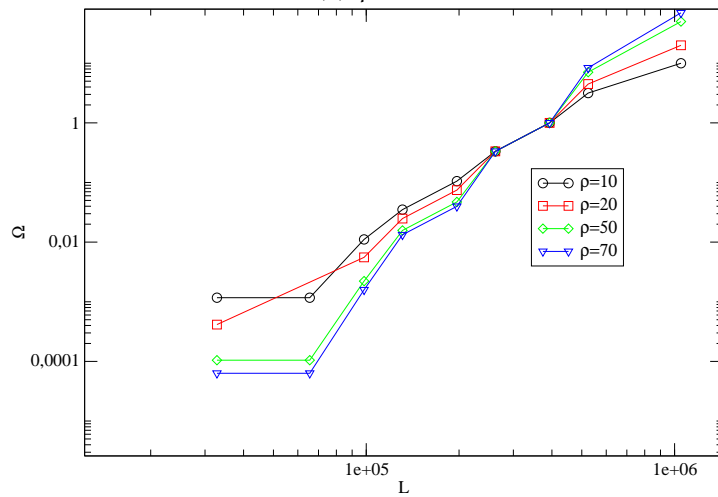
(a)  $q = 5$ (b)  $q = 6$ 

Figure 51: Energy scaling with the lattice size for five values of the coupling ratio  $\rho$  of the Paper-Folding sequences of  $q = 3$  and  $q = 5$ . The different curves correspond to different ratios  $\rho$ .

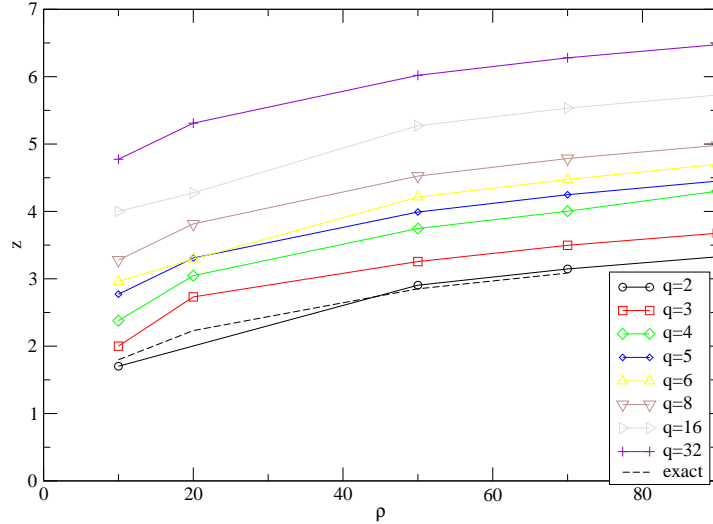


Figure 52: Dynamical exponent  $z$  with the coupling ratio  $\rho$  for several numbers of state  $q$  for Potts chains with the Paper-Folding sequence. The different curves correspond to different numbers of states  $q$ .

the previously-discussed Paper-Folding sequence. In both cases, the curves strongly depends on  $q$ . At the beginning of the renormalization, when  $\Omega$  is still large, the curves for all numbers of states  $q$  overlap but after the renormalization of all the initial couplings, a different behavior is observed. Comparing the figure 53a for  $\rho = 2$  and Fig. 53b for  $\rho = 5$ , a small dependence on the coupling ratio  $\rho$  is observed. On Fig. 53, we present the scaling of  $\Omega$  with  $L$  for four different coupling ratios. In these cases, Fig. 54a for  $q = 4$  and Fig. 54b for  $q = 6$ , the dependence of the scaling on  $q$  is smaller as  $\rho$  increases.

By a log-log fit, the dynamical exponent is estimated and presented on Fig. 55 as a function of the coupling ratio. The dynamical exponent  $z$  is clearly increasing with  $q$ . For the marginal case of  $q = 2$ , the numerical data converges for  $1/\rho > 0.05$  to the analytical prediction of the Period-Doubling sequence of [77] while for  $q > 2$  the dynamical exponent gradually increases.

#### *Rudin-Shapiro sequence*

For the Rubin-Shapiro sequence the scaling of the largest energy  $\omega$  for various numbers of state  $q$  is presented on Fig. 56, for the coupling ratio  $\rho = 20$  on Fig. 56a and for  $\rho = 90$  on Fig. 56b.  $\Omega$  is decreases with  $q$  because, as explained in the previous cases, the increase of  $q$  leads to smaller effective couplings and fields according to the SDRG rules. The first two points in both figures are the same for all the curves because they correspond to the renormalization of the same initial couplings. The scaling of the largest energy with

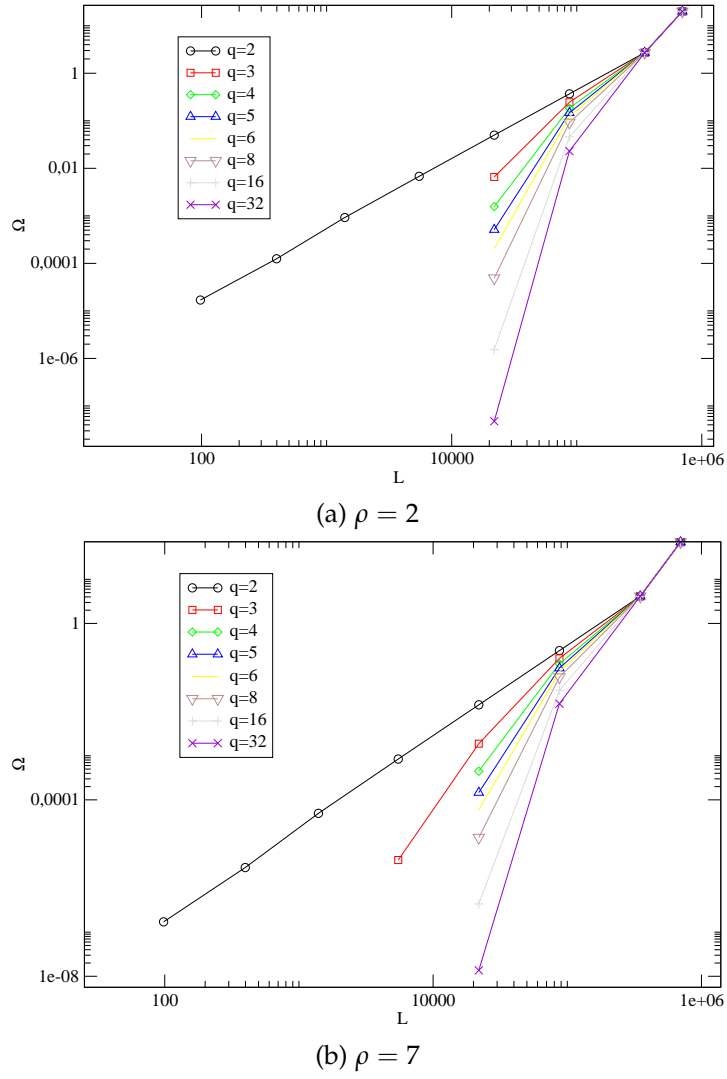


Figure 53: Energy scaling with the lattice size for various states  $q$  of the Period-Doubling sequence for two different coupling ratios  $\rho$ . The different curves correspond to different  $q$ .

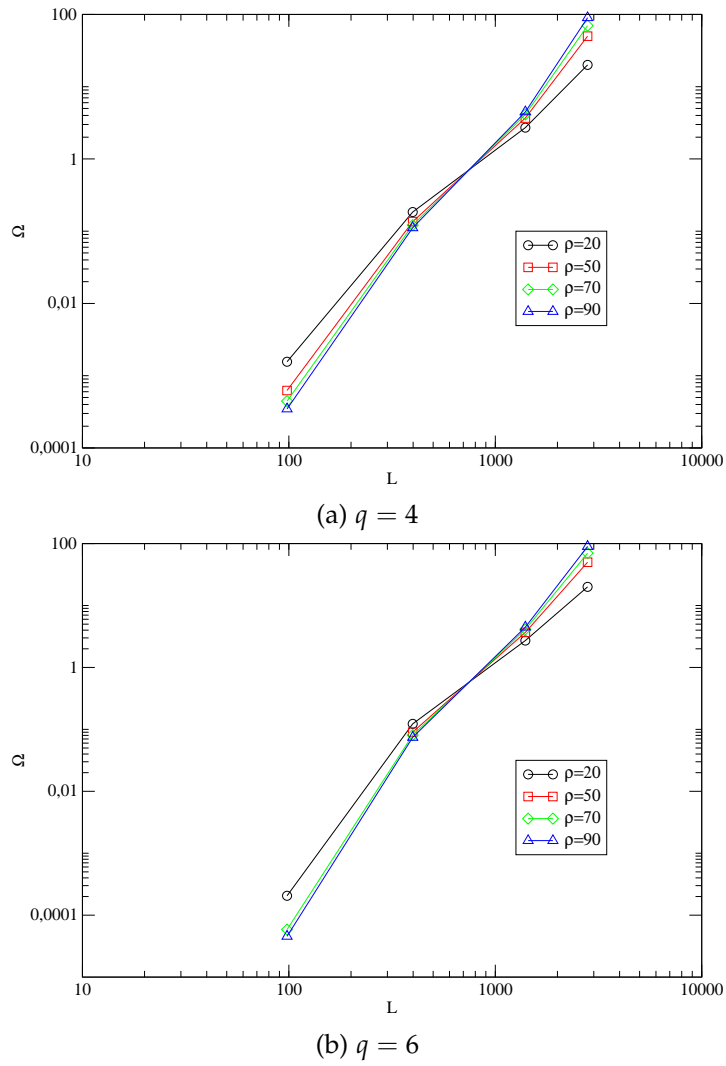


Figure 54: Energy scaling with the lattice size for five values of the coupling ratio  $\rho$  for the Period-Doubling sequences and  $q = 4$  and  $q = 6$  Potts states. The different curves correspond to different ratios  $\rho$ .

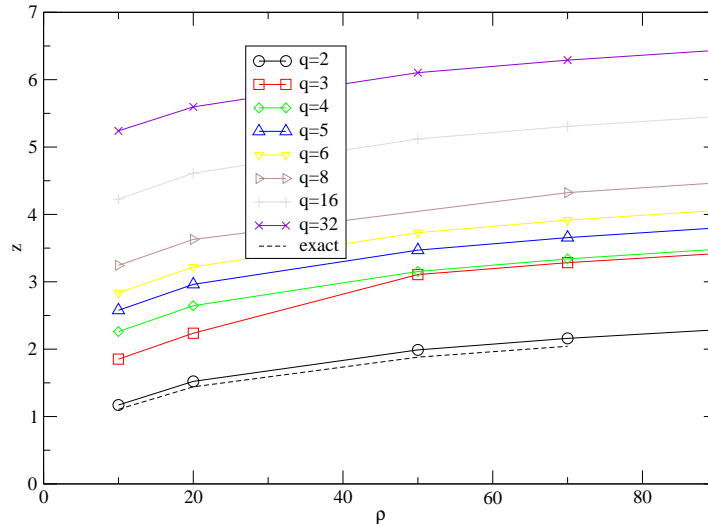


Figure 55: Dynamical exponent  $z$  with the inverse of coupling ratio  $\rho$  for several Potts  $q$ -aperiodic Period-Doubling sequences. The different curves correspond to different numbers of states  $q$ .

different coupling ratios is presented on Fig. 57, for  $q = 5$  states in Fig. 57a and for  $q = 16$  states on Fig. 57b.

Performing a log-log fit to each curve of Fig. 56, we extract the dynamical exponent  $z$  for all numbers of states  $q$ . The results are plotted versus the inverse of the coupling ratio on Fig. 58. The dynamical exponent for the Rubin-Shapiro sequence is found to increase with the number of states  $q$ , as it was the case for the other sequences.

Finally, we can conclude that the dynamical exponent  $z$  extracted numerically by SDRG approach for the sequences Paper-Folding and Period-Doubling, as well as for the Rubin-Shapiro sequence, increases with the number of states  $q$ . This result is in contrast to what we observed for the critical exponent  $\beta/\nu$ . Moreover, we observed that the dependence of the dynamical exponent  $z$  with the coupling ratio  $\rho$ , predicted by analytical study for marginal sequences for the quantum Ising chain by Igloi *et al.* [77], is also present for the Rubin-Shapiro sequence for the quantum Potts chain.

## 5.5 CONCLUSION

In this chapter, the quantum Potts chain with an aperiodic perturbation was studied by SDRG approach. We first discussed the important results of the previous studies on the critical behavior of the classical and quantum spin chains with aperiodic perturbation and then presented the Harris-Luck criterion as well as the most considered aperiodic sequences.

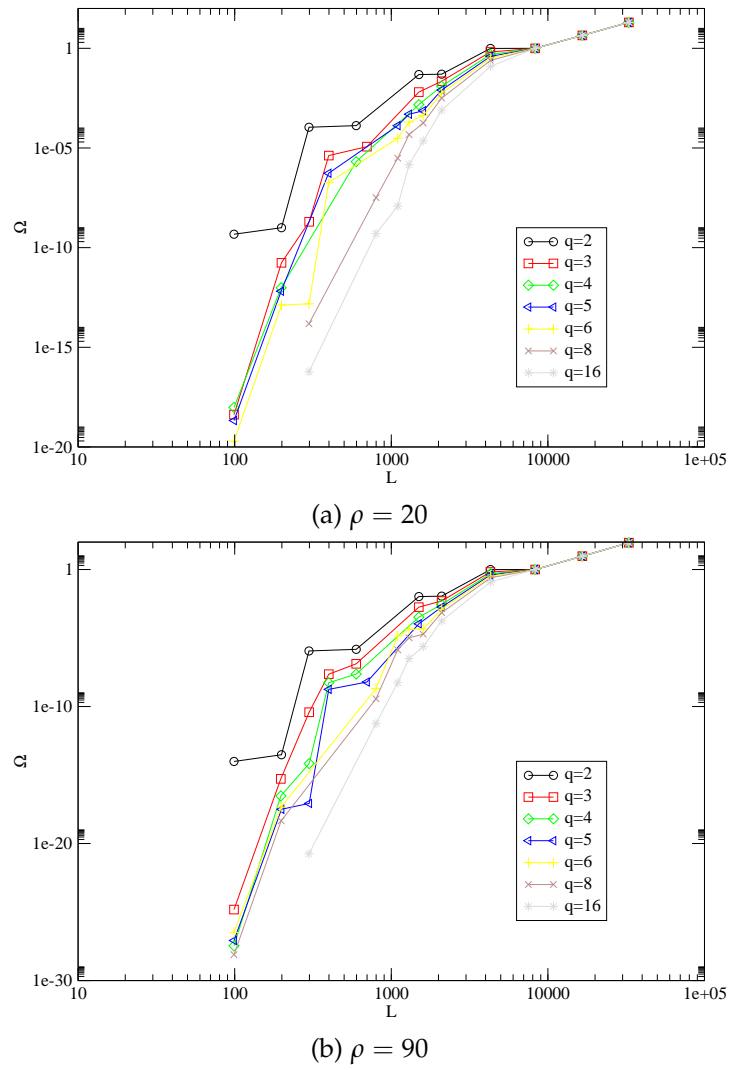


Figure 56: Largest energy scale  $\Omega$  with the lattice size  $L$  for various numbers of states  $q$  for the Rubin-Shapiro sequence with two different coupling ratios  $\rho$ . The different curves correspond to different  $q$ .

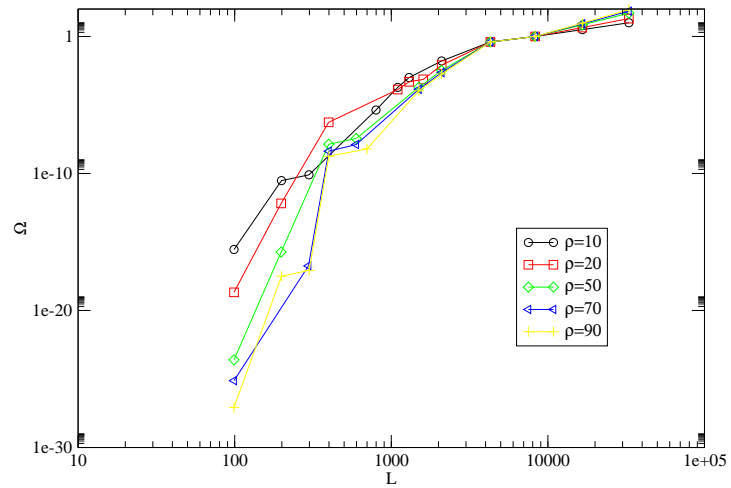
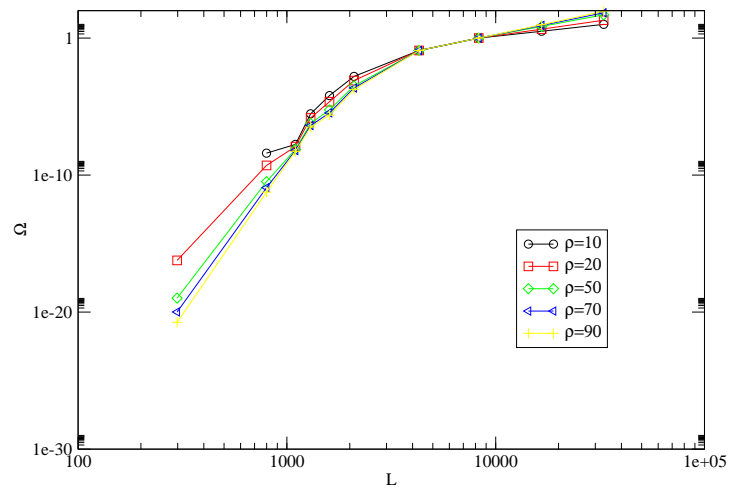
(a)  $q = 5$ (b)  $q = 16$ 

Figure 57: Largest energy scale  $\Omega$  with the lattice size  $L$  for five values of the coupling ratio  $\rho$  for the Rubin-Shapiro sequence with  $q = 5$  and  $q = 16$ . The different curves correspond to different ratios  $\rho$ .

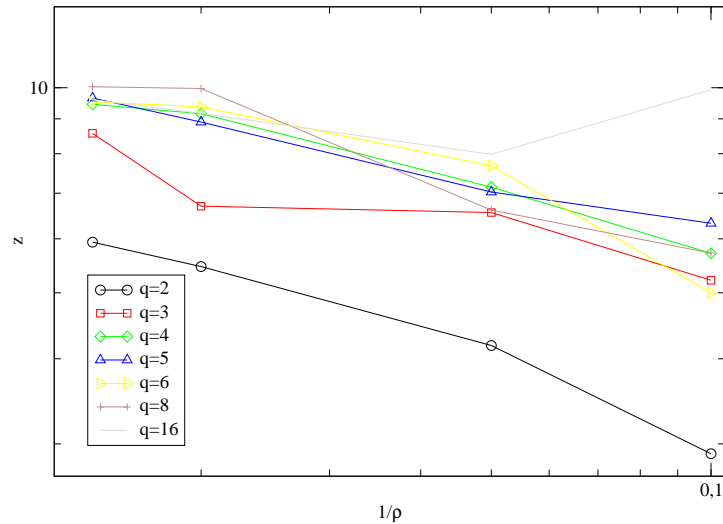


Figure 58: Dynamical exponent  $z$  versus the inverse of the coupling ratio  $\rho$  for several numbers of Potts  $q$  for the Rubin-Shapiro sequences. The different curves correspond to different numbers of states  $q$ .

The known analytical results by the SDRG approach for the quantum Ising chain for an aperiodic family of sequences are discussed. By numerical SDRG calculations, we obtain the critical exponent  $\beta/\nu$  for the quantum Ising chain in a transverse field with the marginal sequences Paper-Folding, Period-Doubling, Three-Folding and for the relevant Rubin-Shapiro sequence. The value for Period-Doubling is found to be in a good agreement with the value obtained in [91], while for the Rubin-Shapiro sequence a discrepancy is observed. The dynamical exponent is numerically estimated and is found to agree with the analytical predictions of [77] for the marginal sequences but in the limit of strong coupling ratio.

Finally, the previous study is extended to the quantum  $q$ -state Potts chain. The analytical SDRG approach leads to the same critical point as the quantum Ising chain for a Fibonacci family of sequence when  $k > 2$ . The critical exponent  $\beta/\nu$  extracted numerically by SDRG calculations is found to be independent of the number of states  $q$ , except for the Rubin-Shapiro sequence for which a dependence on  $q$  was observed. The scaling of the largest energy  $\Omega$  was found to depend on the coupling ratio and the dynamical exponent  $z$  increases with the number of states  $q$ .

---

GENERAL CONCLUSION

---

In Chapter 2, we presented the introduction and the outline of the thesis. In Chapter 3, we discussed some general information on classical and quantum phase transitions, and some basic elements of disordered systems.

In Chapter 4, we presented the critical properties of the random quantum Ising chain in a transverse field. The SDRG approach was applied to the RTFIM as well as to the random quantum  $q$ -state Potts chain, confirming by numerical calculations the critical exponents are the same for both models. The phase diagram of the random quantum Ashkin-Teller chain was extracted by the DMRG approach. On the critical lines the integrated autocorrelation time of the spin-spin and polarization-polarization autocorrelation functions present a peak. The location of the critical lines, also observed by a maximum of the disorder fluctuations of the magnetization and polarization, was determined. The coexistence of the peak of the autocorrelation time and of disorder fluctuations for the two order parameters, leads to the conclusion that the systems is controlled by disorder fluctuations rather than quantum fluctuations. Finally, the decay of the autocorrelation functions on the three different regions of the phase diagram was considered. For coupling strength  $\epsilon > 1$ , the existence of a double-Griffiths phase was confirmed. The dynamical exponents,  $z_m$  and  $z_p$ , estimated from the algebraic decay inside the Griffiths phase of the spin-spin and polarization-polarization autocorrelation functions, was extracted. As expected, the dynamical exponents,  $z_m$  and  $z_p$ , present a peak at different locations for  $\epsilon > 1$ .

From one hand, the existence of a double Griffiths phase in the random quantum Ashkin-Teller chain is well established after [41] and [102]. From the other hand, its location is not confirmed with a good accuracy in the case of a uniform coupling strength  $\epsilon$ . The same questions apply in the case of random coupling strengths  $\epsilon_J, \epsilon_h$ , with the possibility for the new couplings to be able to modify the location of the double-Griffiths phase. Moreover, another possible extension is given by the  $N = 3$  quantum random Ashkin-Teller chain, for which an analytical SDRG approach by Barghathi *et al.* [103], predicted the existence of an IDFP, while the phase diagram is still under investigation.

In Chapter 5, we discussed results concerning the critical behavior of systems with aperiodic modulation of the couplings. The analytical SDRG formulation of the aperiodic quantum Ising chain in a presence of a transverse field is discussed. By numerical SDRG calculations, we extracted the critical exponent  $\beta/\nu$  of the Paper-Folding, Period-Doubling and Three-Folding marginal sequences as well as the relevant Rubin-Shapiro sequence. The scaling of the largest energy  $\Omega$  was studied to extract the dynamical exponent  $z$ . The numerical SDRG calculations were extended to the quantum aperiodic  $q$ -state Potts chain. The critical exponent  $\beta/\nu$  was found to be independent of  $q$  for the Paper-Folding, Period-Doubling and Three-Folding sequences while for the Rubin-Shapiro, the exponent vary with  $q$ . The scaling of the largest energy depends on the coupling ratio for all the considered aperiodic sequences. The dynamical exponent is obtained for each sequence and is found to increase with the value of  $q$ .

Due to the SDRG approach, our results can only be considered accurate for large coupling ratios, i.e. large difference between the values of the two couplings  $J_a$  and  $J_b$  (or strong disorder in random chains). We are not able to see the dependence on the coupling ratio of the exponent  $\beta/\nu$ , which is observed in the aperiodic quantum Ising chain using free-fermion technique [91]. We expect to reach this behavior by DMRG calculations [104].

The self-dual Fernandez-Pacheco real-space RG approach [105], recently applied to the quantum pure and random Ising spin chains [106, 107] may be a very promising method to explore critical properties in quantum aperiodic spins chains. In particular, for aperiodic chains with *specific* substitution rules (i.e. Period-Doubling, Rubin-Shapiro, etc), the Block RG could locate the critical point [108] and give access to other quantities as generalized multifractal dimensions [109] or many-body localization phase transitions [110].

---

## BIBLIOGRAPHY

---

- [1] K.G. Wilson and J. Kogut, *Phys. Rep. C* **12**, 75 (1974).
- [2] E.H. Lieb, T.D. Schultz and D.C. Mattis, *Ann. Phys. (NY)* **16**, 406 (1961).
- [3] S. Sanchev, *Quantum Phase Transitions*, Cambridge University Press (2nd ed.) (2011).
- [4] H.E. Stanley, *Introduction to Phase Transitions and Critical Phenomena*, Oxford University Press (1971).
- [5] N. Goldenfeld, *Lectures on Phase Transitions and Renormalization Group*, Perseus Publishing (1992).
- [6] S Chattopadhyay, P Ayyub, VR Palkar, M Multani, *Phys. Rev. B* **52**, 13177 (1995).
- [7] A. Vilenkin and L. H. Ford, *Phys. Rev. D* **26**, 1231 (1982).
- [8] D. Bitko, T.F. Rosenbaum and G. Aeppli, *Phys. Rev. Lett.* **77**, 940 (1996).
- [9] L. Bemkó, S. Bordács, T. Vojta, D. Nozadze, F. Hrahsheh, C. Svoboda, B. Dóra, H. Yamada, M. Kawasaki, Y. Tokura and I. Kézsmárki, *Phys. Rev. Lett.* **108**, 185701 (2012).
- [10] M. Greiner, O. Mandel, T. Esslinger, T.W. Hänsch and I. Bloch, *Nature* **415**, 39 (2002).
- [11] H.F. Trotter, *Proc. American Math. Soc.* **10**, 545 (1959).
- [12] T. Vojta, *AIP Conf. Proc.* **1550**, 188 (2013).
- [13] A.B. Harris, *J. Phys. C* **7**, 1671 (1974).
- [14] A. Weinrib and B.I. Halperin, *Phys. Rev. B* **27**, 413 (1983).
- [15] Y. Imry and S.-k. Ma, *Phys. Rev. Lett.* **35**, 1399 (1975).
- [16] M. Aizenman and J. Wehr, *Phys. Rev. Lett.* **62**, 2503 (1989).
- [17] R.B. Griffiths, *Phys. Rev. Lett.* **23**, 17 (1969).
- [18] P. Pfeuty, *Phys. Lett. A* **72**, 245 (1979).
- [19] D.S. Fisher, *Phys. Rev. Lett.* **69**, 534 (1992); *Phys. Rev. B* **50**, 3799 (1994); *Phys. Rev. B* **51**, 6411 (1995); *Physica A* **263**, 222 (1999).
- [20] B. McCoy, *Phys. Rev. Lett.* **23**, 383 (1969).

- [21] B. McCoy and T.T. Wu, *Phys. Rev.* **176**, 631 (1968); *Phys. Rev.* **188**, 982 (1969).
- [22] B. McCoy, *Phys. Rev.* **188**, 1014 (1969).
- [23] T. Vojta, *J. Phys. A* **39**, R143 (2006).
- [24] T. Vojta, *AIP Conf. Proc.* **1550**, 188 (2013).
- [25] S.K. Ma, C. Sasgupta and C.K. Hu, *Phys. Rev. Lett.* **43**, 1434 (1979).
- [26] S.K. Ma and C. Sasgupta, *Phys. Rev. B* **22**, 1305 (1980).
- [27] F. Iglói and C. Monthus, *Physical Reports* **412**, 277-431 (2005).
- [28] F. Iglói, *Phys. Rev. B* **65**, 064416 (2002).
- [29] R. B. Potts, *Proc. Camb. Soc.* **48** 106 (1952).
- [30] F.Y. Wu, *Rev. Mod. Phys.* **54**, 235 (1982).
- [31] J. Sólyom and P. Pfeuty, *Rev. Rev. B* **24**, 218 (1981).
- [32] L. Turban, *J. Physique* **42**, 793 (1981).
- [33] J. Kogut, *Rev. Mod. Phys.* **51**, 659 (1979).
- [34] M.P.M. den-Nijs, *J. Phys. A* **12**, 1857 (1979).
- [35] J. Jose, L. Kadanoff, S. Kirkpatrick and D.R. Nelson, *Phys. Rev. B* **16**, 1217 (1977).
- [36] S. Elitzur, R. Pearson and J. Shigemitsu, *Phys. Rev. D* **19**, 3698 (1979).
- [37] T. Senthil and S.N. Majumdar, *Phys. Rev. Lett.* **76**, 3001 (1996).
- [38] J. Ashkin and E. Teller, *Phys. Rev.* **64**, 178 (1943).
- [39] M. Kohmoto, M. den Nijs and L.P. Kadanoff, *Phys. Rev. B* **24**, 5229 (1981).
- [40] E. Carlon, P. Lajkó and F. Iglói, *Phys. Rev. B* **87**, 277201 (2001).
- [41] F. Hrahsheh, J. Hoyos, R. Narayanan and T. Vojta, *Phys. Rev. B* **89**, 014401 (2014).
- [42] C. Fan, *Phys. Lett.* **39A**, 136 (1972); *Phys. Rev. B* **6**, 902 (1972).
- [43] G. Kamieniarz, P. Kozłowski and R. Dekeyeser, *Phys. Rev. E* **55**, 3724 (1997).
- [44] M. Yamanaka, Y. Hatsugai and M. Kohmoto, *Phys. Rev. B* **50**, 559 (1994).
- [45] F. Hrahsheh, J. Hoyos and T. Vojta, *Phys. Rev. B* **86**, 214204 (2012).

- [46] F. Iglói and H. Rieger, *Phys. Rev. B* **57**, 11404 (1998).
- [47] H. Rieger and A.P. Young, Quantum Spin Glasses. In Complex Behavior of Glassy Systems, Eds by Miguel Rub and Conrado Prez-Vicente, Lectures Notes in Physics 492. Springer Berlin Heidelberg. *Phys. Rev. B* **57**, 11404 (1998).
- [48] A.P. Young and H. Rieger, *Phys. Rev. B* **23**, 8486 (1996).
- [49] D. Shechtman, I. Blech, D. Gratias and J. W. Cahn , *Phys. Rev. Lett.* **53**, 1951 (1984).
- [50] M. Gardner , "Mathematical Games" *Scientific American* **236**, 111 (1977).
- [51] C. L. Henley, *Comments Cond. Matt. Phys.* **13**, 59 (1987).
- [52] T. Janssen, *Phys. Reports* **168**, 55 (1988).
- [53] P. Guyot, P. Kramer and M. de Boissieu, *Rep. Prog. Phys.* **54**, 1373 (1991).
- [54] C. Janot, J. M. Dubois and M. de Boissieu, *Am. J. Phys.* **57**, 972 (1989).
- [55] A.A. Migdal, *Sov. Phys. JETP* **42**, 743 (1976); L.P. Kadanoff, *Ann. Phys. (NY)* **100**, 359 (1976).
- [56] C. Godrèche, J.M. Luck and H. Orland, *J. Stat. Phys.* **45**, 777 (1986).
- [57] H. Ayoama and T. Odagaki, *J. Stat. Phys.* **48**, 503 (1987).
- [58] I. Bose, *Phys. Lett. A* **5**, 123 (1987).
- [59] C. A. Tracy, *J. Phys. A* **21**, L603 (1988); *J. Stat. Phys.* **51**, 481 (1988).
- [60] E. Lieb, T. Schultz and D. Mattis, *Ann. Phys. (NY)* **16**, 407 (1961).
- [61] J. M. Luck and Th. Nieuwenhuizen, *Europhys. Lett.* **2**, 257 (1986).
- [62] H. A. Ceccatto, *Z Phys. B* **75**, 253 (1989); *Phys. Rev. Lett.* **62**, 203 (1989).
- [63] F. Iglói, *J. Phys. A* **21**, L911 (1988).
- [64] J. M. Luck, *J. Stat. Phys.* **72**, 417 (1993).
- [65] J. M. Luck, *Europhys. Lett.* **24**, 359 (1993).
- [66] I. Peschel, *Phys. Rev. B* **30**, 6783 (1984).
- [67] L. Turban and B. Berche, *Z. Phys. B* **92**, 307 (1993).
- [68] L. Turban, F. Iglói and B. Berche, *Phys. Rev. B* **49**, 12695 (1994).

- [69] F. Iglói and L. Turban, *Europhys. Lett.* **27**, 91 (1994).
- [70] F. Iglói, D. Karevski and H. Rieger, *EPJ B***1**, 513 (1998).
- [71] F. Iglói, D. Karevski and H. Rieger, *EPJ B***5**, 613 (1998).
- [72] D. Karevski, G. Palágyi and L. Turban, *J. Phys. A* **28**, 45 (1995).
- [73] D. Karevski and L. Turban, *J. Phys. A* **29**, 3461 (1996).
- [74] B. Berche, P.E. Berche, M. Henkel, F. Iglói, P. Lajkó, S. Morgan and L. Turban, *J. Phys. A* **28**, L165 (1995).
- [75] P.E. Berche, B. Berche and L. Turban, *J. Phys. I (France)* **6**, 621 (1996).
- [76] F. Iglói and L. Turban, *Phys. Rev. Lett.* **77**, 1206 (1996).
- [77] F. Iglói, L. Turban, D. Karevski and F. Szalma *Phys. Rev. B* **56**, 11031 (1997).
- [78] J. Hermisson, U. Grimm and M. Baake, *J. Phys. A: Math. Gen.* **30**, 7315 (1997)
- [79] J. Hermisson and U. Grimm, *Phys. Rev. B* **57**, 673 (1998).
- [80] J. Hermisson, *J. Phys. A: Math. Gen.* **33**, 57 (2000).
- [81] Y. Okabe and K. Niizeki, *J. Phy. Soc. Jpn.* **57**, 1536 (1988).
- [82] E.S. Sørensen, M.V. Jarić and M. Ronchetti, *Phys. Rev. B***44**, 9271 (1991).
- [83] G. Langie and F. Iglói, *J. Phys. A* **25**, L487 (1992).
- [84] P.E. Berche, C. Chatelain and B. Berche, *Phys. Rev. Lett.* **80**, 297 (1998).
- [85] C. Chatelain, P.E. Berche and B. Berche, *EPJ B***7**, 439 (1999).
- [86] M.S. Faria ,N.S. Branco and M.H.R. Tragtenberg, *Phys. Rev. E* **77**, 041113 (2008).
- [87] F. Iglói and L. Turban, *Phys. Rev. E* **78**, 031128 (2008).
- [88] K. Hida, *J. Phys. Soc. Jpn.* **73**, 2296 (2004).
- [89] A. P. Vieira, *Phys. Rev. B* **71**, 134408 (2005).
- [90] A. P. Vieira *Phys. Rev. Lett.* **94**, 077201 (2005).
- [91] F. J. Oliveira Filho, M. S. Faria and A. P. Vieira, *J. Stat. Mech.*, P03007 (2012).
- [92] F. Iglói and R. Juhasz and Z. Zimboras, *Europhys. Lett.* **79**, 37001 (2007).

- [93] R. Juhasz and Z. Zimboras, *J. Stat. Mech.*, Po4004 (2007).
- [94] H. Bargathi, D. Nozandze and T. Vojta, *Phys. Rev. E* **89**, 012112 (2014).
- [95] F. Iglói, *J. Phys. A* **26**, L703 (1993).
- [96] L. Turban, F. Iglói and B. Berche, *Phys. Rev. B* **49**, 12695 (1994).
- [97] H. L. Casa Grande, N. Laflorencie, F. Alet and A. P. Vieira, *Phys. Rev. B* **89**, 134408 (2014).
- [98] P. Collet and J. P. Eckmann, *Iterated Mapps in the Internal as Dynamical Systems*, (Birkhauser, Boston 1980).
- [99] M. Dekking, M. Mendez-France and A. van der Poorten, *Math. Intelligence* **4**, 130 (1983).
- [100] M. Dekking, M. Mendez-France and A. van der Poorten, *Math. Intelligence* **4**, 190 (1983).
- [101] J. M. Dumont, *Number Theory and Physics*, Springer Proceedings in Physics, Vol. 47, edited by J. M. Luck, P. Moussa and M. Waldschmidt (Springer, Berlin 1990), p. 185.
- [102] C. Chatelain and D. Voliotis, *Eur. Phys. J. B* **89**, 88 (2016).
- [103] H. Bargathi, F. Hrahsheh, J.A. Hoyos, R. Narayanan and T. Vojta, *Physica Scripta* **T165**, 014040 (2015).
- [104] C. Chatelain and D. Voliotis, *in preparation*.
- [105] A. Fernandez-Pacheco, *Phys. Rev. D* **19**, 3173 (1979).
- [106] C. Monthus, *J. Stat. Mech.*, Po1023 (2015).
- [107] R. Miyazaki and H. Nishimori, *Phys. Rev. E* **87**, 032154 (2013).
- [108] D. Voliotis, *in preparation*.
- [109] C. Monthus, *J. Stat. Mech.*, Po4007 (2015).
- [110] C. Monthus, *J. Stat. Mech.*, 033101 (2016).

# Appendices

.1 STRONG-DISORDER RENORMALIZATION GROUP DETAILS FOR THE RTFIM

.1.1 Green functions and Dyson equation

The Schödinger equation, applied to the evolution operator, is given by [1]

$$i \frac{\partial}{\partial t} \hat{U}(t, t_i) = \hat{H} \hat{U}(t, t_i).$$

It follows that the operator

$$G^R(t, t_i) = -i\theta(t - t_i)U(t, t_i)$$

is a Green function of  $i\partial_t - H$ . In terms of the eigenvalues  $E_n$  and eigenstates  $\psi_n$  of the hamiltonien  $H$ , the retarded Green function  $G^R$  is

$$G^R(x, x_i; t - t_i) = -i\theta(t - t_i) \sum_n e^{-E_n(t-t_i)} \psi_n(x) \psi_n^*(x_i).$$

The Fourier transform is defined as

$$G^R(x_f, x_i, E) = \int_0^\infty dt e^{iEt} G^R(x_f, x_i, t).$$

If  $E$  is made complex with a small positive imaginary part then the above integral is well defined and reads

$$G^R(x_f, x_i; E) = \lim_{\epsilon \rightarrow 0^+} \sum_n \frac{\psi_n(x_f) \psi_n^*(x_i)}{E + i\epsilon - E_n}$$

and, as an operator, is written

$$\hat{G}^R(E) = \lim_{\epsilon \rightarrow 0^+} \frac{1}{E + i\epsilon - \hat{H}}.$$

We now introduce the more general Green function

$$G(z) = \frac{1}{z - H}.$$

When the hamiltonian is decomposed as

$$H = H_0 + V$$

and letting  $A = z - H$  and  $B = z - H_0$ , the following identity holds

$$\frac{1}{A} = \frac{1}{B} (B - A) \frac{1}{A} + \frac{1}{B}$$

and gives the Dyson equation [2]

$$G(z) = G_0(z) + G_0(z) \hat{V} G(z) \tag{213}$$

whose solution is formally

$$G(z) = [1 - G_0(z)\hat{V}]^{-1}G_0(z). \quad (214)$$

Equation (214) is expanded to the form [3]

$$G(z) = G_0(z) + G_0(z)\hat{V}G_0(z) + G_0(z)\hat{V}G_0(z)\hat{V}G_0(z) + \dots \quad (215)$$

The diagonal elements of  $G(z)$  in the basis  $\{|\phi_n\rangle\}$  is

$$\begin{aligned} \langle\phi_n|G(z)|\phi_n\rangle &= G_{0nn} + G_{0nn}\hat{V}_{nn}G_{0nn} + \sum_m G_{0nn}\hat{V}_{nm}G_{0mm}\hat{V}_{mn}G_{0nn} + \dots \\ &= \frac{1}{z - E_n} + \frac{\hat{V}_{nn}}{(z - E_n)^2} \sum_m \frac{\hat{V}_{nm}\hat{V}_{mn}}{(z - E_n)^2(z - E_m)} \end{aligned}$$

### .1.2 Renormalization rule for strong bond $J_i$

The Dyson equation is now applied to the calculation of an effective Hamiltonian at low energy for a quantum Ising chain in a transverse field in the presence of a strong coupling  $J_i$ . Consider the decomposition

$$H = H_0 + \hat{V},$$

where

$$H_0 = -J_i\sigma_i^z\sigma_{i+1}^z \quad (216)$$

and

$$\hat{V} = -h_i\sigma_i^x - h_{i+1}\sigma_{i+1}^x. \quad (217)$$

The ground-state of  $H_0$  corresponds to the  $z$ -basis ferromagnetic states  $|\uparrow\uparrow\rangle_z$  and  $|\downarrow\downarrow\rangle_z$  while the first excited-states are  $|\uparrow\downarrow\rangle_z = \sigma_{i+1}^x|\uparrow\uparrow\rangle_z$  and  $|\downarrow\uparrow\rangle_z = \sigma_i^x|\uparrow\uparrow\rangle_z$ . The ground-state energy is  $E_0 = -J_i$  and the energy for both excited states  $E_i = +J_i$ . The quantum mechanical perturbation theory is studied by the Dyson Eq. (215). To second order, the expansion reads

$${}_z\langle\uparrow\uparrow|G(z)|\uparrow\uparrow\rangle_z = {}_z\langle\uparrow\uparrow|[G_0(z) + G_0(z)\hat{V}G_0(z) + G_0(z)\hat{V}G_0(z)\hat{V}G_0(z)]|\uparrow\uparrow\rangle_z. \quad (218)$$

The first term of Eq. (218) is the free propagator. The second term which corresponds to the first-order perturbation theory vanishes because  $\hat{V}$  flip the spins. The perturbation theory up to second-order is written

$${}_z\langle\uparrow\uparrow|G(z)|\uparrow\uparrow\rangle_z = \frac{1}{z + J_i} + \frac{1}{(z + J_i)^2} \sum_i {}_z\langle\uparrow\uparrow|\hat{V}|\phi_i\rangle\langle\phi_i|\hat{V}|\uparrow\uparrow\rangle_z \frac{1}{z - E_i}$$

where  $|\phi_i\rangle$  denotes the two excited-states. The last term is equal to

$$\begin{aligned} z \langle \uparrow\uparrow | G(z) | \uparrow\uparrow \rangle_z &= \frac{1}{z + J_i} + \frac{1}{(z + J_i)^2} \frac{z \langle \uparrow\uparrow | \hat{V} | \downarrow\downarrow \rangle_z \langle \downarrow\downarrow | \hat{V} | \uparrow\uparrow \rangle_z + z \langle \uparrow\uparrow | \hat{V} | \uparrow\downarrow \rangle_z \langle \uparrow\downarrow | \hat{V} | \uparrow\uparrow \rangle_z}{z - E_i} \\ &= z \langle \uparrow\uparrow | G_0 \hat{V}_{\text{eff}} G_0 | \uparrow\uparrow \rangle_z \end{aligned}$$

At low energy  $z \simeq E_0$ , the denominator of the second term can be approached by  $z - E_i \simeq 2J_i$ . The Dyson equation then gives the effective coupling

$$\hat{V}_{\text{eff}} = \frac{h_i h_{i+1}}{J_i}.$$

### .1.3 Renormalization rule for a strong field $h_i$

We now consider the case of the quantum Ising chain with a strong transverse field  $h_i$ . To construct an effective Hamiltonian, we start with the decomposition

$$H_0 = -h_i \sigma_i^z$$

and

$$\hat{V} = -J_{i-1} \sigma_{i-1}^z \sigma_i^z - J_i \sigma_i^z \sigma_{i+1}^z.$$

The ground-state corresponds to the  $x$ -basis state  $|\uparrow\rangle_x$  and the first excited states are  $|\downarrow\rangle_x = \sigma_i^z |\uparrow\rangle_x$ . The ground-state energy is  $E_0 = -h_i$  and the first-excited one is  $E_i = +h_i$ . The Dyson Eq. (215) reads

$${}_x \langle \uparrow | G(z) | \uparrow \rangle_x = {}_x \langle \uparrow | [G_0(z) + G_0(z) \hat{V} G_0(z) + G_0(z) \hat{V} G_0(z) \hat{V} G_0(z)] | \uparrow \rangle_x$$

where, as in the previous case, the first-order term vanishes while the rest gives

$$\begin{aligned} {}_x \langle \uparrow | G(z) | \uparrow \rangle_x &= \frac{1}{z + h_i} + \frac{1}{(z + h_i)^2} \frac{{}_x \langle \uparrow | \hat{V} | \downarrow \rangle_x \langle \downarrow | \hat{V} | \uparrow \rangle_x}{z - E_i} \\ &= {}_x \langle \uparrow | G_0 \hat{V}_{\text{eff}} G_0 | \uparrow \rangle_x, \end{aligned}$$

At low energy,  $z - E_i \simeq 2h_i$ , we obtain the effective hamiltonian

$$V_{\text{eff}} = \frac{J_{i-1} J_i}{h_i}.$$

.2 SDRG FOR THE POTTS MODEL

.2.1 Properties for the Potts operators

In the Potts model, operators  $\hat{\Omega}_i$  and  $N_i$  are defined on each site  $i$  of the chain. The operator  $\hat{\Omega}_i$  is related to the next-neighboring interactions between Potts states and is given by

$$\hat{\Omega}_i |\sigma_i\rangle = \exp(i\frac{2\pi}{q}\sigma_i) |\sigma_i\rangle, \quad \hat{\Omega}_i^\dagger = \Omega_i^{-1}.$$

The operator  $\hat{\Omega}_i$  is diagonal in the Potts spin states  $|\sigma_i\rangle$ , for  $\sigma_i \in \{0, \dots, q-1\}$ . Denoting  $\omega = e^{i\frac{2\pi}{q}}$ , the Potts operator  $\hat{\Omega}$  can be written, for example for  $q = 4$ , as

$$\hat{\Omega}_i = \mathbb{1} \otimes \dots \otimes \mathbb{1} \otimes \begin{pmatrix} 1 & 0 & 0 & 0 \\ 0 & \omega & 0 & 0 \\ 0 & 0 & \omega^2 & 0 \\ 0 & 0 & 0 & \omega^3 \end{pmatrix} \otimes \mathbb{1} \otimes \dots \otimes \mathbb{1}.$$

On the other hand,  $N_i$  is a ladder operator

$$N_i |\sigma_i\rangle = |\sigma_{i+1}\rangle, \quad N_i^\dagger = N_i^{-1},$$

which is written in the matrix form as

$$N_i = \mathbb{1} \otimes \dots \otimes \mathbb{1} \otimes \begin{pmatrix} 0 & 0 & 0 & 1 \\ 1 & 0 & 0 & 0 \\ 0 & 1 & 0 & 0 \\ 0 & 0 & 1 & 0 \end{pmatrix} \otimes \mathbb{1} \otimes \dots \otimes \mathbb{1}.$$

The symmetric state

$$|\tilde{0}\rangle = \frac{1}{\sqrt{q}} \sum_{\sigma=0}^{q-1} |\sigma\rangle, \tag{219}$$

is an eigenstate of  $N$

$$N |\tilde{0}\rangle = \frac{1}{\sqrt{q}} \sum_{\sigma=0}^{q-1} |\sigma+1\rangle = \frac{1}{\sqrt{q}} \sum_{\sigma'=0}^{q-1} |\sigma'\rangle = |\tilde{0}\rangle$$

for the eigenvalue 1. The operator  $\hat{\Omega}$  acting on the same state gives

$$\Omega^\sigma |\tilde{0}\rangle = \frac{1}{\sqrt{q}} \sum_{\sigma'=0}^{q-1} (\omega^\sigma)^{\sigma'} |\sigma'\rangle.$$

### .2.2 SDRG rule for strong field

The Potts Hamiltonian (105) is decomposed as the sum

$$H = H_0 + \hat{V}$$

where

$$H_0 = -h_i \sum_{i=1}^{q-1} N_i^\sigma$$

and

$$\hat{V} = -J_{i-1} \sum_{\sigma=1}^{q-1} \hat{\Omega}_{i-1}^\sigma \hat{\Omega}_i^{-\sigma} - J_i \sum_{\sigma=1}^{q-1} \hat{\Omega}_i^\sigma \hat{\Omega}_{i+1}^{-\sigma}.$$

The ground-state is the symmetric state (219) with energy  $E_0 = -h_i(q-1)$ . The excited states are  $|\tilde{\sigma}\rangle = \hat{\Omega}_i^\sigma |\tilde{0}\rangle$ , for  $\sigma \neq 0$ . The energy of the first excited-state is given by

$$H_0 \hat{\Omega}_i^\sigma |\tilde{0}\rangle = -h_i \sum_{\sigma'=1}^{q-1} N_i^{\sigma'} \hat{\Omega}_i^\sigma |\tilde{0}\rangle = h_i \hat{\Omega}_i^\sigma |\tilde{0}\rangle$$

To obtain the effective coupling, we use the Dyson Eq. (215) up to the second-order

$$\langle \tilde{0} | G(z) | \tilde{0} \rangle = \frac{1}{(z + h_i(q-1))} + \frac{1}{(z + h_i(q-1))^2} \langle \tilde{0} | \hat{V} G_0(z) \hat{V} | \tilde{0} \rangle.$$

The first-order vanishes and the second term is written as

$$\frac{1}{(z + h_i(q-1))^2} \langle \tilde{0} | \left[ \sum_j \sum_{\sigma=1}^{q-1} J_j \hat{\Omega}_j^\sigma \hat{\Omega}_{j+1}^{-\sigma} \right] G_0(z) \left[ \sum_k \sum_{\sigma=1}^{q-1} J_k \hat{\Omega}_k^\sigma \hat{\Omega}_{k+1}^{-\sigma} \right] | \tilde{0} \rangle.$$

where the sums  $j$  and  $k$  extends only over  $\{i-1, i\}$ . The only non-vanishing contribution comes from the terms with  $j = i-1$  and  $k = i$  or  $j = i$  and  $k = i-1$ . We get

$$\begin{aligned} & \frac{2J_{i-1}J_i}{(z + h_i(q-1))^2} \sum_{\sigma, \sigma'=1}^{q-1} \hat{\Omega}_{i-1}^\sigma \langle \tilde{0} | \hat{\Omega}_i^{-\sigma} G(z) \hat{\Omega}_i^{\sigma'} | \tilde{0} \rangle \hat{\Omega}_{i+1}^{-\sigma'} \\ &= \frac{2J_{i-1}J_i}{(z + h_i(q-1))^2} \sum_{\sigma, \sigma'=1}^{q-1} \hat{\Omega}_{i-1}^\sigma \hat{\Omega}_{i+1}^{-\sigma} \frac{\delta_{\sigma, \sigma'}}{z - h_i} \\ &= \langle \tilde{0} | G_0(z) \hat{V}_{eff} G_0(z) | \tilde{0} \rangle. \end{aligned}$$

At low energy, i.e.  $z - E_i \simeq h_i q$ , the effective hamiltonien is

$$\hat{V}_{eff} = -J_{eff} \sum_{\sigma, \sigma'=1}^{q-1} \hat{\Omega}_{i-1}^\sigma \hat{\Omega}_{i+1}^{-\sigma}$$

with the effective exchange coupling

$$J_{\text{eff}} = \frac{2J_{i-1}J_i}{h_i q}.$$

### .2.3 SDRG rule for strong bond

The Hamiltonian is now divided as

$$H_0 = -J_i \sum_{\sigma=1}^{q-1} \hat{\Omega}_i^\sigma \hat{\Omega}_{i+1}^{-\sigma}$$

and

$$\hat{V} = -h_i \sum_{\sigma=1}^{q-1} N_i^\sigma - h_{i+1} \sum_{\sigma=1}^{q-1} N_{i+1}^\sigma.$$

The ground-state is the ferromagnetic doublet

$$|\tilde{\sigma}\rangle = |\sigma\rangle_i \otimes |\sigma\rangle_{i+1}$$

whose energy is  $E_0 = -J_i(q-1)$ . The  $q(q-1)$  excited states have the form

$$|\sigma'\rangle_i \otimes |\sigma\rangle_{i+1} = N_i^{\sigma'-\sigma} |\tilde{\sigma}\rangle \quad \text{and} \quad |\sigma\rangle_i \otimes |\sigma'\rangle_{i+1} = N_{i+1}^{\sigma'-\sigma} |\tilde{\sigma}\rangle$$

with energy  $E_i = +J_i$ . The Dyson equation (215), up to the second-order perturbation theory, is

$$\langle \tilde{\sigma}' | G(z) | \tilde{\sigma} \rangle = \frac{1}{(z + J_i(q-1))} + \frac{1}{(z + J_i(q-1))^2} \langle \tilde{\sigma}' | \hat{V} G_0(z) \hat{V} | \tilde{\sigma} \rangle.$$

where the first-order is zero and the second-term is

$$\begin{aligned} & \frac{1}{(z + J_i(q-1))^2} \langle \tilde{\sigma}' | \hat{V} G_0(z) \hat{V} | \tilde{\sigma} \rangle \\ &= \frac{h_i h_{i+1}}{(z + J_i(q-1))^2} \sum_{\sigma'', \sigma'''=1}^{q-1} \langle \tilde{\sigma}' | (N_i^{\sigma''} G_0 N_{i+1}^{\sigma'''} + N_{i+1}^{\sigma'''} G_0 N_i^{\sigma''}) | \tilde{\sigma} \rangle + \dots \\ &= \frac{h_i h_{i+1}}{(z + J_i(q-1))^2} \sum_{\sigma'', \sigma'''=1}^{q-1} \left[ \frac{\delta_{\sigma'', \sigma' - \sigma} \delta_{\sigma''', \sigma' - \sigma}}{z - J_i} + \frac{\delta_{\sigma''', \sigma' - \sigma} \delta_{\sigma'', \sigma' - \sigma}}{z - J_i} \right] + \dots \\ &= \langle \tilde{\sigma}' | G_0(z) \hat{V}_{\text{eff}} G_0(z) | \tilde{\sigma} \rangle. \end{aligned}$$

We assume as before that  $z \simeq -J_i(q-1)$  and we conclude that the effective Hamiltonian is

$$h_{\text{eff}} = \frac{2h_i h_{i+1}}{J_i q}.$$

## .3 DENSITY-MATRIX RENORMALIZATION GROUP

.3.1 *Introduction*

The Density Matrix Renormalization Group (DMRG) method has been introduced by S. White in 1992 [4] [5]. This numerical technique allows to study the ground-state properties of one-dimensional quantum many-body systems. The method was based initially on the numerical real-space renormalization group proposed by Wilson [7].

The method was extended [6]- [8] to the study of dynamical properties of eigenstates [9], classical and quantum transfer matrices problems [10], out-of equilibrium systems [11] and many others. Nowadays, DMRG is the most considered method for the study of low-dimensional quantum systems, classical systems as well as in quantum chemistry.

.3.1.1 *Wilson RG*

Wilson Numerical Renormalization Group technique [7] is the ancestor of DMRG. It was formulated to extract the ground-state of a quantum system using a subset of its Hilbert space. The system is divided into two blocks of size  $L$ . The quantum state of each one of the blocks is a vector of a  $m$ -dimensional Hilbert space. Then, the quantum Hamiltonian is decomposed in two parts, one for each block plus the interaction between them. The two-block Hamiltonian is projected out onto the sub-space spanned by the  $m$ -lowest-lying energy eigenstates giving a new truncated representation. Each operator is projected onto the new reduced basis. The size of the chain is then doubled. The procedure is iteratively repeated until the system size has reached the desired length. The method was successfully applied to the Kondo problem but failed for strongly-interacting systems. The approach is indeed based on the assumption that the  $m$  low-lying eigenstates of a small block have the same symmetry as the ground-state of the full system, which is not always true. The problem is solved with DMRG by selecting the states in a different way.

.3.2 *Density Matrix Renormalization Group algorithms*

This appendix is largely inspired from  
 Density Matrix Renormalization Group for Dummies  
 G. De Chiara, M. Rizzi, D. Rossini, S. Montangero  
 cond-mat/0603842

.3.2.1 *Infinite-system DMRG*

While the system size is doubled at each iteration of the Wilson NRG, new sites are iteratively inserted at the center of the chain in

the infinite-system DMRG algorithm. The algorithm can be summarized [6] as:

- (a) We consider a left block  $\mathbb{B}(L, m_L)$  containing  $L$  spins.  $m$  denotes the dimension of the Hilbert space. On the right of the block, we consider a single site.
- (b) We build an *enlarged* block, by adding the single site into the right part of the block. The Hamiltonian of the enlarged block  $\hat{H}_E$  is given by

$$\hat{H}_E = H_B + H_S + H_{BS},$$

where  $H_B$  is the Hamiltonian of the block,  $H_S$  is the Hamiltonian of the single site and  $H_{BS}$  is the Hamiltonian of the interaction term between these two.

- (c) The enlarged block is coupled to a similarly constructed one on the right  $\hat{H}_{E'}$ . Depending on the symmetry of the system, the right enlarged block can be obtained by the reflection of the original one.
- (d) A *super-block* Hamiltonian is constructed  $\hat{H}_{sup}$  by the interaction of the two enlarged blocks

$$\hat{H}_{sup} = \hat{H}_E + \hat{H}_{E'} + H_{SS'},$$

where  $H_{SS'}$  is the Hamiltonian of the interaction between the two single sites.

- (e)  $\hat{H}_{sup}$  is diagonalized to compute the ground-state  $|\psi_G\rangle$

$$|\psi_G\rangle = \psi_{\alpha\beta\gamma\delta} |\alpha\beta\gamma\delta\rangle.$$

From  $|\psi_G\rangle$  we construct the reduced density matrix  $\hat{\rho}_L$  of the left enlarged block, by tracing over the right block:

$$\hat{\rho}_L = \text{Tr}_R |\psi_G\rangle \langle \psi_G| = \psi_{\alpha\beta\gamma\delta} \psi_{\alpha'\beta'\gamma\delta}^* |\alpha\beta\rangle \langle \alpha'\beta'|.$$

The renormalization procedure of DMRG consists on the truncation of the Hilbert space of the enlarged block by diagonalizing the reduced density matrix and keeping the  $m_{L+1}$  largest eigenstates. The truncated change of basis is performed by using the  $m_L D \times m_{L+1}$  rectangular matrix  $\hat{O}_{L \rightarrow L+1}$  with columns the largest eigenstates. With the subscripts, we denote the input block and the corresponding block after the renormalization.

The truncated enlarged block which ..... from the renormalization is picked as  $\mathbb{B}'(L+1, m_{L+1})$  which is starting block of the new DMRG iteration, while the block Hamiltonian is given by

$$\hat{H}'_B = \hat{O}^\dagger_{L \rightarrow L+1} \hat{H}_E \hat{O}_{L \rightarrow L+1}.$$

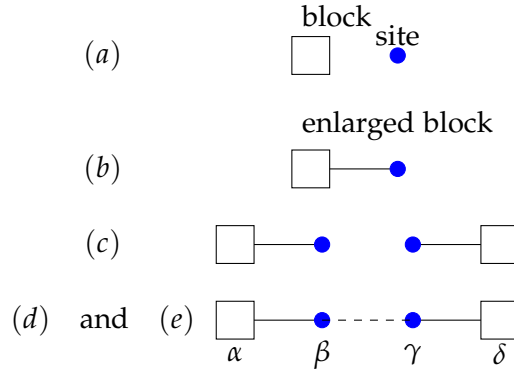


Figure 59: Infinite-system DMRG steps algorithm. The letters  $\alpha, \delta$  corresponds to blocks and  $\beta, \gamma$  to single sites.

### .3.2.2 Finite-system DMRG

In many systems which include for example strong impurity effects or randomness, the infinite- system algorithm cannot reach the appropriate accuracy for the ground-state. Therefore, the *finite system* algorithm [?] was introduced to improve the convergence and reduce the error.

The idea is to stop the infinite-algorithm at some (preselected) super-block length  $L_{max}$  which is kept fixed. The DMRG infinite algorithm continues but only one block is increased while the other decreases. The reduced basis transformations which we described above, still applies to the growing block.

The DMRG *finite-system* algorithm provides a better convergence by the *sweep procedure*, where the steps are summarized on the figure 60 and in the following:

- When the infinite-system algorithm reaches the desired size  $L_{max}$ , the system is formed by two blocks  $\mathbb{B}(L_{max}/2 - 1, m)$  and two free sites (represented into the Fig. 60 by dots).
- The left block is enlarged with one site and the right is reduced by one correspondingly. Now the system configuration is  $\mathbb{B}(L_{max}/2, m) \bullet \bullet \mathbb{B}(L_{max}/2 - 2, m)$ .
- The left block is increasing until the length  $L_{max} - 4$  is reached. The right block  $\mathbb{B}(1, D)$  is obtained by scratch while the left  $\mathbb{B}(L_{max} - 3, m)$  form renormalization procedure.
- The role of the left and right blocks are switched and the free sites starts to *sweep* from left to right.

- Each step the renormalized block has to be stored in the memory.

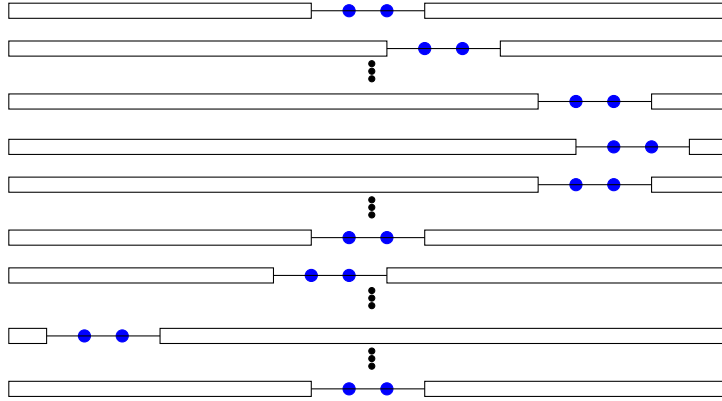


Figure 60: DMRG finite-size algorithm.

---

## BIBLIOGRAPHY

---

- [1] J.W. Negele and H. Orland, *Quantum Many-Particle Systems*, Westview Press, Boulder (1998).
- [2] F.J. Dyson, *Phys. Rev.* **75**, 489 (1949).
- [3] C. Chatelain, *Interaction Rayonnement-Matière*, Lectures notes, Nancy-Université (2008-2011).
- [4] S.R. White, *Phys. Rev. Lett.* **69**, 2863 (1992).
- [5] S.R. White, *Phys. Rev. B.* **48**, 10345 (1993).
- [6] U. Schollwoeck, *Rev. Mod. Phys.* **77**, 259 (2005).
- [7] K. G. Wilson, *Rev. Mod. Phys.* **47**, 773 (1975).
- [8] K. Halberg, *Adv. Phys.* **55**, 477 (2006).
- [9] K. Halberg, *Phys. Rev. B* **52**, 9827 (1995); T.D. Kühner and S.R. White, *Phys. Rev. B* **60**, 335 (1996); E. Jeckelmann, *Phys. Rev. B* **66**, 045114 (2002).
- [10] T. Nishino, *J. Phys. Soc. Jpn.* **64**, 3598 (1995); X. Q. Wang and T. Xiang, *Phys. Rev. B* **56**, 5061 (1997); N. Shibata, *J. Phys. Soc. Jpn.* **66**, 2221 (1997).
- [11] Y. Hieida, *J. Phys. Soc. Jpn.* **67**, 369 (1999); E. Carlon, M. Henkel and U. Schollwoeck, *Eur. J. Phys. B* **12**, 99 (1999); *Phys. Rev. E* **63**, 036101 (2001);